A virtual synchronous generator control in the power system with high penetration of renewable energies–weak grid

by

Daniel Angelo Kisinga

A thesis submitted to the

Department of Automatic Control and Systems Engineering

in partial fulfillment of the requirements for the degree of

Doctor of Philosophy

February 5, 2025

Declaration

I, Daniel Angelo Kisinga, declare that the work presented in this thesis is my own. All material in this thesis which is not of my own work, has been properly accredited and referenced.

Daniel Angelo Kisinga

Abstract

In response to global climatic change and the accessibility of clean energy in the world, power systems are experiencing a paradigm shift from conventional synchronous generators (SG) based systems to mixed generation systems with a large portion of renewable energies (RE). This has resulted in the erosion of the conventional power system's frequency control. This is because, inertia of the system declines with the continual displacement of the SG by the inertia-less RE generations such as solar photovoltaic (SPV) systems and wind turbine generation (WTG) systems. Therefore, on the occurrence of a small frequency contingency in the system, a high rate of change of frequency (RoCoF) and high frequency deviations can be experienced. This results in a cascading failure and eventually a black out.

To increase the inertia of in power systems with high penetration of RES units, an interfacing power electronic converter (inverter) can be controlled to mimic the operation of a synchronous generator (SG). This technology is known as a *virtual synchronous generator* (VSG). In this research work, VSG technology is explored in a scenario of its connection to a weak grid. That is, a grid with high penetration of RE-generation units. In this case, there is a strong coupling between active power(P) and active power (Q). Therefore, *a new virtual power circles based PQ decoupling scheme is presented in chapter 3*. The PQ decoupling is achieved by virtual addition of an RCL circuit in the VSG controller.

VSGs are required to ride through faults in order to avoid cascading failure of the system. To achieve this for a VSG connected to a weak gird, *a new low voltage ride through (LVRT) strategy using an finite control set model predictive control (FCS-MPC) is presented in chapter 4*. The strategy improves transient response of the VSG on the occurrence of faults such as voltage sags and maximises power transfer during LVRT.

The intermittent and stochastic nature of the RES makes the system inertia to be a time varying quantity rather than a constant quantity as in conventional strong power systems. Therefore in weak grids, it is important to understand and track the system's inertia values. This provides system situational analysis such that a maximum size of the frequency contingency can be defined. Moreover, optimisation of the available resources for containing frequency deviations and prevent high RoCoF can be established with the knowledge of the available inertia. Furthermore, inertia adaptive protection schemes can be designed. Thus, *a new neural network based stochastic inertia estimation method in a weak power system is presented in chapter 5*. This forms basis for designing an inertia adaptive VSG.

Contents

List of Figures

List of Tables

List of Abbreviations

ANN Artificial neural networks

ASFCL Active super conducting fault current limiter

DG Distributed generations

DU Dispatchable units

EPS Electrical power system

FRT Fault ride through

FCS Finite control set

GB Great Britain

LVRT Low voltage ride through

MPC model predictive control

PSO Power systems operators

P Active power

Q Reactive power

RES Renewable energy sources

RoCoF Rate of change of frequency

SR Spinning reserve

SFC Secondary frequency control

SPV Solar photovoltaic systems

SCL Short circuit levels

SG Synchronous generator

SFCL Super conducting fault current limiter

THD Total harmonic distortion

UFLS Underfrequency load shedding

UK United Kingdom

VSG Virtual synchronous generators

VSI Voltage source inverter

WTG Wind turbine generation

Acknowledgment

First and foremost, I am very grateful to the God–the Almighty for the gift of life, for the unnumbered blessings, grace and opportunities. It is indeed, he who strengthens me and I can do all things through him.

I have had significant help from my supervisor Dr Paul Trodden. I have benefited greatly from his guidance, patience and experience on research. I therefore, would like to express my sincere gratitude to him. I am very thankful for your presence in this challenging, yet exciting PhD journey.

I have been fortunate to receive a PhD commonwealth scholarship from United Kingdom (UK) government through Commonwealth Scholarship Commission (CSC). Funding of my studies, this research would have been impossible without them. I am very grateful to them. Moreover, I express my heartfelt gratitude to the Tanzanian government through Dar Es Salaam Institute of Technology (DIT) for granting to me a study leave.

It will be improper and ungrateful to not recognise University of Sheffield through the Department of Automatic Control and Systems Engineering (ACSE)–for providing to me with the opportunity to undertake PhD studies. I, believe, to have greatly acquired knowledge and researching skills through their properly structured PhD program.

Last but not least in significance, I appreciate all the support, prayers and love my family has shown to me during this journey. Special thanks, to my son–Ethan A. Kisinga, whenever I looked at you, I got courage to propel in these studies. I love you son!

"*The Lord is my rock, my fortress and my deliverer; my God is my rock, in whom I take my refuge, my shield and horn of my salvation, my stronghold*" Psalm 18:2.

Chapter 1

Introduction

This chapter introduces this research by providing a background on the low inertia power systems; research challenges for the low inertia EPS, research questions and their corresponding objectives, as well as by summarizing the main contributions of this research work. The chapter is finalized by providing the list of publications and by articulating this thesis organisations.

1.1 Background

Reliable electrical energy is pivotal for economic and social welfare of humankind. Smooth operation of industries and prosperous functioning of the modern societies depends heavily on the availability of the electrical energy. To suffice the need, man designed one of the most complex systems known as Electrical Power Systems. Therefore, the availability of the electrical energy depends on the reliable and secure operation of these systems. Hence, power systems must be properly operated and protected. In ensuring their protection, Power System Operators (PSO) have introduced grid codes. These provide technical specifications, operating procedures, and governing principles between the PSO and the consumers of the electrical energy [1].

The grid codes, for example frequency grid code according to Great Britain (GB) Security and Quality of Supply Standards (SQSS), are significantly important in this era where power systems are witnessing increasing penetration of Renewable Energy Sources (RES) which affects power system dynamics, due to their intermittent nature. Generally, a power system is an inherently dynamic system as a result of the nature of its operation. The state of the art of operation of a power system requires real time

balance between supply and demand, that is, power generation and power consumption, respectively. Since the loads of a power system, which quantify the power demand, are stochastic in nature then, the generation must be capable of always coping up with this stochasticity so as to maintain a constant frequency.

Frequency is, therefore, used as an indicative parameter for expressing the balance between supply and demand in power systems [2, 3]. If the supply exceeds the demand, the power system frequency increases and it decreases on the contrary event. Thus, due to the variability of the load and momentary mismatches between supply and demand, power system frequency always fluctuates. Nevertheless, these fluctuations must be within the acceptable limits as specified by the grid codes. For example, in Great Britain (GB) frequency is to be maintained by operators within 0.4% of the nominal frequency while the statutory limit is 1% of the nominal frequency [4].

Operation outside these limits is unsafe for both PSO and consumers. In terms of the power systems operation, large frequency deviations from specified limits can cause large voltage variations, power flow changes, undesired operation of relays as well as damage to the generators. Consequently, a cascading failure may arise that can even result in a blackout [5, 6]. For example, the blackout in the United Kingdom (UK) in September, 2019 [7] is a result of a large frequency excursion. Therefore, power systems are protected against reaching unsafe values by a scheme known as Under Frequency Load Shedding (UFLS) scheme. This is a must for maintaining frequency stability of a power system [8, 9].

By definition, frequency stability refers to the ability of an Electrical Power System to maintain a steady frequency following a severe mismatch between power generation and demand [5, 9]. Such mismatches can occur due to events like a sudden loss of mains or large feeders, a significant increase in load, or a sudden drop in load [10]. These events result in a rapid increase in the rate of change of frequency (RoCoF). In some countries, such as Great Britain (GB), power system protection engineers utilize RoCoF relays to detect and protect against loss of mains [4, 11]. In principle, RoCoF relays play a critical role in detecting islanding mode, which occurs when a part of the power system becomes electrically isolated but continues to operate.

Modern power systems are increasingly prone to blackouts caused by frequency instability, as demonstrated by events such as the 2016 blackout in Australia [12]. This is

contrary to the conventional power systems. The stability against frequency deviations in the conventional power systems are largely contributed by the deployment of the synchronous generators (SG) [13]. These generators have been used for power generation, provision of spinning reserve, as well as voltage and frequency regulations [14]. The frequency of the power system is directly related to the rate/speed of rotation of the rotor of the SG. The rotor is one of the three main parts of the SG, others include air-gap and the stator. The latter, is a mobile part which is made up of a rotating mass carrying windings with DC current. While in motion, the rotor stores kinetic energy. Therefore on an event, for example, a sudden increase in the load, the rotor releases the stored energy as per Newton's Second Law of motion so as to maintain its state. Thus, it maintains the frequency of a power system and resists *rapid RoCoF* in response to momentary imbalance between supply and demand. The release or absorption of energy by the rotor of SG is technically termed as *inertia response* [13]. In [7], inertia is defined as the available kinetic energy from all rotating masses which are directly coupled to the system. This definition, therefore, includes inertia from the *demand side* such as that from the directly connected motors.

Inertia response and frequency stability of a power systems are, therefore, related phenomenon. Generally, a power system with high inertia is robust against frequency oscillations, as well as stable towards large frequency contingencies. The stability is achieved by the short term supply of the stored energy by the rotating masses upon the occurrence of the frequency contingency [15]. This provides significant time for the primary and secondary frequency control actions. Hence, inertia response is key for the stable operation of a power system when subjected to a frequency contingency.

In modern power systems, however, SGs are gradually and continuously being replaced by the RES–generators. This trend is enhanced by several factors such as: environmental awareness, geopolitical oil economy, depletion of fossil fuels, falling costs of RES generators, advancement of power electronics technologies and customer preferences. Moreover, the trend is to integrate RES to the distribution system. This, thus, offers a perfect mode of electrification through elimination of the transmission costs and minimization of the losses in the system. Consequently, electrification becomes affordable and hence, fostering more penetration of RES in power systems across the globe. Many countries including the GB have set a goal of achieving 100% RE systems

by 2050 [16–19]. According to the International Renewable Energy Agency (IRENA), the status of the RES penetration in EPS across the globe is expected to increase from 25% (in 2021) to 90% (in 2050) [20]. It can be observed that out of the 90% expected RES penetration, inertia-less sources (Wind Turbine Generation (WTG) and Solar Photovoltaic Systems (SPV)) will contribute to about 63% of the increase.

Increasing penetration of the inertial-less RES generations into the electrical power system marks the decline of the systems' inertia [21–23]. For example, the system's inertia in GB has declined from 900,000 MVAs in 2008 to 300,000 MVAs in 2020 [24]. It is expected to further decline to 180,000 MVAs by 2025 [25] (Inertia constants have been converted from s–units as specified in the cited article to MVA/s under the system base of 100,000 MVA). The decline in inertia in the modern power systems is further amplified by the massive deployment of the power electronic converters (PECs) in the demand side. The systems with low inertia are faced with operational challenges as a result of the high RoCoFs and large frequency deviations (as exemplified in figure 1.1). These challenges, are also enhanced by the intermittent nature of the RES generations. This results in a time variability of the committed number of the SGs in the system [14, 15, 26]. For example, in 2012 German with only 20% contribution of RES production to the total demand, recorded several occasions in hours where 50% of the demand was from the RES [27]. A similar case is recorded in September, 2020 in the Croatian power system. The system recorded a coverage of 50% of the hourly demand by the wind farms. The actual production capacity from the RES, however, is only 12% of the total demand [28]. Therefore, penetration of RES in power systems not only reduces the inertia but also results in *a stochastic (i.e. uncertain) and time–varying inertia*.

1.2 Significances of inertia in power systems and the future prospects in modern power systems

Inertia is fundamental to maintaining frequency stability in power networks, as it governs the system's ability to resist rapid frequency changes following disturbances. *In conventional power systems, the inertia response occurs naturally and instantaneously without any active control–that is when no controller is acting in the system.* High levels of inertia in these systems traditionally ensured robust resistance to frequency contingencies.

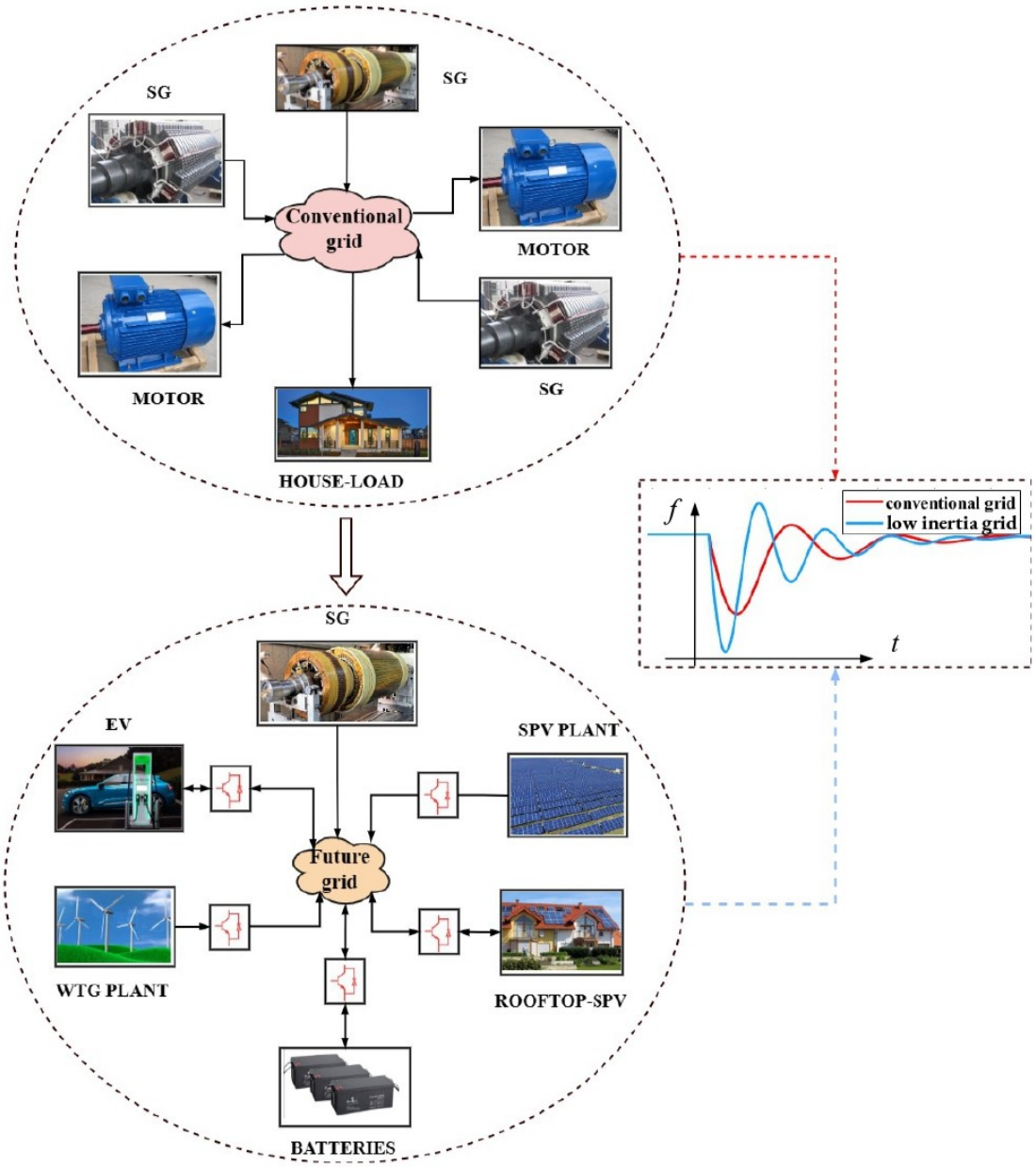

Figure 1.1: *Transition from conventional to future grid with their frequency response*

However, in future converter-dominated power systems, inertia is significantly reduced, leaving the grid more vulnerable to frequency instability. To mitigate this challenge, alternative solutions are being developed, including advanced control systems. These systems comprise primary controllers (for immediate stabilization), secondary controllers (for restoring nominal frequency), and tertiary controllers (for long-term optimization and system reliability).

Primary controllers act to limit the rapid Rate of Change of Frequency (RoCoF) immediately following a disturbance. *These controllers provide synthetic or "virtual" inertia by leveraging advanced power electronics and inverter-based resources*. Tech-

nologies such as energy storage systems, grid-forming inverters, and fast frequency response (FFR) mechanisms emulate the effects of physical inertia by rapidly injecting or absorbing power to stabilize frequency [29]. This approach enables the power system to maintain stability without relying on the inherent inertia of synchronous machines.

Secondary controllers restore the system frequency to its nominal value (e.g., 50 Hz in the GB grid). In converter-based systems, this is achieved by dynamically adjusting the power outputs of renewable energy sources (RES) and other resources like battery storage or demand response systems. On the other hand, tertiary controllers focus on the long-term optimization of power generation and consumption. Operating on a slower timescale, they ensure economic dispatch and resource allocation while maintaining grid stability and efficiency. These three levels of control collectively address the challenges posed by reduced inertia in converter-dominated power systems.

Therefore, inertia remains critical in operation of the power systems and hence–future power systems require innovative approaches, such as synthetic inertia and faster frequency control systems, to ensure frequency stability in a low-inertia environment. The transition towards these solutions is essential to accommodate the increasing share of renewable energy and to maintain reliable and resilient power systems.

1.3 Research challenges for low inertia EPS

PSO and researchers in the respective field have proposed a number of ways to address the challenges caused by the low stochastic inertia in the system. Some of the implemented practical methods include, limitation of the RES penetration and its corresponding instantaneous power generation from the RES generators and review of the RoCoF relay setting. These methods are particularly imposed by the PSO and they only provide short term solutions. Hence, new solutions are required as more RES are penetrating to the power systems so as to achieve a 2050 goal for 100% renewables. Moreover, their implementation is very challenging. The limitations and challenges of these methods are in detail discussed in Chapter 2 of this body work. On the other hand, it is proposed to continuously estimate inertia of the system for planning and optimisation of the system reserves. In literature, there are a number of methods proposed for the task. Most of the proposed methods are large disturbance based methods which depend on the occurrence

of the disturbances (transient based methods) [30–34] and they are offline. It is, however, required to be able to estimate inertia online. Moreover, the estimate must be done continuously so as to optimise resource and formulate an inertia adaptive protection scheme. Furthermore, disturbance based methods are intrusive to the system. Other methods involve system identification [14, 24, 35–37]–these involve setting of an active power perturbation in steady state conditions which excite the system's dynamics at suitable frequencies. Then, from the excited frequency response, the system model relating active power, frequency and inertia, is obtained–from which inertia is implicitly estimated. These methods are online, however, they are mathematically burdensome, intrusive to the system and perform estimation only during steady state conditions. *There exists a need, therefore, for an online, non intrusive method that can estimate a stochastic inertia during both transient and steady state conditions.* This is necessary for security-constrained optimisation of the system's resources. The in detail critical literature review of the inertia estimation methods in power systems, necessity for inertia estimation in power system with high penetration of renewables and a corresponding new estimation method is discussed in chapter 5.

Most RES are connected to the grid through PECs, in particular inverters–they can be operated to mimic SGs. Hence, they can add what is known as virtual inertia to the system. This technology is known as virtual synchronous generator (VSG) operation. There are many topologies of the VSGs ranging from virtual synchronous machine (VISMA) [38], synchronverter [39–41], simplified swing equation based VSG [42], reactive-power frequency based VSG [43, 44], droop based VSG [45, 46] etc. Studies have indicated that, among these designs, the synchronverter may be the most effective in limiting RoCoF and frequency nadir in low-inertia systems [47]. *One of the outstanding challenges for synchronverter technology is, however, how to achieve decoupling of the active (P) and reactive power (Q) [39];* in the original development of the technology, the synchronverter was connected to a *strong* grid and thus, the PQ coupling effect was not recognized appreciably.

The PQ decoupling problem is particularly timely because the increasing penetration of RES in power systems is accompanied by an associated decrease in the short circuit level (SCL) [48] and, thus, an overall *weakening* of the grid. WTG and SPV systems, for example, generate short-circuit fault currents in the order of one fifth of those for large

coal and gas-fired units [49]. A decrease of SCL signifies an increase in the resistive component of the grid, which results in a resistive or inductive–resistive system. Hence, a weak grid is characterized by a low X/R ratio [50]. *In these weak grids, P and Q have a strong coupling effect which requires an effective PQ decoupling technique for their independent control*.

A literature survey, presented in chapter 3, shows that many of the proposed PQ decoupling methods lacks practical applicability due to the complexity of tuning the controller [51, 52]. The use of the virtual impedance, however, is promising. This has therefore gained attention to many researchers [53–61]. Most of these researches have been performed on islanded systems and *inertia emulation was not considered* [53–57]. Moreover, the studies do not provide theoretical background on what type and magnitude of the virtual impedance are required. This results in complexity in sizing of the required magnitudes of the virtual impedance. Furthermore, the relationship between the PQ decoupling scheme and required magnitudes of the virtual impedance need to be established. *This research, therefore, bridges this gap and develops a simple and practical PQ decoupling scheme for a VSG–synchronverter connected to a weak grid.*

Another timely challenge for the VSG is the provision of the low voltage fault ride through (LVRT) while maximizing the power transfer. A VSG is required to remain connected to the grid on the occurrence of voltage sags. This is important in a system with high penetration of RES in order to avoid *cascading failure* which might result in a blackout. This is a stringent requirement for the VSG because–the large currents that flow in the response to voltage sag are potentially damaging to the equipment. It is proposed in some literature [62–66] to limit this current to its rated value. This, however, result in a limited power transfer with a poor transient response, which might aggravate power imbalance and results in a cascading failure. Alternatively, the power transfer can be improved using an active superconductor fault current limiter (SFCL).

The idea of an active SFCL was introduced in [67]. A number of researches [67–69] have investigated the use of the active SFCL in distribution and transmission systems. These researches, however, are limited to the islanded systems, where the design is aimed at limiting the fault current rather than providing a LVRT. Moreover, PSO requires a VSG to be able either to supply active power (P), reactive power (Q) or PQ during LVRT contingent to the level of the voltage sag. This was not studied in the latter

literature's. On other hands [70] considered a grid connected VSG. The proposed active SFCL involved addition of the resistive impedance during fault. This, therefore, requires a proper coordination between the virtual impedance and the added impedance during LVRT. This was left as a future work in [70]. *This research therefore develops a new LVRT technique for a grid connected VSG–synchronverter using an active SFCL*. This is achieved by coordinating between the virtual impedance through the PQ decoupling scheme and an active SFCL.

1.4 Research questions

The following four research questions are summarised from sections 1.1 and 1.3;

RQ1. What are the operational and frequency control challenges of the power system with high penetration of RES?

This question aims at exploring the challenges of operating a power system with high penetration of RES-generations. Moreover it explores the state of art measures deployed by PSO to operate low inertia power system, their challenges and hence, investigating the emerging and the future operational trends.

RQ2. How can a VSG be controlled in a power system with high penetration of RES generators, that is in a weak grid?

High penetration of RES generators in a power system results in a weak grid. A VSG connected in these systems is faced with a coupled PQ control problem. Therefore, this research question aims at exploring effective PQ decoupling methods for a VSG connected to a weak grid.

RQ3. How can a VSG connected to a weak grid provide an effective low voltage fault ride through (LVRT)?

In the occurrence of the voltage sags, a grid connected VSG is required to remain connected to the grid. Moreover, it is required to aid the grid to recover to its state prior to the occurrence of the voltage sags. This requires a LVRT strategy to be encompassed with the VSG design. This question therefore, aims at exploring the LVRT methods for a VSG connected to a weak grid, in particular it explores LVRT

technologies that can enhance power transfer with a minimum transient response during LVRT.

RQ4. How can a time varying inertia be estimated in a power system with high penetration of RES?

This research question aims at reviewing the existing methods for inertia estimation and their challenges in the power system with high penetration of RES generations. Moreover, it explores a suitable online estimation method for adaptive inertia frequency protection scheme for the weak grid.

1.5 Research objectives

1.5.1 Main objective

To develop control methods for a virtual synchronous generator (VSG) connected to a power system with high penetration of RES generations–a weak grid.

1.5.2 Specific objectives

i. To analyse operational challenges of a power system with high penetration of RES-generations.

ii. Modelling of the VSG and development of the decoupled PQ control for a VSG connected to a weak grid.

iii. Development of the low voltage ride through strategy for a VSG connected in a weak grid.

iv. Development of an online inertia estimation method for adaptive inertia control of the VSG connected to a weak grid.

1.6 Main contributions

i. A comprehensive review on the operational challenges of a power system with high penetration of RES is presented. Moreover, this details the state of art mitigative measures deployed by the PSO and their corresponding challenges, as well as

the future trend on operating a low inertia power system. These are presented in chapter 2.

ii. Modelling of the VSG and parameter sizing of its virtual stator is presented in chapter 3.

iii. A new PQ decoupling scheme for a VSG connected to a weak grid is presented in chapter 3. The implementation of the scheme and simulation results in a representative loading scenarios are provided to validate the efficacy of the scheme.

iv. A new LVRT strategy using a FCS-MPC based active SFCL is presented. The strategy maximises power transfer during LVRT with a better transient response. Simulation results are provided to support the validity of the strategy. These are presented in chapter 4.

v. A new neural network based online estimation of the stochastic inertia in a power system with high penetration of RES is presented in chapter 5. The method can perform online estimation of the inertia of the power system with high penetration of RES. Inertia is explicitly estimated which provides a potential for adaptive inertia control of the VSG connected in a weak grid.

1.7 List of publications

i. D. A. Kisinga, P. Makolo and P. Trodden, "A Neural Network-based Online Estimation of Stochastic Inertia in a Power System," 2022 IEEE PES/IAS PowerAfrica, Kigali, Rwanda, 2022, pp. 1-5, doi: 10.1109/PowerAfrica53997.2022.9905270.

ii. D. A. Kisinga and P. Trodden, "Virtual power circle based PQ decoupling technique for a virtual synchronous generator connected to a weak grid," 2023 IEEE Belgrade PowerTech, Belgrade, Serbia, 2023, pp. 01-06, doi: 10.1109/PowerTech55446.2023.10202828.

iii. D. A. Kisinga and P. Trodden, "A low voltage ride through (LVRT) strategy using an active superconductor fault current limiter (SFCL) for a virtual synchronous generator (VSG) connected to a weak grid," 2023 IEEE PES Innovative Smart

Grid Technologies Europe (ISGT EUROPE), Grenoble, France, 2023, pp. 1-5, doi: 10.1109/ISGTEUROPE56780.2023.10407439.

iv. Kisinga, DA, Makolo, P. and Trodden, P. (2024). A modified synchronverter for a weak grid with virtual power circles-based PQ decoupling scheme. IET Renewable Power Generation .

v. D. A. Kisinga and P. Trodden "A LVRT strategy using a FCS-MPC based active SFCL for Virtual Synchronous Generators," (to be submitted).

1.8 Thesis structure

The rest of this thesis is organised as shown in Fig. 1.2 and a brief description is given in the sequel;

Chapter 2 summarizes frequency control in power systems. It highlights the measures that PSO have so far undertaken in operating low inertia power system, discusses the corresponding challenges for control, and identifies future trends for operation of the low inertia power systems.

The future trend of operating low inertia power systems involve deployment of the VSGs. Chapter 3, therefore, provides a systematic design for the class of the VSGs known as synchronverter. Specifically, this details the design of the virtual stator–the VSG to grid interfacing LCL filter. Moreover, the PQ coupling problem for the VSG connected to a weak grid is analysed. This includes the critical literature review on the state of the art methods of the PQ decoupling methods and introduction of the *new virtual power circles based PQ decoupling technique for a synchronverter connected to a weak grid*. The modifications of the conventional synchronverter to accommodate the virtual power circles based PQ decoupling technique are presented in this chapter. This is accompanied by simulation results in the representative loading scenarios, as well as during mild frequency and voltage variations.

A VSG is required to aid the grid to recovery to its nominal state when faults such as voltage sags occur in the grid. To achieve this, a VSG must have a LVRT capability. The state of art methods for achieving a LVRT for the VSGs are analysed in *Chapter 4* with their corresponding drawbacks. Then, chapter 4 continues by presenting *a new LVRT strategy using a finite control set model predictive control (FCS-MPC) based*

an active superconducting fault current limiter (SFCL). With this strategy the VSG can ride through both mild and severe faults while maximising power transfer. This is achieved through a coordinated control between the FCS-MPC based the active SFCL and the virtual power circles based PQ decoupling scheme. Finally, chapter 4, presents simulation results to support the validity of the proposed LVRT strategy. This is done with accordance to the surveyed grid codes which detail the PQ requirement during LVRT under different conditions of the voltage sag.

While Chapter 3 and Chapter 4 focus on the design and control of the VSG connected to the weak grid, chapter 5 focuses on estimating inertia in a weak power grid. It starts by providing the importance of estimating inertia in a power system with high penetration of RES. Then, it presents the critical literature review on inertia estimation methods in EPS. Finally, it presents *a new neural network based method as a way forward for stochastic inertia estimation in the low inertia power system*. The method can explicitly estimate inertia online in the power system with high penetration of RES. This is validated using a modified New England power system in the DigiSILENT Powerfactory environment. This provide basis for designing inertia adaptive VSG.

Chapter 6 Closes this thesis by drawing conclusions and providing potential future research works.

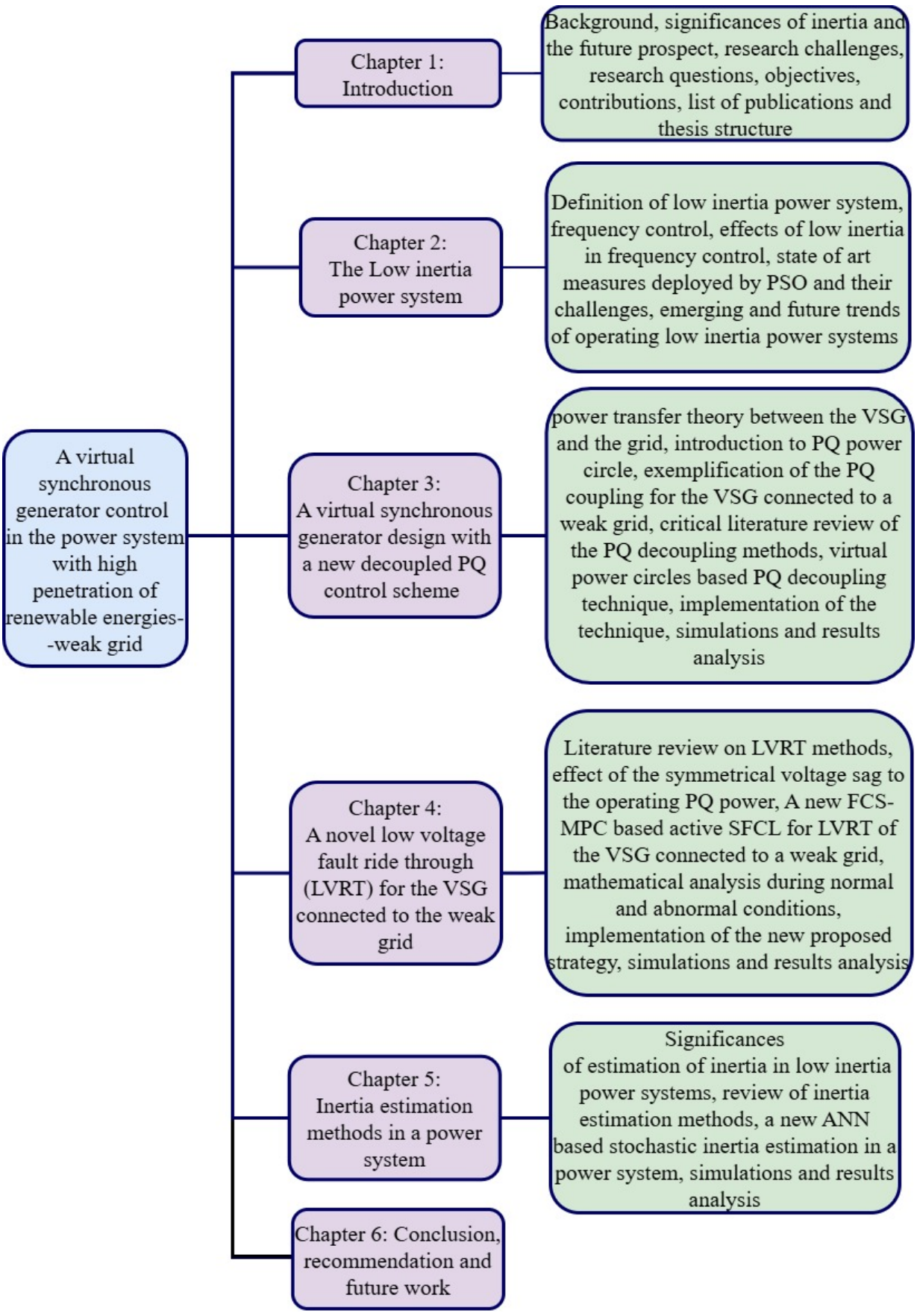

Figure 1.2: *Thesis structure*

Chapter 2

The Low Inertia Power System

This chapter provides a thorough background on frequency control in power systems. It describes the operational challenges of the low inertia in power systems. The state of art measures that PSO have deployed and future trends are also discussed. Hence, it lays a fundamental basis for the future researches on the low inertia power systems.

2.1 Introduction

Before embarking into the operational challenges of the low inertia power system, its definition is provided in this section. The decline of inertia in power systems is primarily caused by the high penetration of the RES generations that are inertia–less or whose inertia is decoupled by the power electronic converter (PEC). Moreover, the decline of inertia is also caused by the decoupling of the contribution of inertia from the demand side by the PECs. Therefore, in this context a low inertia power system is defined as *the power system characterized by both high penetration of the PECs interfaced RES generations and a high penetration of the PECs in the demand side*.

As mentioned in chapter 1, *inertia* plays an important role in the frequency control of a power system. Frequency control is required to maintain operation of the system close to or around its rated frequency. The over frequency and under frequency operation of a power system has detrimental impacts to both, the system and the users of the electric power. For example, under-frequency operation can results in high magnetizing currents in transformers and induction machines [71]. The resulting high currents can damage windings of these machines. Moreover, operation of the industrial motors that are directly

connected to the system depends on the system's frequency. Hence, over frequencies and under frequencies can result in over speeding and under speeding of the motors, correspondingly. This can create mechanical stresses that can even damage the motors. It is therefore, significant to maintain frequency within its nominal specified range.

It can, thus, be concluded that the influx penetration of the inertia-less RES in power systems have eroded and continues to erode frequency control in these systems. This causes operational and control challenges to the power system operators (PSO). These challenges have already been noticed and experienced in some of the power systems. As RES penetration continues to grow, these challenges become more significant and urgent to address. Hence, some measures must be put in place. Therefore, this chapter explores precisely the challenges that PSO face. Moreover, it sheds some light on the mitigating measures that PSO have undertaken so far. Lastly, it covers the future trends for operating the low inertia power systems. Hence, this provides basis for the development of the new researches and solutions to these challenges.

The rest of this chapter is organized as follows; Section 2.2 reviews frequency control in power systems as a basis for understanding the challenges of operating a low inertia power system. The effects of decline in inertia on frequency control is provided in Section 2.3. The operational challenges of the low inertia power system are highlighted in Section 2.4. Section 2.5 reviews the state-of-the-art measures that have been introduced or adopted by the PSOs, and also outlines the corresponding limitations and challenges. Finally, emerging and future technologies for the low-inertia mitigation in power systems are discussed in Section 2.6.

2.2 Frequency control in power systems

Grid codes specify the acceptable range of frequencies for the power systems operation. For example in Britain, the statutory limit specifies that the frequency should be maintained within 1% of a nominal level (i.e. 50 Hz), despite any disturbances and frequency contingencies that might occur. In a power system, the frequency variations can be caused by the stochastic nature of the demand or by the disturbances such as loss of generation or faults in the system. Hence, effective frequency control is necessary in order to ensure grid codes are adhered to. Essentially, frequency control is divided into four control

zones acting at different time scales from the onset of the disturbance [2]. These control zones are; *inertia response, primary control, secondary control and tertiary control.*

2.2.1 Inertia response

Inertia serves as the first line of defense against frequency disturbances in power systems. In conventional power systems, it is primarily provided by the rotating masses of synchronous generators (SGs). This inherent characteristic ensures an instantaneous response to frequency deviations, acting without the need for external control mechanisms. Inertia effectively limits the rate of change of frequency (RoCoF) immediately following a disturbance, buying critical time before any control systems take action.

The inertial response typically lasts for a brief duration, up to approximately 5 seconds after the disturbance [72]. During this period, it plays a crucial role in stabilizing the system by reducing rapid RoCoF, ensuring grid stability before secondary mechanisms, such as governor or automated control responses, activate. This rapid and automatic behavior underscores the importance of inertia in maintaining the reliability and robustness of modern power systems, particularly in the face of increasing renewable energy integration.

2.2.2 Primary frequency control

Primary frequency control refers to as the response of the synchronous generator (SG) in containing frequency deviations by regulation of its output active power. This is performed by the generator with a reserve capacity. Hence, it is also referred to as frequency containment reserve (FCR). It is achieved through governor control, that is, as the imbalance persists following inertia response, the speed of the SG changes. To restore the speed of the rotor of SG, the control governor opens the control valve to increase or decrease the prime mover, for example steam flow in a thermal SG. In so doing, the output power of the SG changes correspondingly and hence, the speed (and thus frequency) is recovered to its nominal value. In Britain, the governor control is activated within 2 seconds and should provide a full increased output power within 10 seconds following a frequency contingency [25]. The primary frequency control lasts for 30 seconds following an imbalance as shown in Fig. 2.1.

2.2.3 Secondary frequency control (SFC)

The purpose of the secondary control is to restore the system frequency to its nominal value. This is due to the incapability of the FCR to restore the system's frequency to its value before the occurrence of the frequency contingency. This is because the primary control loop is merely a proportional control response i.e. without integral action. Therefore, the secondary response is activated after 30 seconds following the imbalance and on the persistence of frequency deviation from its value before the imbalance. This is achieved by using a central control system, that is automatic generation control (AGC), that monitors several generators in the area. The AGC specifically changes the generator set points and recovers the system frequency [73]. Moreover, SFC ensures that the FCR is made available again for the later utilisation. The SCR lasts for only 15 minutes following its activation [72].

2.2.4 Tertiary frequency control

The purpose of the tertiary frequency control is to restore the secondary frequency control reserve and or providing desired economical operations of the generating units [73]. In most occasions, it is performed manually following the commands by the PSO. It also involves initiation of the generation units for providing a spinning reserve based on the forecasted events. Hence, the tertiary frequency control is ensured by both spinning and non-spinning reserves. Figure 2.1 provides the frequency control zones with their corresponding time scales.

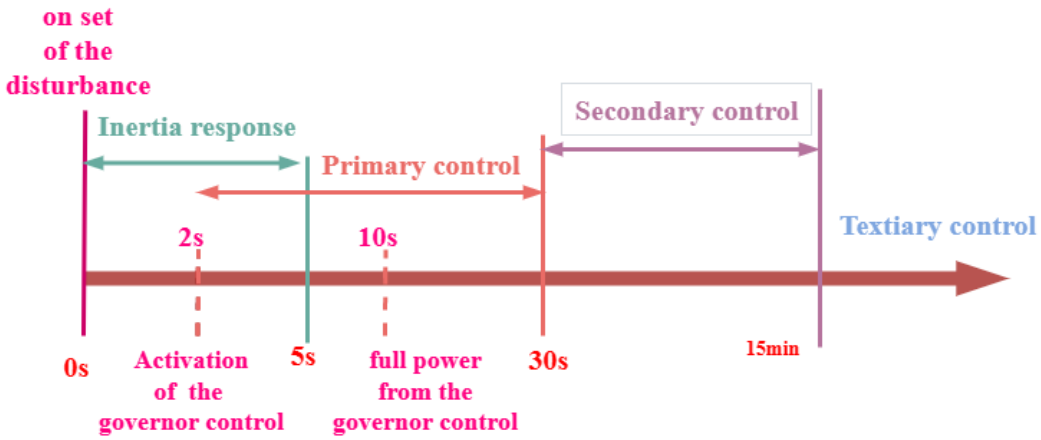

Figure 2.1: *Frequency control zones with their corresponding times scales in a power system*

2.3 Effects of the decline of inertia in the frequency control in a power system

The system inertia limits how fast the frequency changes (*i.e.,* RoCoF) following the occurrence of a frequency contingency. This is evident from the swing equation that (approximately) governs the dynamics of the frequency deviations (from nominal), Δf:

$$H\frac{\mathrm{d}(\Delta f)}{\mathrm{d}\,t} + D\Delta f = \frac{\Delta P}{S^{\text{base}}} \tag{2.1}$$

where H is the inertia constant, $\frac{d(\Delta f)}{dt}$ is the RoCoF, D is the damping, Δf is the relative frequency deviation, ΔP is a disturbance which marks the change in active power in the system, and S^{base} is the base power. For the same ΔP, RoCoF varies inversely with the inertia constant:

$$\frac{\mathrm{d}(\Delta f)}{\mathrm{d}\,t} = \frac{1}{H}\frac{\Delta P}{S^{\text{base}}} \tag{2.2}$$

from a steady state with $\Delta f(0) = 0$. Hence, the larger the inertia constant, the smaller the RoCoF, and, hence, the frequency nadir in response to disturbances. Therefore, a reduction in system inertia results in the proneness of the system to the frequency instability due to the increased RoCoF and its corresponding frequency deviation.

To illustrate the effects of the decline of the inertia in the power system's frequency response, Fig. 2.2 shows the time-response for system governed by the swing equation (2.1) following a disturbance, as the inertia constant H is reduced from nine seconds to 1.8 seconds; these values are based on the anticipated decrease of inertia in the GB system, which has been predicted to reach 3 seconds (down from 9 seconds in 2008) during the early 2020s [24], and fall as low as 1.8 seconds by 2025 [25]. It is clear that as inertia decreases the RoCoF increases and higher frequency deviations are observed; moreover, oscillations become more pronounced and settling times increase. These pose operational challenges to the PSO.

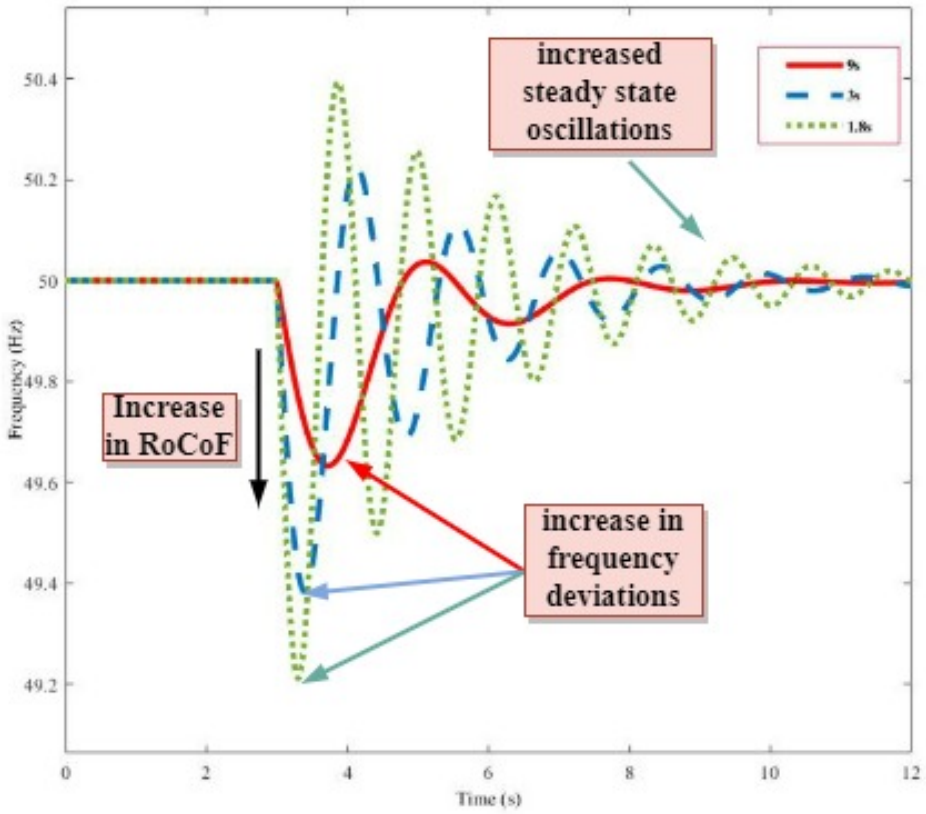

Figure 2.2: *The frequency response of a power system as inertia decreases progressively*

2.4 Operational challenges of the low inertia power system

It is important to provide a holistic review of the challenges caused by the decrease in inertia of the power system, as well as by the stochasticity of both generation (RES) and the demand. This forms a basis for exploring solutions to the future low-inertia power systems operations. Figure 2.3 depicts the operational challenges faced by the PSOs as the system inertias decrease while RES penetration increases. Each of these challenges is discussed in remainder of this section.

2.4.1 Decline in spinning reserve (SR) and dispatchable units

Spinning reserve is an unused synchronized capacity that can be dispatched and affect the active power in the system [74], and as such it has played a key role in the operation and control of a traditional power system. It provides protection against power systems

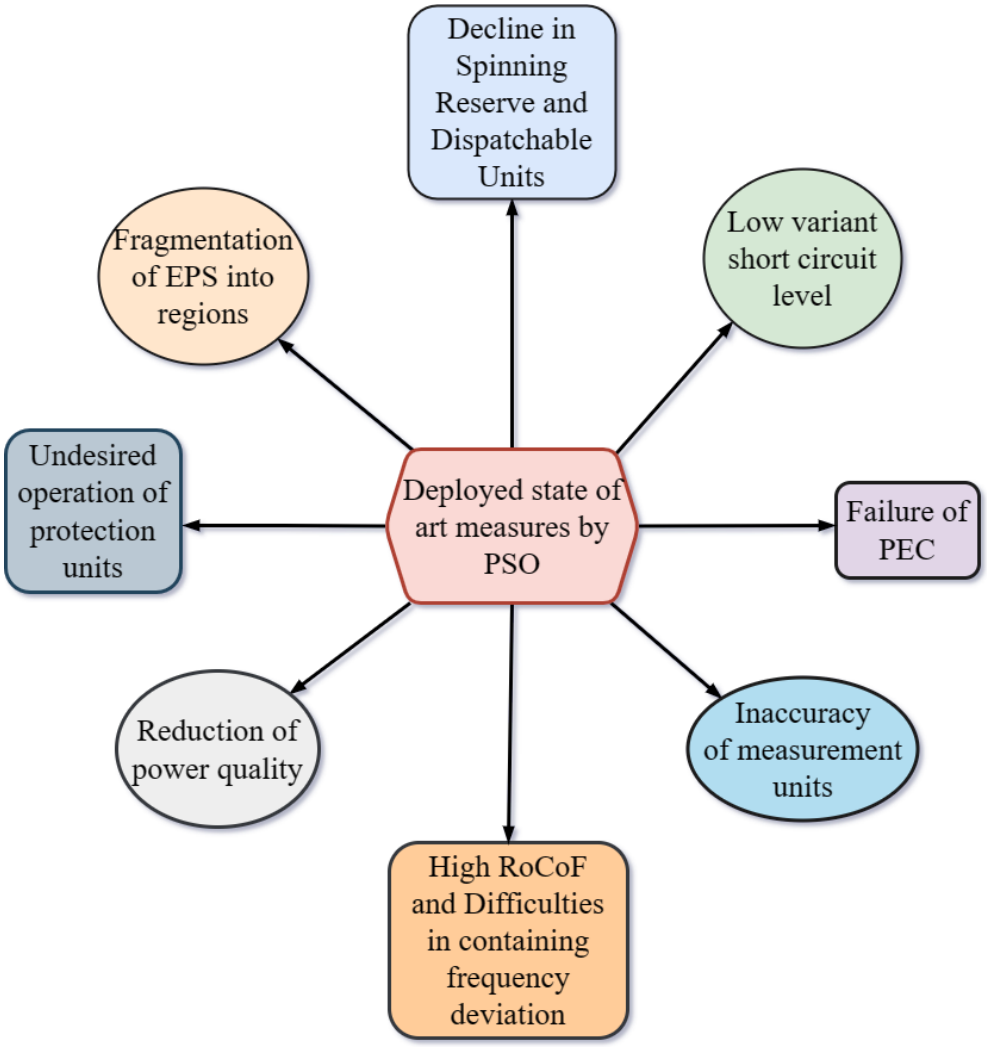

Figure 2.3: *Operational challenges of the Low inertia power system*

reaching unsafe frequency deviations following a frequency contingency, such as an unpredictable increase in demand or loss of the supply [75–77]. This is achieved by providing a reserve of inertia as well as active power that can be dispatched for primary and secondary frequency control [78]. Hence, a power system with higher SR is more reliable with the reduced probability of loss of demand than the one with low SR. Therefore, it is imperative that PSOs ensure sufficient SR is available in the system, and a reliability metric known as Planning for Reserve Margin (PRM) has been used to quantify and set requirements on this availability; in Taiwan, for instance, a statutory limit of 15 percent is required for the successful power system operation [79].

The increased integration of renewable energy sources (RES), which lack the inherent rotating mass of synchronous generators (SGs) connected to the grid [22], results in

a corresponding reduction in system inertia and synchronous reserve (SR) [78, 80]. Beyond this reduction, the stochastic nature of RES introduces further variability in SR by influencing the number of committed SGs. This variability makes it difficult to precisely quantify SR requirements. Additionally, many RES operate at Maximum Power Point (MPP), which means they have no reserve power available for dispatch in the event of frequency contingencies [81]. Although RES can technically provide extremely fast response times, their role as dispatchable units is hindered by economic considerations [82]. To create power reserves, RES output could be curtailed, but this leads to inefficiencies, financial losses, and reduced productivity [83].

In terms of economic operation, RES are often treated as non-dispatchable. The high costs associated with output curtailment or managing variability make it less viable to treat RES as dispatchable units in practice [84]. Moreover, RES are also challenged by operational limits, such as wind turbines' cut-off speeds, where they must shut down during high winds, complicating their dispatchability during grid contingencies [85]. Dispatchable units and SR have been vital tools in ensuring power system resiliency against frequency contingencies and meeting system's demand. Therefore, their decline poses new operational challenges to PSOs in mitigating frequency contingencies and satisfying demands reliably and securely.

2.4.2 Difficulties in limiting RoCoF and containing frequency deviation

In the traditional power systems, SGs provided sufficient inertia to limit RoCoF. Moreover, availability of sufficient SR and dispatchable units ensured that the frequency deviation could always be contained within limits. Limiting RoCoF and containing frequency deviation in efficient and economic fashion in the low-inertia power system is more challenging [25]. This is due to the increased RoCoF, while limited time and resources (SR and DU) are available to limit the frequency excursions. This can trigger the operation of the under-frequency load shedding (UFLS) and RoCoF relays, which may result in a cascading failure and even a blackout. A number of countries have witnessed high frequency deviations in the last decade; this is exemplified by the blackouts in Australia in 2016 and UK in 2019.

2.4.3 Undesired operation of the protection units

Low inertia in power systems ramifies more frequency oscillations [86] as the results of the stochasticity of both demand and generation. This stresses protection units in the system. Moreover, following a disturbance with marginal reserve in the system, high RoCoF and large frequency deviations are expected. Therefore, this can result in an undesired operation of the RoCoF relays and UFLS relays [87, 88]. To prevent this undesired operation, some countries have extended RoCoF relay to a wider settings (as detailed in Section 2.5.1). However, adoption of and adherence to these new codes has been particularly challenging for the new distributed generation (DG) providers. In [88], the high cost for RoCoF testing in generators is said to be a major hindrance. In Australia, thousands of the customers' installed PV inverters have default UFLS relays settings that do comply with relaxed grid codes; in the event of a frequency excursion which is within acceptable limits defined by the relaxed code, these relays are undesirably still activated [89, 90]. A similar observation is reported in GB, where some DGs are still operating according to old grid codes despite the introduction of relaxations [87].

2.4.4 Inaccuracy of the measurement units

Operation of a power system relies on the accuracy of its measurements for control and protection purposes. This becomes more significant as power grids morph into *smart* grids; a smart grid is self-healing network that uses real-time measurements for optimal operation of the system. For example, operation of the UFLS and RoCoF relays depend on the accurate measurement of frequency. However, reduction of inertia signifies faster dynamics in the system particularly in terms of the RoCoF. Therefore, measuring units are required to take measurements more rapidly which may introduce errors. This can result into wrong control decisions in the system [25].

2.4.5 Reduction of the power quality

Power quality refers to the characteristics of electrical power—such as voltage, frequency, and waveform integrity—that ensure the reliable and efficient operation of connected devices [91]. Key indicators of power quality include voltage sags, swells, harmonic distortion, flicker, and unbalances. Reduction of the power system inertia has serious

repercussions for the power quality of the system. The serious concerns on the power quality of the low inertia power system is caused by its proneness to fluctuations. The problem is exacerbated by the stochasticity of both RES and the demand in the system: this can introduce significant voltage flicker [19, 92]. Moreover, in these converter-dominated networks, power quality issues are more pronounced due to the nonlinear characteristics of power electronic devices. These devices can introduce significant harmonic distortion, particularly under high penetration of renewable energy sources (RES) [93, 94]. Harmonics can lead to overheating in equipment, increased losses, and interference with protection systems [95]. Generally, the interaction of stochastic RES, PEC-induced harmonics, and reduced system inertia poses significant challenges to maintaining power quality.

2.4.6 Fragmentation of a power system into regions

Higher penetration of RES results in the fragmentation of a power system into weakly connected and strongly connected areas. This is owing to the geographical dispersion of the RES and the corresponding decrease in inertia and damping; coupling between areas/machines may be weakened. This results into regional variations of the frequency and RoCoF in the system [25]. Thus, when a disturbance occurs in the system, measurements units can detect different RoCoFs depending on their location [96]. This fragmentation of the system poses operation challenge to the power system as it marks the increasing of inter-area oscillations [97]. For example, in [98] the effects of wind penetration in a five-area power system model is studied. It is concluded that high penetration reduces damping and hence increases inter-area oscillations. Several historical blackouts are reported to be caused by inter-area oscillations; for example, the 1996 USA blackout [99].

2.4.7 Weak grid with a low variant short circuit level (SCL)

A weak grid refers to a grid characterized by low system strength, often measured using the Short Circuit Ratio (SCR). SCR is defined as the ratio of the available Short Circuit Level (SCL) at the point of connection to the rated power of an inverter-based resource [100]. The SCL represents the amount of current that flows during a fault in the system, serving as an indicator of the system's ability to handle and recover from disturbances [49]. A high SCL signifies a robust system with quicker fault recovery,

whereas a low SCL indicates a weaker grid with slower recovery times and heightened vulnerability.

The ongoing transition to low-inertia power systems dominated by renewable energy sources (RES) has markedly decreased SCL's. Inverter-based generators, such as wind turbines and solar photovoltaic, contribute significantly less fault current—up to five times lower—compared to traditional synchronous generators like coal and gas plants [48, 49]. The reduction in the fault current in weaker grids can lead to the failure of protection systems to operate correctly, resulting in sustained overloads or faults that can compromise system stability. Moreover, the stochastic and intermittent nature of RES causes SCL values to fluctuate over time, further complicating system operations and challenging grid stability [101].

A low SCL in weaker grids exacerbates voltage profile management issues. During a fault, voltage levels drop, and the slower recovery associated with low SCL can allow these voltage depressions to propagate, increasing the risk of generator tripping and widespread instability [48, 49]. Furthermore, the absence of synchronous generators in low-inertia systems eliminates a major source of fault current, further reducing SCL and, consequently, SCR. This weakened state makes the grid more susceptible to voltage instability, harmonic distortions, and operational challenges, underlining the critical need for advanced solutions to maintain power quality and reliability.

2.4.8 Failure of power electronics converters

Power electronic converters (PECs) are a key enabling technology for the penetration of the RES in the power systems. Most RES technologies, for example solar photovoltaic (SPV), generate DC power. PECs provide suitable power control and enable the integration of such RES to the grid. In a low inertia power system, fast frequency responsive (FFR) devices (as detailed in Section 2.6) depend on the fast operation of the PECs; this also includes the possibility of the RES on the demand side, such as Electric Vehicles (EVs), participating in providing frequency support. Therefore, PECs play an underpinning role in the operation of the future low-inertia power system [102, 103]. However, PECS are prone to failures [104–106]. These failures are primarily caused by the fragility of the components of the PECs, in particular capacitors and power semiconductor devices. For example, [107] reports that PECs contribute to one fourth of the failure rates in wind

turbine systems. This challenges the operation of the low-inertia power system, and hence compromising its ability to reliably deliver electrical energy [108–110].

2.5 The deployed state-of-the-art mitigative measures for operating the low-inertia power systems and their challenges

This section reviews the state of the art in techniques PSOs are deploying in mitigating against the challenges of the low inertia; Figure 2.4 highlights the techniques discussed in the sequel.

2.5.1 Extension of the RoCoF relay settings

To mitigate the undesired operation of the RoCoF relays and minimizing the islanding of the distributed generations, PSOs in different countries have extended RoCoF relays to a wider settings. For example, in GB RoCoF relay requirements have been changed from $0.125\,\mathrm{Hz\,s^{-1}}$ over $0.5\,\mathrm{s}$ to $1\,\mathrm{Hz\,s^{-1}}$ over the same period [25, 87]. EirGrid in Ireland has made a similar modification, going from $0.5\,\mathrm{Hz\,s^{-1}}$ over $0.5\,\mathrm{s}$ to $1\,\mathrm{Hz\,s^{-1}}$ [13, 111]. The Australian grid code for RoCoF has been modified to define an automatic access standard of $4\,\mathrm{Hz\,s^{-1}}$ over the window of $0.25\,\mathrm{s}$ and a minimum access standard of $1\,\mathrm{Hz\,s^{-1}}$ for $1\,\mathrm{s}$ [88]. Moreover, the UFLS settings have been changed from 1% deviation from nominal frequency to 2% of the same [89, 90]. Despite these extensions, the adoption and implementation of the new settings pose many challenges. In [88] it is stated that the cost of RoCoF testing of generators is too high, while in Australia thousands of installed PV inverters from customers have UFLS relays set according to old grid codes [90]. A similar case is observed in GB where the DGs are still operating with the old RoCoF relay settings [7].

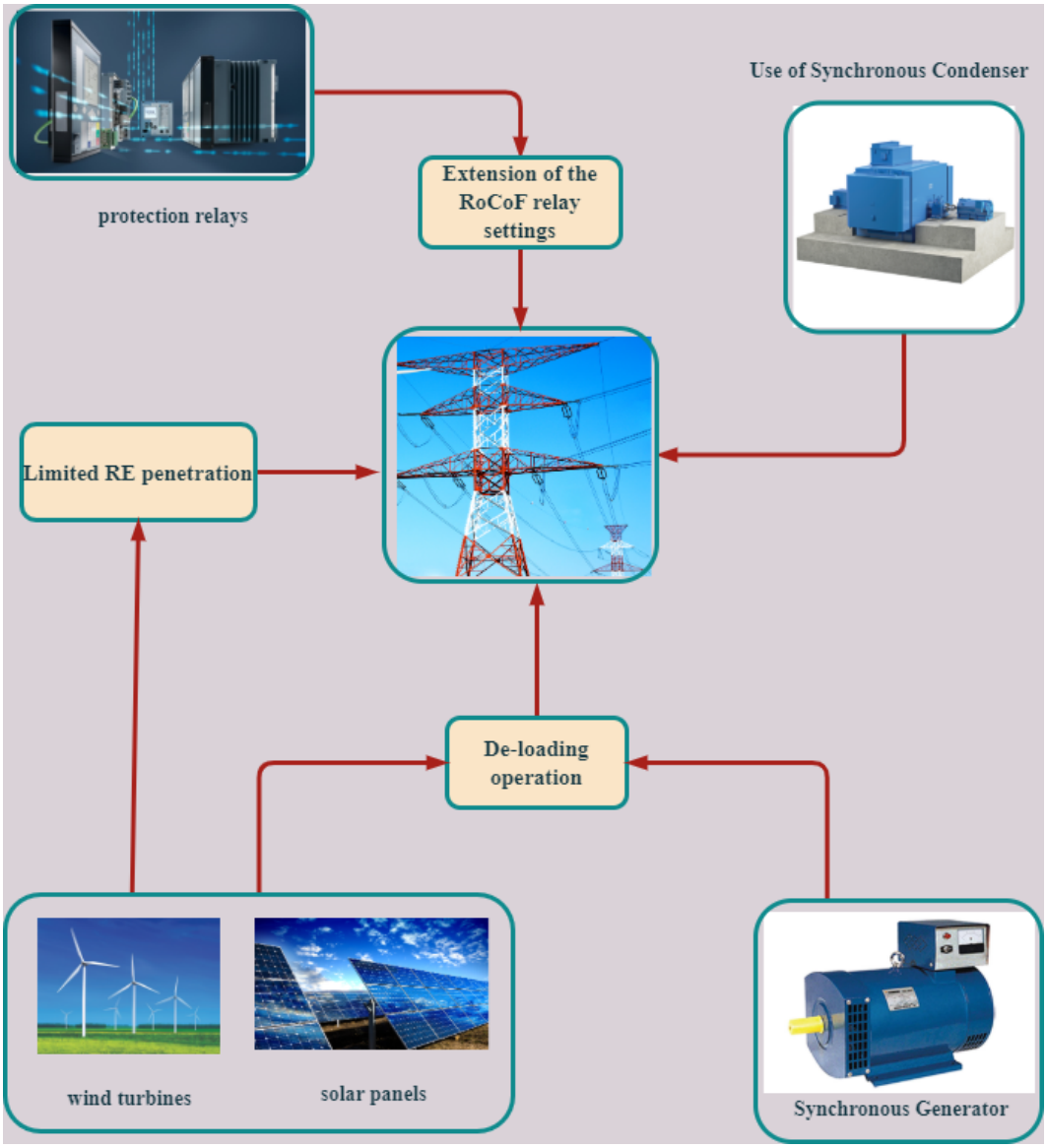

Figure 2.4: *State-of-the-art operational mitigation measures against decline of inertia in power systems.*

2.5.2 De-loading of generating units and use of synchronous compensators

In order to deal with the decline in reserve and to enhance availability of the dispatchable units for limiting RoCoF and frequency deviation, PSOs may de-loade the generating units or make use of the synchronous compensators (SCs) [87, 112]. De-loading entails operating generating units below their maximum output capacity; in the case of RES, this means curtailing operation below MPP [28]. For example, in the GB network inertia is

estimated and the ability of the system to withstand largest loss is evaluated [7]. This then allows the estimation of the required amount of the de-loaded generation to be dispatched for additional inertia support. This technique can lead to a high cost for the system operation, and increasingly so as the penetration of RES rises. For example, in [25] it is reported that the annual cost for this provision across the GB network has increased from £600 million in 2017/2018 to £1500 million in 2018/2019. Additionally, de-loading of the RES can results in high power losses, raising the transmission, and hence unit cost of the electrical energy; hence, the technique is considered uneconomical [80]. Moreover, the technique can be unreliable due to the intermittent nature of the RES generations.

Synchronous compensators (SCs) are synchronous motors, which historically have been used for reactive power compensation in electrical networks [112]. Additionally, SCs can improve the short circuit level in the system [23, 113]. However, since SCs are composed of rotating masses directly connected to the grid they have the potential to raise system inertia and, more generally, participate in frequency support; a number of studies have demonstrated their capability for providing inertia support in the low-inertia power systems [23, 112, 113]. Unfortunately, the use of the SCs for the inertia and frequency support remains expensive due to high investment and operating costs [88].

2.5.3 Limitation of RES penetration in the power system and its instantaneous power generation

The decrease in inertia is mainly due to the high penetration of inertia-less RES. Therefore, PSO in some countries have imposed limits on the percentage penetration of RES to ensure sufficient inertia is available to limit frequency excursions. For example, the EirGrid operator in Ireland instigated a penetration penetration liafter the penetration of RES of RES reached 60% in 2017 [72]. In addition, EirGrid introduced operational metrics to limit the instantaneous contribution of RES power to the system, as detailed in [111]. Currently, [28] says that it is not feasible to operate the Croatian power system with penetration of RES of more than 50%. It should be noted that penetration limits encourage curtailment operation in the event that RES exceeds the limit. Therefore, the technique is not supportive towards 100% RES.

2.5.4 Converter-based frequency support services

In power systems with a high penetration of renewable energy sources (RES), power electronic converters are essential to integrate these resources into the grid. When equipped with advanced control strategies, these converters can effectively provide vital frequency support services. The key prerequisite for such functionality is access to an instantaneous energy source, enabling rapid power injection or absorption to counteract frequency fluctuations [114]. This capability can be achieved by interfacing the converters with energy storage systems such as batteries or supercapacitors. Through proper reserve allocation and control, converters can offer both short-term frequency stabilization, such as inertia emulation and fast frequency response, as well as long-term services like peak load management.

A notable example is the Hornsdale Power Reserve in South Australia, which illustrates how converter-based systems can deliver synthetic inertia and frequency support, significantly contributing to system stability during grid disturbances [115]. Similarly, in Great Britain (GB), the Enhanced Frequency Response (EFR) service highlights the role of converter-based technologies in frequency regulation. Introduced by National Grid ESO, EFR focuses on maintaining frequency stability by providing a full response within one second or less [116]. Grid-scale battery systems, leveraging their instantaneous and precise response capabilities, are key participants in the EFR framework [117].

2.6 Emerging technologies and future trends

Modern low-inertia power systems require fast frequency responsive devices and strategies to contain high RoCoF and frequency deviations. This can be achieved through *inertia-emulation techniques* and demand-side response or management [7, 78, 118]. Inertia emulation is a technique which uses fast acting energy reserve to release or absorb energy, similar to the rotor of a rotating machine. The provided inertia in this fashion is known as *virtual* or *synthetic* inertia. The virtual inertia can be provided from machines, generating units, or energy storage systems (ESS) interfaced with PECs under a suitable control technique. The inertia from rotating machines such as wind turbines and induction motors is decoupled from the grid by the presence of the PECs; however, this concept of the hidden inertia can be emulated in control of the grid-connected PECs

to provide inertia support in the power system. This led to the concept of the *inducverter* and *virtual synchronous machine* (VSM). The inducverter mimics the inertia characteristics of the induction machine while VSM imitates the characteristics of the synchronous machines. In addition to the provision of inertia, VSM can enhance islanding operation of microgrids by providing grid-forming functionality. Detailed analyses of inducverter and VSM are provided in [111], while further details on synthetic inertia can be found in [13, 118, 119].

Demand-side management is proving to be a suitable tool for mitigation against frequency excursions in a low-inertia power system. The demand side can participate in frequency control through providing fast frequency response [120]. This can be achieved through passive or active participation of the controllable loads, such as EVs [121, 122]. The demand side can also participate passively in frequency control through engaging or disengaging loads into/from the grid depending on the form of frequency deviation: thermostatically controlled loads (TCLs), such as refrigerators, are such an example. On the other hand, with the rejuvenation of the power systems into smart grids, bidirectional power flow becomes possible and even likely. Therefore, customers with ESS or with EVs can actively participate in frequency control through vehicle-to-grid mode of operation; therefore, the PSO may encourage consumers to participate in demand-side response [123].

While RES will dominate the future energy mix, another future trend/solution is integrating alternative low carbon solutions like nuclear energy, CCS, and advanced energy storage. Gas turbines with hydrogen blending offer a transitional solution. A hybrid approach leveraging diverse technologies will be key to ensuring a sustainable, reliable, and economically viable energy future. The latter solution is, however, not a subject for this thesis.

In summary, the emerging and the future trend is towards provision of fast frequency responsive controls and inertia emulation techniques. The latter is provided by what is known as *virtual synchronous generators (VSG)*. Considering the time variation of the inertia and the stochasticity of the RES and loads, a real-time monitoring and estimation of the inertia in the system is required. The accurate estimation of system's inertia equips the PSO with situational awareness of the system, which in turn is is vital for the optimisation of resources and deployment of accurate corrective measures [32, 34, 124].

2.7 Summary

Penetration of the PECs interfaced RES generations into power systems is continuously increasing, particularly with the target of 100% renewables in power systems by 2050. This introduction of RES have resulted in the decrease of the inertia of the power systems. Such reduction have negative impacts on the frequency control. This is due to the fact that, RoCoF increases and hence time of containing frequency deviation by PSO decreases. This is amplified by the stochasticity of RES and its non-dispatchability. With the portion of SGs which were used to provide SR being replaced by RES generations, its stochasticity amplifies the problem by affecting the number of SG committed in the system at a time. This together with its non-dispatchability, they mark the decline in reserve for frequency control in power systems. Hence, PSO are faced with operation challenges in containing frequency deviation. Therefore, the proneness to frequency instability of the low inertia power system increases. In this context, various techniques are being deployed by PSO such as relaxation of grid codes, limiting instantaneous RES generations etc. It is a fact that these are temporary measures, the emerging and future trend is towards *virtual enhancement of the system's inertia and provision of the fast frequency responsive control*. This includes enhanced fast frequency control such as adaptive inertia control and participation demand side during frequency contingency.

This research work therefore, explores provision of the virtual inertia in the weak-low inertia power system. It covers the control of the VSG in both normal grid condition and during faults such as on the occurrence of the voltage sags. These are detailed in chapter 3 and 4, respectively. It then, explores technologies for real time estimation of the inertia. This is detailed in chapter 5. The estimate is important for providing situational awareness and hence deployment of the resources by PSO in an economical fashion. Moreover, understanding the inertia status of the system will enable PSO to procure synthetic inertias from the demand side. Furthermore, VSGs may be controlled in adaptive fashion contingent to the available inertia.

Chapter 3

A Virtual Synchronous Generator Design with a New Decoupled PQ Control scheme

VSGs are used to increase inertia of the power systems with high penetration of RES. The continual influx penetration of RES in power syste, however, results in a strong coupling between active power (P) and reactive power (Q). Hence, any VSG technique requires a PQ decoupling technique in order to operate effectively. In this chapter, a new PQ decoupling technique for VSGs basing on virtual shifting of the PQ power circles is presented. Implementation of the technique is as well provided. For verification of the validity of the technique, a VSG is designed and simulation results are provided. It is demonstrated that, the technique achieves a decoupled PQ control for the VSG connected to a weak grid. Moreover, the VSG operated under the the new proposed scheme is capable of supporting frequency and voltage regulation in the grid without inducing large transient grid currents.

3.1 Introduction

A VSG refers to an inverter that mimics the operations of synchronous machine [125]. The concept of this technology was firstly introduced by Becke and Hesse in 2007 [38] and has seen numerous improvements and modifications since; current designs and topologies of VSGs include the virtual synchronous machine (VISMA) [38], synchronverters [39–41], simplified swing equation based VSGs [42], reactive-power frequency based VSGs [43, 44], droop based VSGs [45, 46] etc. They all, however, have the same system configuration consisting of a source of energy such as a RES or an energy storage

system (ESS), an inverter and a control algorithm as shown in Fig. 3.1.

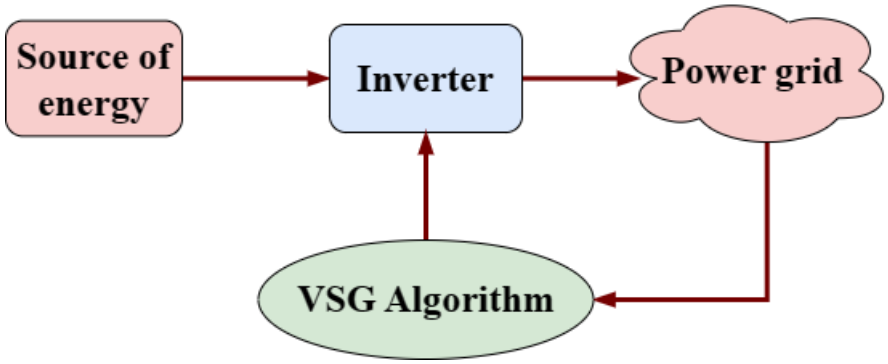

Figure 3.1: *A VSG configuration*

Generally, the topogies of the VSGs are distinguished from one another by the VSG algorithm used. *According to the study by Tamrakar et al. in [47], while comparing the VSG topologies, it was found that synchronverters may provide the best results in terms of limiting RoCoF and frequency nadir in the low inertia power systems. Therefore, this research work considers—the synchronverter's topology—as the VSGs representative topology*. In the original research paper [39] of the synchronverter by Q. Zhong and G. Weiss, one of the outstanding challenges that was left for future researches, is the decoupling of the active (P) and reactive powers (Q) for the synchronverter's PQ control. In their research work [39], the synchronverter was connected to the strong grid and thus, the PQ coupling effect was not recognised appreciably.

The influx penetration of RES generators in power grids, however, results in the decrease of the short circuit levels (SCL) [see Chapter 2, subsection 2.4.7] which weakens the power grid. The decrease of the SCL marks the increase of the resistive components which results in a resistive or inductive-resistive grid. Hence, a weak grid is characterised by a low X/R ratio [50] which is contrary to the conventional power grids. In these weak power grids, P and Q are strongly coupled such that an effective PQ decoupling technique is required for their independent control.

An accurate decoupled PQ control is important for the successful operation of the grid connected VSG. This ensures maximum power is harvested from RES generators and the VSG is supporting the grid during faults, for example on the occurrence of the voltage sags. During normal operations of the grid, power system operators (PSO) require a VSG to operate at unity power factor, that is with zero Q. On the other hand, when voltage

sags occur, a VSG is called upon to supply appropriate amount of Q so as to aid the grid to recover to its nominal voltage. On top of the participation in *Vf*—frequency and voltage regulation, a decoupled PQ control enhances dynamic and stability performance of the VSG, hence preventing an unintentional islanding of the VSGs which might cause cascading failure and hence, a black out [126]. In this chapter, therefore, a new PQ decoupling technique for a VSG connected to a weak grid is presented.

The technique is based on the transformation of a PQ power circle of a VSG connected to a weak grid: first, the PQ power circle is *translated* from its designed position to that of a conventional synchronous generator (SG) connected to a *strong* grid, achieving *a partial* PQ decoupling. Then, to achieve full PQ decoupling, the radius of the PQ power circle in the latter position is further modulated; this is achieved using a series resistance–capacitance–inductance (RCL) circuit which is virtually implemented in the VSG controller. The magnitudes of the components of the RCL PQ–decoupling circuit are easily computed at the desired location and radius of the translated virtual PQ power circle.

The efficacy of the proposed technique is validated using a synchronverter connected to the weak grid in representative loading scenarios. To achieve this, a synchronverter is modelled as per [40] and then, the model is modified for implementation of the proposed technique. These modifications are also provided in this chapter, as well as, the component sizing of the virtual stator of the synchronverter. Contrary to [40], a direct power angle control approach is used to control the modified synchronverter. This offers simplicity not only in the implementation of the technique, but also it removes the complexity of tuning the synchronverter. Moreover, the modified sychronverter being a voltage controlled based VSG can easily synchronise with the grid without using a phase locked loop (PLL). The modified synchronverter model is then implemented in MATLAB/Simulink environment. It is demonstrated that, the technique achieves a decoupled PQ control for the synchronverter connected in a weak grid. Furthermore, the synchronverter operated under the proposed scheme/technique is capable of supporting both frequency and voltage regulation in the grid without inducing large transient grid currents.

The rest of this chapter is organised as follows: Section 3.2 provides the power transfer theory between a VSG and the grid, and it introduces the concept of the PQ

power circle. By using the PQ power circles of the VSG and SG connected to a weak grid and to a strong grid, respectively the problem of PQ coupling is exemplified in this section. The critical literature review of the existing PQ decoupling techniques is presented in section 3.3. Moreover, the latter section presents the proposed virtual power circles based PQ decoupling scheme for a VSG connected to a weak grid. Section 3.4 provides the implementation of the virtual power circles based PQ decoupling scheme. This requires a design of the VSG and its corresponding modifications to accommodate the scheme. These are all provided in section 3.4. Simulation results and their analysis for testing the validity of the virtual power circles based PQ decoupling scheme are presented in section 3.6. Finally this chapter is concluded in section 3.7 by providing its summary.

3.2 PQ coupling effect for power transfer between two AC sources

A VSG is required to transfer power from a RE-generation unit or from the dedicated ESS to the grid. This is equivalent to the power transfer between two synchronised AC sources. Figure 3.2 provides an illustration of AC-voltage source from the terminals of the VSG synchronised to the power grid, while the two are separated by an equivalent impedance $Z(X, R)$.

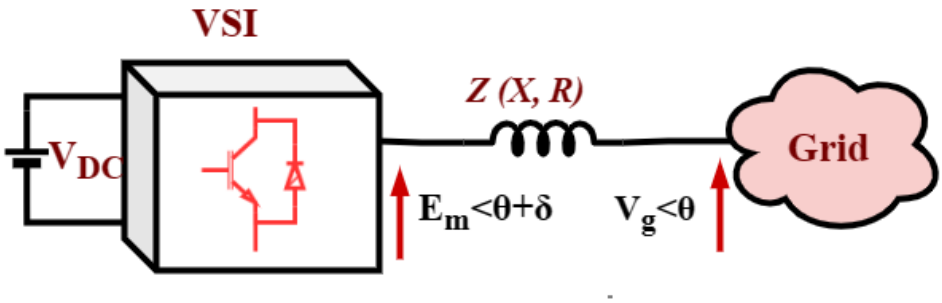

Figure 3.2: *A simplified block diagram of the synchronverter connected to the grid*

Considering Fig. 3.2 and from the power transfer theory, the P and Q transferred to the grid are given by [127],

$$P = \frac{3V_g E_m}{2|Z|}\cos(\alpha - \delta) - \frac{3V_g^2}{2|Z|}\cos\alpha, \tag{3.1}$$

$$Q = \frac{3V_g E_m}{2|Z|}\sin(\alpha - \delta) - \frac{3V_g^2}{2|Z|}\sin\alpha, \tag{3.2}$$

where V_g and θ are the amplitude and angle, respectively, of the grid voltage (V); E_m and $\theta + \delta$ are the amplitude and angle of the internal voltage (E) of the VSG, respectively; Hence, δ is the power angle, that is, the difference of angles between E and V and

$$\alpha = \tan^{-1}(X/R)\ . \tag{3.3}$$

Equations (3.1) and (3.2) can be combined to form a PQ power circle

$$\left(P + \frac{3V_g^2}{2|Z|}\cos\alpha\right)^2 + \left(Q + \frac{3V_g^2}{2|Z|}\sin\alpha\right)^2 = \left(\frac{3V_g E_m}{2|Z|}\right)^2, \tag{3.4}$$

whose centre coordinates (a, b) are

$$a = -\frac{3V_g^2 R}{2(X^2 + R^2)}, \qquad b = -\frac{3V_g^2 X}{2(X^2 + R^2)}, \tag{3.5}$$

and whose radius (r) is

$$r = \frac{3V_g E_m}{2\sqrt{X^2 + R^2}}. \tag{3.6}$$

In a weak grid, X and R are approximately equal or with relatively small differences [50]. Hence, the PQ circle for a VSG connected to a weak grid is similar to the blue circle shown in Fig. 3.3, *i.e.,* such that $a < 0$ and $b < 0$ with $a \approx b$. The consequence of this is that P and Q are typically strongly coupled around the operating point of the VSG: controlled changes to $P > 0$ result into uncontrolled changes to Q.

In contrast, the connection of a conventional SG to a strong, highly inductive grid results in P and Q being largely decoupled. Let $Z_s(X_s, R_s)$ denote the impedance between the SG and the strong grid. The conventional SG operates with a value of α

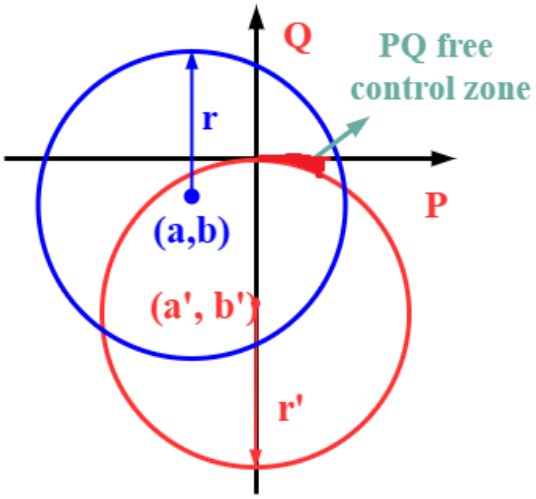

Figure 3.3: *PQ power circles for a SG connected to a strong grid (red circle) and a VSG connected to the weak grid (blue circle)*

close to $90°$, such that

$$P = \frac{3V_g E_m}{2X_s} \sin\delta, \tag{3.7}$$

$$Q = \frac{3V_g}{2X_s} \left(E_m \cos\delta - V_g\right), \tag{3.8}$$

which may be combined to give the PQ circle

$$(P)^2 + \left(Q + \frac{3V_g^2}{2X_s}\right)^2 = \left(\frac{3V_g E_m}{2X_s}\right)^2. \tag{3.9}$$

The coordinates of the centre of this circle are

$$a' = 0, \qquad b' = -\frac{3V_g^2}{2X_s}, \tag{3.10}$$

while the radius is

$$r' = \frac{3V_g E_m}{2X_s}. \tag{3.11}$$

This circle is indicated in red on Fig. 3.3. There exists a small portion of the circle—the red shaded region labelled the PQ *free control zone*—where P and Q are nearly decoupled: a $P > 0$ can be provided by varying δ while Q remains near to zero or, more precisely, within a tolerable range. At the same time, a desired non-zero value of Q can be transferred to the grid at near-constant P by making variations to the internal voltage amplitude E_m. Hence, in this region of operation, a decoupled PQ control can

be achieved.

3.3 Virtual power circles based PQ decoupling technique for a VSG connected to the weak power grid

Before presenting the proposed PQ decoupling technique for the VSG connected to a weak grid, subsection 3.3.1 provides a critical literature review of the existing PQ decoupling techniques.

3.3.1 Challenges of the existing PQ decoupling techniques

Various approaches have been proposed in the literature to solve the PQ–coupling problem, as surveyed in sequel. In [51] a novel linearization–based PQ control scheme is proposed to reduce oscillations caused by the PQ coupling. The method requires a parametric value (m)—the tangent of the PQ circle—which is difficult to compute and estimate. The scheme in [52] feeds forward reference values for P and Q, determined from a small signal model of the VSG; despite the simplicity of obtaining the controller gains, determination of the required increments to power angle and internal voltage of the VSG can be complex to determine in practice. In [128] a virtual impedance is designed based on the capacitor current feedback for suppression of the harmonics, while quantification of the required magnitude of the virtual impedance is done on the basis of the modulation signal. The relationship between coupling of the PQ and the virtual impedance is, however, not investigated. In [53] the idea of using a virtual negative resistance to achieve PQ decoupling, proposed in [54], is enhanced to mimic a proportional-resonant controller in its implementation. Practical applicability may be limited, however, by the observation that the use of proportional integral (PI) controller in the voltage control loop may lead to critical stability of the DC components of the output currents; moreover, the VSG structure was not considered in the design of the controller of the inverter. In [55] a novel non-PLL based method for PQ control with Hilbert transform is proposed. The method does not, however, incorporate the VSG structure in the inverter control design. In [56, 57] a modified PLL is proposed: P and Q

are decoupled based on the axial voltages, achieved by the addition of a series virtual inductance. However, quantification of the magnitude of the virtual inductance is needed and its effect to the system is not investigated. Moreover, inertia is not emulated in the inverter's control design.

Virtual impedance has been used in the VSG designs for limiting the fault current, improving power sharing and for suppressing harmonic oscillations. In [60] a large virtual impedance is designed to limit the symmetrical three phase fault currents in the microgrid. Motivated by this research work, [61] improved the output impedance of the synchronverter by adding a large virtual inductance in series with the stator inductance. The added inductance is intended to increase stability of the synchronverter by preventing the occurrence of undesired large current variations in the event of the grid voltage variations. The use of large impedance, however, increases the voltage drop which can hinder the power transfer; moreover, in [61] the synchronverter is connected to a strong grid and hence the PQ coupling is not studied. In [129] a finite control set model predictive control based VSG is designed for an islanded microgrid, wherein a virtual impedance is used to shape the output impedance of the converter for the accurate power sharing. In this work, however, the quantification of the required magnitude of the virtual impedance is not provided. In [52, 58, 59] the virtual impedance is quantified based on the harmonic analysis to improve the harmonic oscillations of the current. A virtual impedance with fractional proportional integral derivative (PID) controller is used to achieve accurate reactive power sharing in [130], while in [131] adaptive virtual impedance is used in a microgrid to achieve the same goal. In the latter literature's, analysis is limited to the case of an islanded microgrid. Moreover, quantification of the virtual impedance is limited to a particular application, whether harmonic analysis or reactive power sharing. This results in complexity in sizing of the values of virtual impedance.

From the detailed literature survey above, it can be observed that the PQ coupling problem still needs some research. This is in particular for VSG technologies connected to a weak grid. The use of virtual impedance shows promise solution, however, quantification of its required magnitude is still challenging. *Therefore, this chapter bridges this gap with the control objective of achieving a decoupled PQ control using virtual impedance for a VSG connected to a weak grid. This should be achieved in a fashion that*

P is controlled by modulation of the δ and Q by internal voltage modulation. Moreover, there should be simplicity in establishing type and magnitudes of the required virtual impedance. To achieve this objective, a simple new PQ decoupling technique for a VSG connected to a weak grid is introduced. The working principle and implementation of this technique is as discussed in the following subsections.

3.3.2 The virtual power circles based PQ decoupling technique for a VSG connected in a weak power grid

Working principle of the proposed PQ decoupling technique

The aim is to achieve a decoupled PQ control for the synchronverter connected to a weak grid, and to achieve this in such a way that P and Q may be controlled using conventional methods; that is, direct power angle (δ) control for P and internal voltage amplitude (E_m) modulation for Q. To achieve this aim, the PQ power circle of the VSG connected to the weak grid will be shifted to a location corresponding to that of an SG connected to a strong grid, as indicated in Fig. 3.3. To this end, the first step is to translate the centre of the PQ power circle from (a, b) to (a', b'). This requires the P-coordinate of the power circle to be moved from $a \neq 0$ to $a' = 0$. From (3.5), $a = 0$ if and only if $R = 0$ since $V_g > 0$ is enforced by the grid. To achieve this, therefore, we propose to add a virtual resistance $R_v = -R$ in series with the original impedance $Z(X, R)$. The subsequent total equivalent interfacing resistance seen by the system, $R_T = R_v + R$, will then be equal to zero.

This shifts the P-coordinate of the power circle's centre to $a = a' = 0$ but also modifies the radius r to

$$r = \frac{3V_g E_m}{2\sqrt{X^2 + R_T^2}} = \frac{3V_g E_m}{2\sqrt{X^2}}. \tag{3.12}$$

Hence, in order to maintain the radius at its original value, a virtual inductive impedance X_{Lv} is added. Thus, the total equivalent interfacing impedance is

$$Z_T(X_T, R_T) = \underbrace{(R + R_v)}_{R_T=0} + \jmath \underbrace{(X + X_{Lv})}_{X_T} \tag{3.13}$$

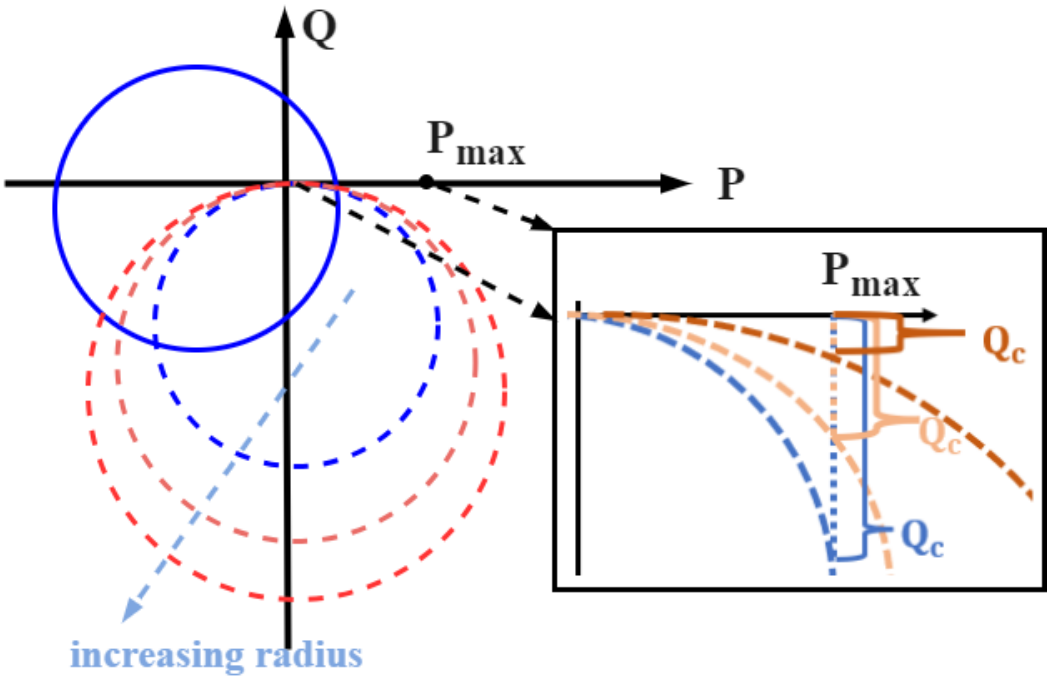

Figure 3.4: *Conceptual visualisation of how the PQ cycles can be shifted for a decoupled PQ control of the VSG connected a weak grid*

yielding the radius

$$r = \frac{3V_g E_m}{2\sqrt{X_T^2 + R_T^2}} = \frac{3V_g E_m}{2(X + X_{L_v})}, \tag{3.14}$$

and Q-coordinate of the circle's centre

$$b = -\frac{3V_g^2}{2(X + X_{L_v})}.$$

Note that this circle passes through the point $(0, 0)$ if $E_m = V_g$. Moreover, if

$$X_{L_v} = \sqrt{X^2 + R^2} - X. \tag{3.15}$$

then

$$r = \frac{3V_g E_m}{2\sqrt{X^2 + R^2}} \quad \text{and} \quad b = \frac{3V_g^2}{2\sqrt{X^2 + R^2}}, \tag{3.16}$$

and the circle has the original radius of (3.6); moreover,

$$r = \frac{E_m}{V_g} b \quad \text{and} \quad r - b = \frac{3V_g}{2\sqrt{X^2 + R^2}} \left(E_m - V_g\right). \tag{3.17}$$

The net effect of the addition of the series impedance $Z_v(X_{Lv}, R_v)$ is therefore to

translate the PQ power circle of the weak grid-connected synchronverter to resemble that of an equal-sized SG connected to a strong grid.

An analysis of the PQ coupling

This translation does not necessarily achieve adequate decoupling of P and Q, since the PQ free control zone is limited in extent if the power circle radius is small. This is illustrated in Fig. 3.4, where the solid blue circle is the original one of the weak grid-connected synchronverter and the dashed blue circle is the resulting PQ following the addition of $Z_v(X_{Lv}, R_v)$. We present an analysis of this coupling in this section, leading to conditions on the circle radius that must be satisfied to achieve adequate decoupling.

Suppose that it is desired to supply $(P, Q) = (P_{\text{ref}}, Q_{\text{ref}})$. Following the translation describe in the previous section, the P and Q supplied are, in terms of the circle radius r and Q-centre b,

$$P = r \sin \delta \tag{3.18}$$

$$Q = r \cos \delta - b. \tag{3.19}$$

Three facts are apparent from these relations:

1. $P = P_{\text{ref}}$ is possible only if $r \geq P_{\text{ref}}$; the value of δ required to provide $P = P_{\text{ref}}$ is then
$$\delta_{\text{ref}} = \sin^{-1} \frac{P_{\text{ref}}}{r} \in [-\pi/2, +\pi/2]\,. \tag{3.20}$$

2. $Q = Q_{\text{ref}}$ with $P = 0$ can be achieved by setting
$$r - b = \frac{3V_g}{2\sqrt{X^2 + R^2}} (E_m - V_g) = Q_{\text{ref}}. \tag{3.21}$$

3. If $r - b = Q_{\text{ref}}$ to provide $Q = Q_{\text{ref}}$, then setting $\delta = \delta_{\text{ref}}$ in order to achieve $P = P_{\text{ref}}$ results in
$$Q = Q_{\text{ref}} - Q_c(r) \tag{3.22}$$
where
$$Q_c(r) := r(1 - \cos \delta_{\text{ref}}) = r \left(1 - \sqrt{1 - \left(\frac{P_{\text{ref}}}{r} \right)^2} \right) \tag{3.23}$$

This means that supplying $P = P_{\text{ref}}$ via control of δ is accompanied by a coupled reactive power Q_c that perturbs from the reference value Q_{ref} (including when $Q_{\text{ref}} = 0$); this coupled perturbation $Q_c(r)$ is, for $r \geq P_{\text{ref}}$, a monotonically decreasing function of r such that:

1. $Q_c(r) = P_{\text{ref}}$ when $r = P_{\text{ref}}$;
2. $Q_c(r) \to 0$ as $r \to \infty$;
3. $Q_c(r_2) < Q_c(r_1)$ for $r_2 > r_1$.

To reduce this coupling the radius of the power circle must therefore be increased. It is shown in Fig. 3.4 that as the radius of the circle increases the magnitude of Q_c decreases and, thus, the extent of the PQ free control zone increases. It is also evident that there exists a circle for which $P = P_{\text{ref}}$ is possible while $|Q_{\text{c}}| \leq \varepsilon$, for any positive constant ε; in particular, solving (3.23) with the condition $|Q_{\text{c}}| \leq \varepsilon$ yields

$$r \geq \frac{P_{\text{ref}}^2 + \varepsilon^2}{2\varepsilon}. \tag{3.24}$$

The problem of providing $P = P_{\text{ref}}$ and $Q = Q_{\text{ref}} - Q_c$ with $|Q_c| \leq \varepsilon$ is then (theoretically) just a matter of selecting a sufficiently large radius of the circle; however, setting $X_{Lv} = \sqrt{X^2 + R^2} - X$ as described in the previous section provides no guarantee that (3.24) is met.

Modifications to achieve adequate decoupling

It can be observed from (3.14) that to increase the radius requires the reactance $X + X_{Lv}$ to decrease, since E_m is reserved for Q control while V_g is the grid voltage. To achieve this a capacitor with reactance X_v is added in series with the original interfacing inductance X. The new interfacing reactance is

$$X_T' = X + X_{Lv} + X_v \tag{3.25}$$

where—if $X_{Lv} = \sqrt{X^2 + R^2} - X$, as previously explained—X_v may be sized such that

$$X_T' = \gamma\sqrt{X^2 + R^2} \tag{3.26}$$

with $0 < \gamma \leq 1$ because the value of X_v is negative.

This results in the radius

$$r(\gamma, E_m) = \frac{r_0(E_m)}{\gamma} \quad \text{where} \quad r_0(E_m) \coloneqq \frac{3V_g E_m}{2\sqrt{X^2+R^2}}, \tag{3.27}$$

where we now explicitly notate that r is a function of γ and E_m. This replaces condition (3.24) with

$$\frac{r_0(E_m)}{\gamma} \geq \frac{P_{\text{ref}}^2+\varepsilon^2}{2\varepsilon} \iff \gamma \leq \frac{2\varepsilon}{P_{\text{ref}}^2+\varepsilon^2}\frac{3V_g E_m}{2\sqrt{X^2+R^2}}. \tag{3.28}$$

Likewise, the corresponding centre coordinates are $a = 0$ and

$$b(\gamma) = \frac{b_0}{\gamma} \quad \text{where} \quad b_0 \coloneqq -\frac{3V_g^2}{2\sqrt{X^2+R^2}}. \tag{3.29}$$

This replaces condition (3.21) with

$$\frac{3V_g}{2\gamma\sqrt{X^2+R^2}}\left(E_m - V_g\right) = Q_{\text{ref}}. \tag{3.30}$$

Now it is seen that problem of providing $P = P_{\text{ref}}$ and $Q = Q_{\text{ref}} - Q_c$ with $|Q_c| \leq \varepsilon$ is a matter of setting the virtual reactance and finding a suitable pair (E_m, γ) such that (3.28) and (3.30) are met. Motivated by this, we define the following algorithm for selecting the virtual circuit parameters.

Algorithm 1 (PQ Decoupling Scheme) *Given $P_{\text{ref}}, Q_{\text{ref}}, V_g, R, X$ and ε*

1. *Obtain γ by solving the optimization problem*

$$\max_{\gamma, E_m} \left\{\gamma : (3.28), (3.30), E_m^{\min} \leq E_m \leq E_m^{\max}, \gamma \leq 1\right\}. \tag{3.31}$$

2. *Set the virtual resistance $R_v = -R$ and virtual reactance $X_{Lv} + X_v$ as*

$$X_{Lv} = \sqrt{X^2+R^2} - X \tag{3.32}$$

$$X_v = (\gamma - 1)\sqrt{X^2+R^2}. \tag{3.33}$$

Algorithm 1 selects the virtual circuit parameters such that the power circle passes

through the points $(P, Q) = (0, Q_{\text{ref}})$ and $(P, Q) = (\pm P_{\text{ref}}, Q_{\text{ref}} - Q_c)$, with $|Q_c| \leq \varepsilon$, for some $E_m \in \left[E_m^{\text{min}}, E_m^{\text{max}}\right]$. The maximum voltage is nominal voltage rating plus its 10%. The maximal γ is taken to maintain the interfacing impedance as large possible while satisfying the developed conditions on power supply and PQ decoupling; a smaller γ implies the need for a larger capacitance in series with the interfacing impedance, and a small system impedance may lead to large transient current values during faults.

In summary, the proposed PQ decoupling technique for a VSG connected to a weak grid is based on the virtual shifting of the center coordinates of the PQ power circle and its corresponding radius modulation. This is achieved by using a virtual RCL circuit which is connected in series with the interfacing impedance between the VSG and the grid. The parameters of the interfacing impedance is obtained from the interfacing filter design and the short circuit characteristic of the grid at the point of common coupling (PCC). Therefore, looking from V to the E, a small impedance will be seen. On top of achieving a decoupled PQ control for the VSG, the reduction of impedance has advantage of increasing a power angle stability. This is due to the increase in the synchronising power. From this point onwards, the technique shall be referred to as *virtual power circles based PQ decoupling scheme*.

3.4 Implementation of the virtual power circles based PQ decoupling scheme for a VSG connected to the weak grid

To implement the proposed scheme, a conventional synchronverter is designed and then modifications are performed on it to accommodate the proposed scheme. Figure 3.5 provides the general hardware structure of the conventional synchronverter connected to the grid. It is composed of the voltage source inverter (VSI), the LCL filter, the circuit breaker (CB)–part of the point of common coupling (PCC)–and the grid.

The following subsections provide modelling of the synchronverter, sizing of the parameters of the LCL filter and the modifications that are performed on the synchronverter for the implementation of virtual power circles based PQ decoupling scheme.

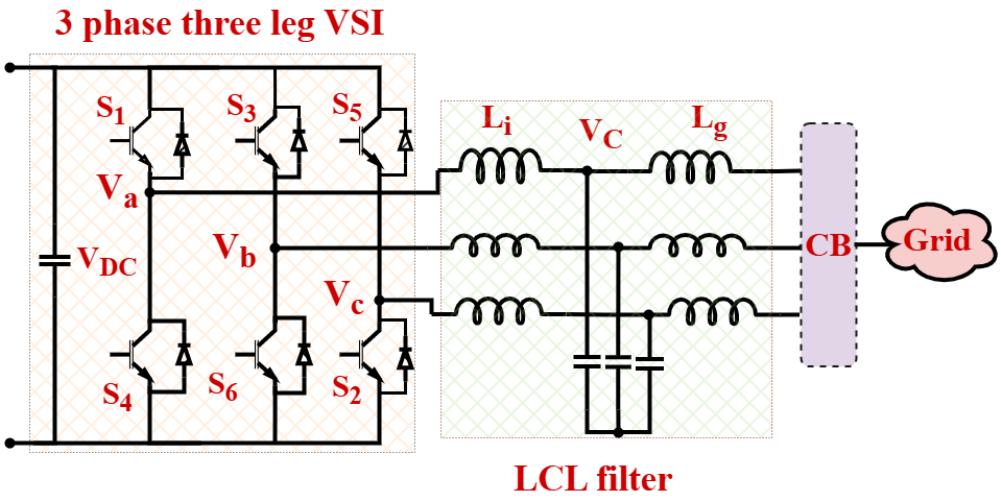

Figure 3.5: *A general hardware configuration of the synchronverter*

3.4.1 Modelling of the conventional synchronverter

A synchronverter is an inverter that mimics the operation of the SG. A SG is an electro-mechanical machine which converts mechanical energy to the electrical energy. There are different types and shapes of SGs. In this work, the synchronverter is modeled to mimic a standard synchronous generator (SG) configuration, specifically a round rotor, non-salient pole machine, as outlined in [39]. The model assumes the absence of damper windings, magnetic saturation, and eddy current losses, with a single pair of magnetic poles. These simplifications align the synchronverter's behavior with that of a conventional SG for easier analysis. The system under consideration connects a single synchronverter to a distribution network with a line-to-line voltage of 415 V, incorporating a ±10% tolerance to account for standard operational variations. To ensure stability, the rotor angle is constrained to a maximum of 90° to prevent instability, consistent with the stability limits of synchronous machines.

The synchronverter's current capacity is derived from its rated power, ensuring that it operates within safe thermal limits under nominal conditions. Additionally, stability considerations include maintaining synchronization with the grid under varying load conditions, emulating the inertia and damping characteristics of traditional SGs. These parameters, including voltage, current, and stability constraints, are crucial for reliable operation and ensure compatibility with the existing power system infrastructure. Furthermore, being an electro-mechanical equipment, there are electrical and mechanical dynamics in the machine. Electrically, the machine is composed of the internal voltage

(E), armature resistance (R_s) and inductance (L_s) and terminal voltage (V_t). In Fig. 3.5, V_t is same as V_c. The internal voltage is controlled by controlling the excitation of the machine and is given by

$$E = L_s \frac{dI}{dt} + IR_s + V_t \tag{3.34}$$

where I is the supplied current by the synchronverter. For a three phase system $I = [I_a, I_b, I_c], E = [E_a, E_b, E_c]$ and $V_t = [V_{ta}, V_{tb}, V_{tc}]$. If θ is the angle of the grid voltage and δ is the power angle for a particular supplied P, then internal voltages are [132]

$$\begin{cases} E_a = E_m \sin(\theta + \delta), \\ E_a = E_m \sin(\theta - (\frac{2\pi}{3}) + \delta), \\ E_a = E_m \sin(\theta - (\frac{4\pi}{3}) + \delta), \end{cases} \tag{3.35}$$

where the amplitude $E_m = K_T \omega_v$ such that K_T is an excitation constant which is obtained from the voltage control loop and ω_v is the virtual angular velocity of the synchronverter. The latter is governed by the swing equation

$$J_v \frac{d(\omega_v)}{dt} = \frac{P_{mec}}{\omega} - \frac{P}{\omega} - D(\omega_v - \omega), \tag{3.36}$$

where J_v is the virtual inertia constant, ω is the nominal grid frequency, P_{mec} is the mechanical input power, and P is the power supplied to the grid:

$$P = E_m I_a \sin(\theta + \delta) + E_m I_b \sin\left(\theta - \tfrac{2\pi}{3} + \delta\right) + E_m I_c \sin\left(\theta - \tfrac{4\pi}{3} + \delta\right), \tag{3.37}$$

with corresponding reactive power

$$Q = -E_m I_a \cos(\theta + \delta) - E_m I_b \cos\left(\theta - \tfrac{2\pi}{3} + \delta\right) - E_m I_c \cos\left(\theta - \tfrac{4\pi}{3} + \delta\right). \tag{3.38}$$

While Fig. 3.5 represents the power part of the synchronverter–the hardware configuration, Fig. 3.6 represents the electronic part–the controller of the synchronverter. This involves virtual inertia emulation using swing equation, calculations of active and reactive powers, calculations of require internal voltage and modulating signals.

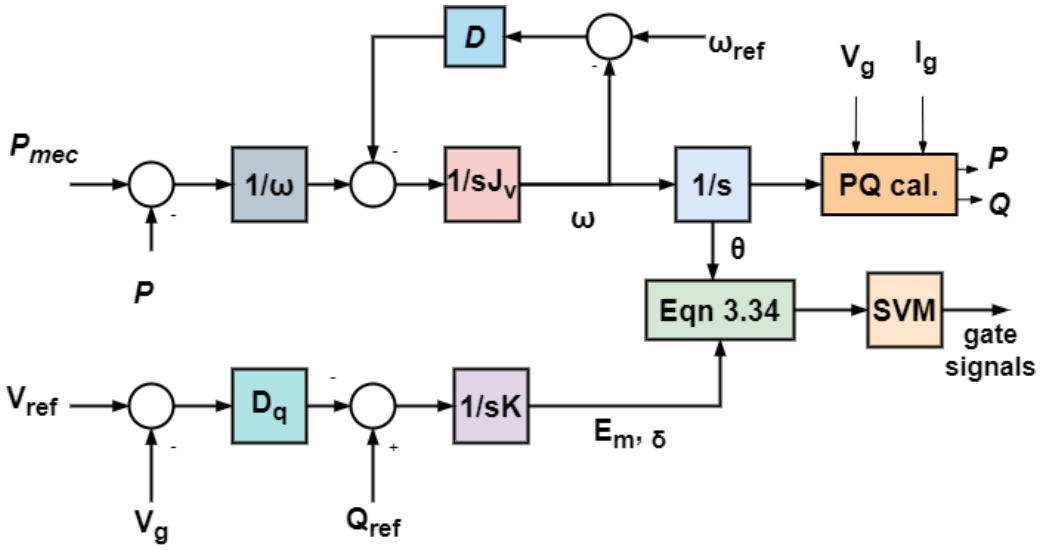

Figure 3.6: *Electronic part of the synchronverter*

3.4.2 Virtual stator design–The LCL filter

The output voltage of the VSI contains harmonics which hinders its direct synchronisation with the grid, so as to avoid supplying highly harmonic current. These currents distort voltage profile and put high reactive power requirement from the power system operator (PSO). Therefore, a low pass filter is required to make sure that the harmonics are trapped and hence clean voltage and currents are obtained. According to IEEE 1547 [133], the supplied current into the grid must have harmonic content less than 5%. Thus, a low pass filter is required to ensure harmonic contents are met. There are many low pass filter topologies, however LCL filters have been proved to offer optimal solution in terms of the harmonics attenuation as well as on the basis of the cost and size [134]. Hence, an LCL filter is designed for interfacing the VSI with the grid.

In the current context, the LCL filter forms the stator of the synchronverter, and thus its sizing is of great importance. To achieve accurate sizing the algorithms proposed in [135–138] are combined with some modifications, accounting for the following considerations.

- The power transfer between two synchronized sources is limited by the size of the interfacing impedance between them. If P_r is the rating of the synchronverter, the maximum impedance between the grid and synchronverter is

$$|Z|_{\max} = \frac{3V_g E_m^{\max}}{2P_r}. \tag{3.39}$$

The total interfacing impedance, once the LCL filter is added, must therefore not exceed this value.

- The resonant frequency of the LCL filter is

$$f_{res} = \frac{1}{2\pi}\sqrt{\frac{L_i + L_g}{C_f L_i L_g}}, \tag{3.40}$$

where f_{res} is the resonant frequency, L_i is the inverter side inductance, L_g is the grid side inductance and C_f is the filter capacitance. This frequency must be within the specified range

$$10f_0 \leq f_{res} \leq 0.5f_s, \tag{3.41}$$

where f_0 is the power frequency and f_s is the switching frequency, since resonance below this range adversely affects power frequency operations, while resonance higher than this range affects system sampling and switching of the VSI.

Therefore (3.39) and (3.41) forms two general conditions that must be adhered to while sizing the filter for the grid connected VSI.

Sizing of the inverter side inductor (L_i)

The size of the inverter side inductance is determined on the basis of the allowed current ripple of the supplied current to the grid. Considering three phase-three leg VSI [136,138], the supplied current ripple is

$$\Delta I = \frac{2V_{DC}}{L_i} m(1-m)T_s, \tag{3.42}$$

where V_{DC} is the DC link voltage of the VSI, m is the modulation index, T_s is the switching cycle period and ΔI is the ripple in the current supplied. The maximum supplied current ripple, attained with $m = 0.5$, is

$$\Delta I_{max} = \frac{V_{DC}}{6L_i f_s}. \tag{3.43}$$

However, the relation between maximum current I_{max}, rated phase voltage V_p, and rated power P_r is

$$I_{\text{max}} = \frac{\sqrt{2}P_r}{3V_p} \tag{3.44}$$

Therefore, if the allowed maximum current ripple is $\Delta I_{\text{max}} = \kappa I_{\text{max}}$, then

$$L_i = \frac{V_{\text{DC}}V_p}{2\sqrt{2}\kappa f_s P_r} \tag{3.45}$$

is the required inverter side inductance.

Sizing of the grid side inductor (L_g)

The size of L_g is related to L_i by a parametric value r:

$$L_i = rL_g. \tag{3.46}$$

According to [135] the maximum harmonic attenuation is obtained when $r = 1$ and thus, the values of L_i and L_g should be equal.

Sizing of the LCL-filter capacitor (C_f)

The size of the capacitor affects the power factor and voltage profile of the synchronverter. Moreover, its value is also affected by the value of L_i and they are inversely related. That is, if there is a large L_i, a small capacitance is sufficient to ensure higher harmonics attenuation. In [136, 137, 139], C_f was sized based on the limitation of the power factor to 5%. Hence

$$C_f = 0.05C_b, \tag{3.47}$$

where

$$C_b = \frac{1}{2\pi f_0 |Z|_{\text{max}}}. \tag{3.48}$$

Consider a grid connected system given in Fig. 3.11; If the system is composed of a $5kW$ synchronverter operated using space vector modulation with sampling time of $40\ \mu s$ and a DC link voltage of 700 V. This results to L_i of $5\ mF$ and hence a C_f of $130\ \mu F$. Using these parameters, the system was initialized and synchronized to the grid at around 0.5 s. It was observed that,no sooner had the circuit breaker closed the system started supplying reactive power to the grid. This is as shown in Fig. 3.7. This is undesired trait and it is

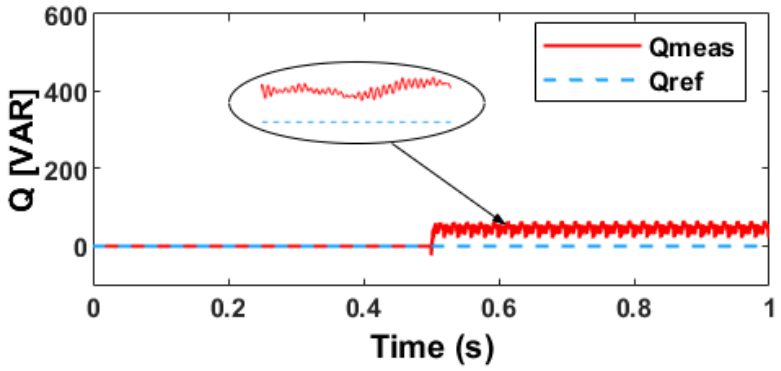

Figure 3.7: *Uncontrolled supply of reactive power during synchronization with C_f given by* (3.47)

attributed to the high value of the capacitance. Hence, since equation 3.48 considers the maximum impedance, a smaller impedance can be chosen. We then considered actual impedance from the designed inductors of the filter, that is, L_i and L_g. Then, equation (3.47) becomes

$$C_f = \frac{0.05}{2\pi f_0 |Z_L|} \tag{3.49}$$

where

$$|Z_L| = 2\pi f_0 (L_i + L_g). \tag{3.50}$$

This results to a C_f of $50\mu F$. When This capacitor is deployed with in the same system, the system was successfully synchronised with no injection of the reactive power as shown below in Fig. 3.8 and in all simulation results as provided in Section 3.6. The ripples from simulations results are inevitable due to the switching action of the inverter.

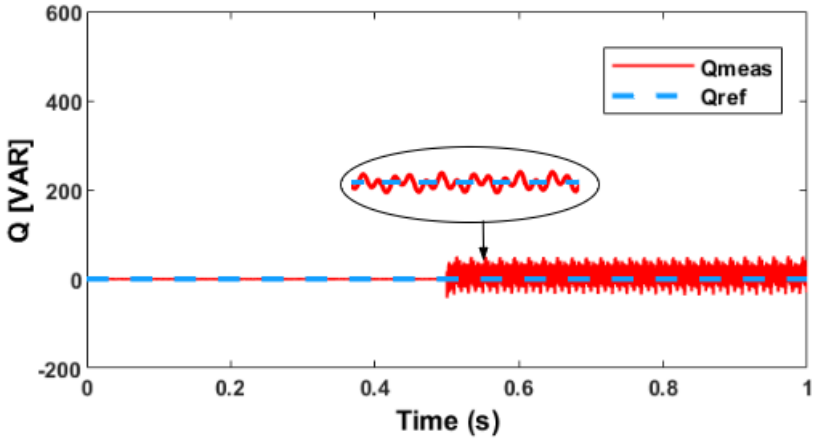

Figure 3.8: *Reactive power during synchronisation with C_f given by* (3.49)

3.5 Modifications to the conventional synchronverter

Implementation of the proposed scheme requires addition of the RCL–PQ decoupling circuit. Hence, the conventional synchronverter is then modified to include the RCL–PQ decoupling circuit as shown in Fig. 3.9; *The illustrates the synchronverter configuration with a virtual RCL decoupling circuit. This representation is not a physical connection in the actual system but rather a conceptual model intended to enhance understanding of the modifications applied to the synchronverter. The virtual RCL circuit serves as an abstraction that emulates the behavior of the decoupling components within the control framework, providing a clear and intuitive visualization of how these modifications influence system dynamics. This approach simplifies the analysis by mapping the control design onto a familiar electrical equivalent, thereby offering insight into the functional enhancements introduced by the virtual RCL configuration*. The RCL–PQ decoupling circuit is implemented virtually in the controller of the synchronverter. The virtual implementation of the RCL–PQ decoupling circuit minimises the cost of implementation and ensures sustainable control; that is, it eliminates the need for re-configuring the hardware part of the synchronverter should the P requirement vary or the grid weaken.

The RCL–PQ decoupling circuit modifies (3.34) to

$$E = \int \frac{I}{C_v}\, dt + (L_v + L_i)\frac{dI}{dt} + I(R_s + R_v) + V_t. \tag{3.51}$$

The magnitude of L_v is computed from X_{Lv}, while that of C_v is evaluated on basis of the value of γ, which, as previously explained, is selected based on the reference power ($P_{\text{ref}}, Q_{\text{ref}}$). To obtain the reference powers, droop controllers are used:

$$P_{\text{ref}} = P_{\text{set}} + D_p(\omega_{ref} - \omega), \tag{3.52}$$

$$Q_{\text{ref}} = Q_{\text{set}} + D_q(V_{\text{ref}} - V_g) \tag{3.53}$$

where D_p is the droop gain for the P–ω control in the system and D_q is the droop gain for the Q–V control. From the reference powers and selected value of γ, C_v is quantified and hence the required magnitude of the virtual impedance. Moreover, the required magnitude of the internal voltage (E_m) and power angle (δ) can be computed from the P

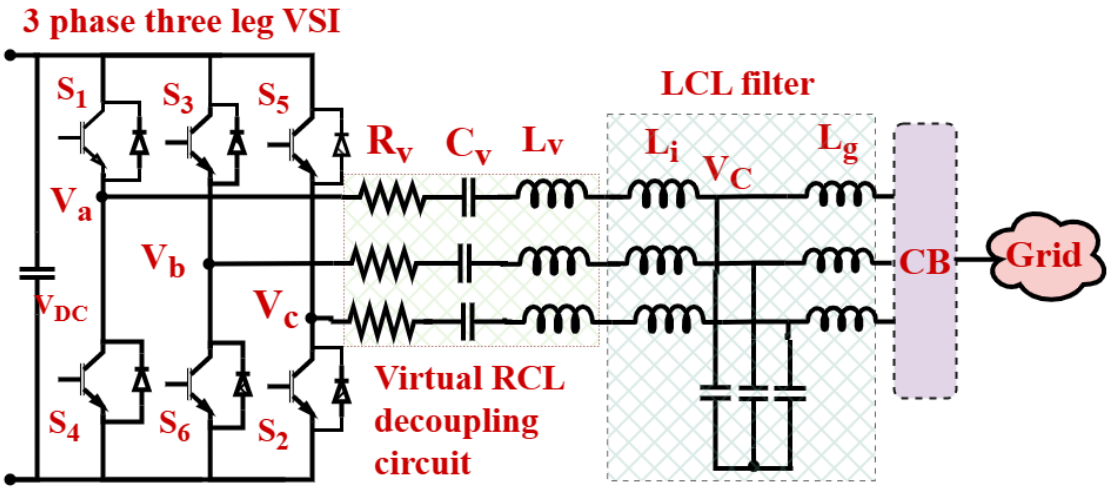

Figure 3.9: *An illustration of the conceptual model of a synchronverter with a virtual RCL decoupling circuit;*

and Q equations using X_T'. The synchronverter controller (SC) is, however, modified where the input to the modulator is virtual power angle (δ_v) and virtual amplitude of the internal voltage (E_{mv}). These values are computed from the impedance model of the grid connected inverter, given in Fig. 3.10. Based on this model, the values of δ_v and E_{mv} can be calculated. Thus, contrary to [40], direct power-angle control of the synchronverter is deployed which offers simplicity in tuning of the parameters due to the removal of the PI controller.

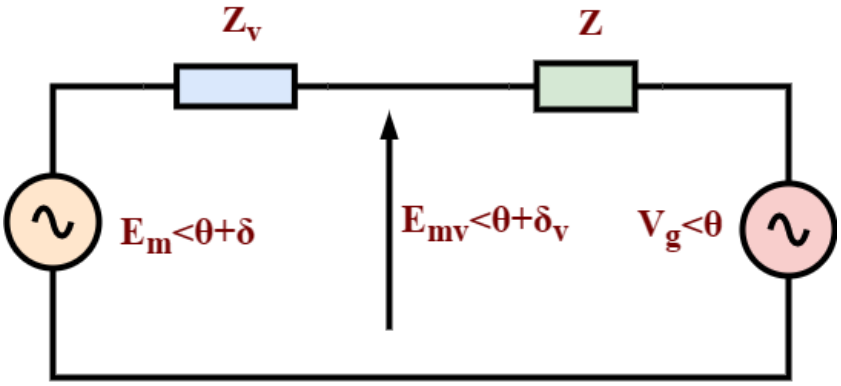

Figure 3.10: *Impedance model of the modified synchronverter*

3.6 Simulations and results analysis

Figure 3.11 provides a per phase representation of the simplified grid connected synchronverter system that was used for simulation studies. The system parameters are as

provided in Table 4.1. The system is implemented in MATLAB/Simulink environment.

Table 3.1: *System parameters.*

Parameter	Value
Rated power (P_r)	5kW
DC bus voltage (V_{DC})	700V
Phase voltage (V_p)	240V
C_f	$50\mu F$
$L_i = L_g$	5mF
X/R ratio	1.05
T_s	40e-6 s
D_p	5000
D_q	50
k	10%

Five cases are demonstrated to test the validity of the proposed PQ decoupling scheme. The first case verifies the PQ coupling that exists when a synchronverter is connected to a weak grid without any decoupling technique. The second case shows that, there exists a partial PQ decoupling when a synchronverter PQ power circle is virtually moved to the location similar to that of the SG connection to the strong grid ($\gamma = 1$). The third case, demonstrates the total PQ decoupling at $\gamma = 0.04$. Then, the fourth and fifth cases are the extensions of the third case, where the synchronverter under the proposed scheme is shown to aid the grid during mild frequency and voltage variations. This is achieved without causing large undesired grid currents. In all the cases, the system is initialised and the circuit breaker is turned ON at 0.5 s to synchronize the inverter to the grid.

3.6.1 Operation on the Physical PQ-power Circle

Figure 3.12 provides simulation results under this case. Referring to Figure 3.4, this case is similar to trying to control P and Q independently on the solid blue circle. Thus, no virtual impedance is used and hence, there is no quantification of γ. A system is initialised and synchronised to the grid at around 0.5 s. Then, while Q is kept constant, a step change in P is demanded at 1 s. It is observed that the measured P follows the reference value (P_{set}), but Q also changes, undesirably deviating away from its set point. Hence there exists a strong coupling between P and Q and therefore, a decoupling

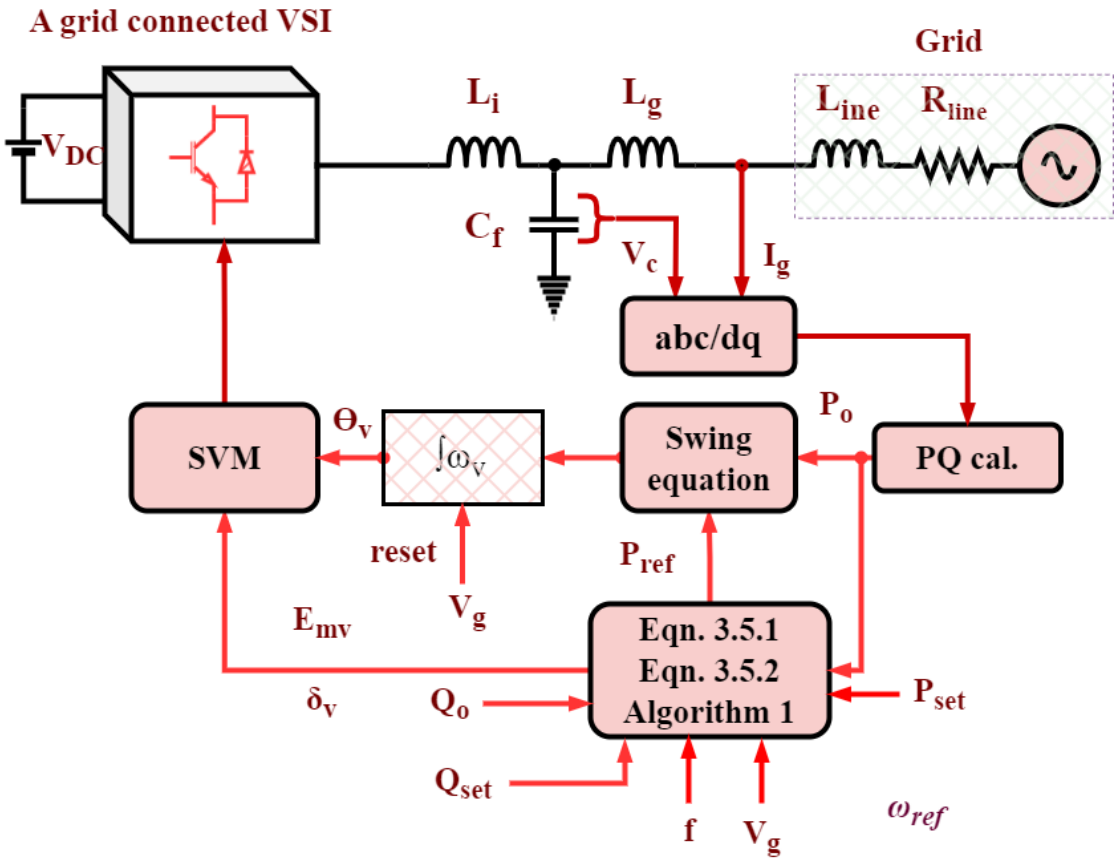

Figure 3.11: *A considered grid connected VSG system for simulation studies*

technique is required to achieve independent P and Q control.

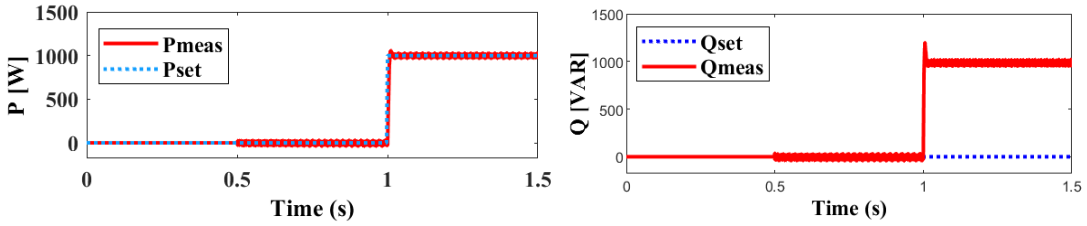

(a) *Coupled active power* (b) *Coupled reactive power*

Figure 3.12: *Simulation results: a coupled PQ control*

3.6.2 Operation on the shifted virtual PQ-power circle ($\gamma = 1$)

This is similar to controlling P and Q, on the dotted blue circle of Fig. 3.4. Hence, the radius of the actual PQ power circle and shifted virtual PQ-power circle are the same. Thus, the total impedance ($Z_T(X_T)$) of the shifted virtual PQ power circle is equal to the original interfacing impedance ($Z(X, R)$) between the synchronverter and the grid. The proposed scheme is tested under three step changes of P, that is from 0 to 1000 W, then to 4000 W and finally to 500 W at 1 s, 1.5 s and 2 s respectively. It is shown in Fig. 3.13a that the measured P follows the P-reference at all times but the measured Q deviates when P exceeds 1000 W. Therefore, there is partial PQ decoupling when $\gamma = 1$.

It is also observed that the impact of adding virtual decoupling impedance is on the voltage applied to the inverter. It is seen from Fig. 3.13c that the required RMS voltage changes to $244.2V$, $256.5V$ and to $242.1V$ at the respective times corresponding to the step change in P. Therefore, the addition of negative resistance increases the voltage demand from the inverter. Hence, the values of the virtual impedance must be carefully designed so that the increase in voltage by virtual impedance must not cause the applied voltage to exceed the specified standard voltage bounds. Moreover, the DC link must be designed to ensure that it is capable of supporting the required increase in voltage.

3.6.3 A total decoupled PQ control ($\gamma = 0.04$)

This case describes total PQ decoupling by the proposed scheme which is achieved at $\gamma = 0.04$. A system is initialised and synchronised to the grid at around 0.5 s. The ability

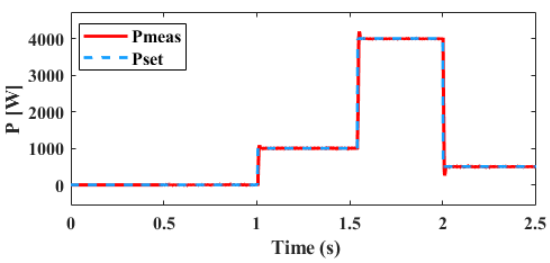

(a) *Active power response*

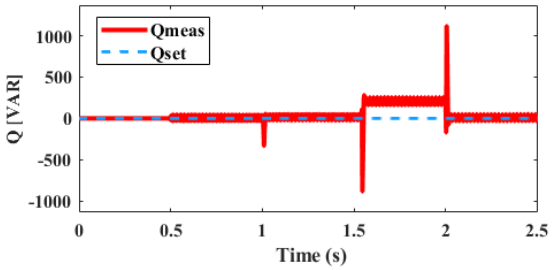

(b) *Reactive power response*

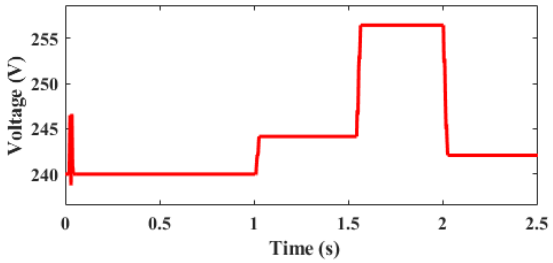

(c) *Applied inverter voltage (E_{mv})*

Figure 3.13: *Simulation results: partial PQ decoupling ($\gamma = 1$)*

to decouple P and Q, and achieve their independent control is as shown on Fig. 3.14a and Fig 3.14b.

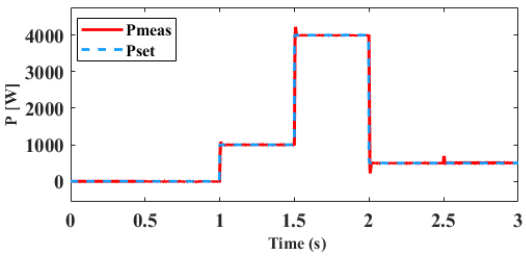

(a) *Active power response*

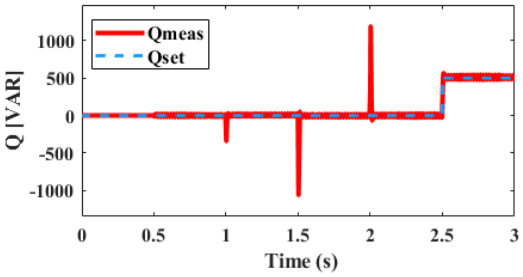

(b) *Reactive power response*

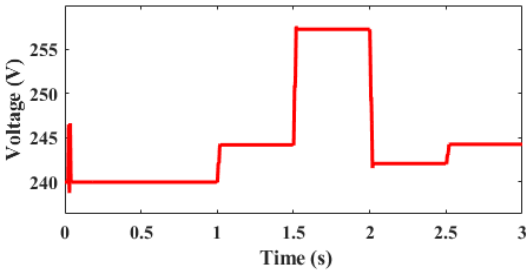

(c) *Applied inverter voltage (E_{mv})*

Figure 3.14: *Simulation results: total PQ decoupling ($\gamma = 0.04$)*

A step change of P is invoked from 0 to $1000\,\mathrm{W}$ at $t = 1\,\mathrm{s}$, followed by changes to $4000\,\mathrm{W}$ and $500\,\mathrm{W}$ at times $t = 1.5\,\mathrm{s}$ and $t = 2\,\mathrm{s}$ respectively. Both the measured P and

Q follow their references successfully during these times. A step change in Q is then introduced from 0 to $500\,\mathrm{var}$ at time $t = 2.5\,\mathrm{s}$; this is done to demonstrate that both P and Q can change independently. The measured Q follows its reference successfully while P still tracks its reference.

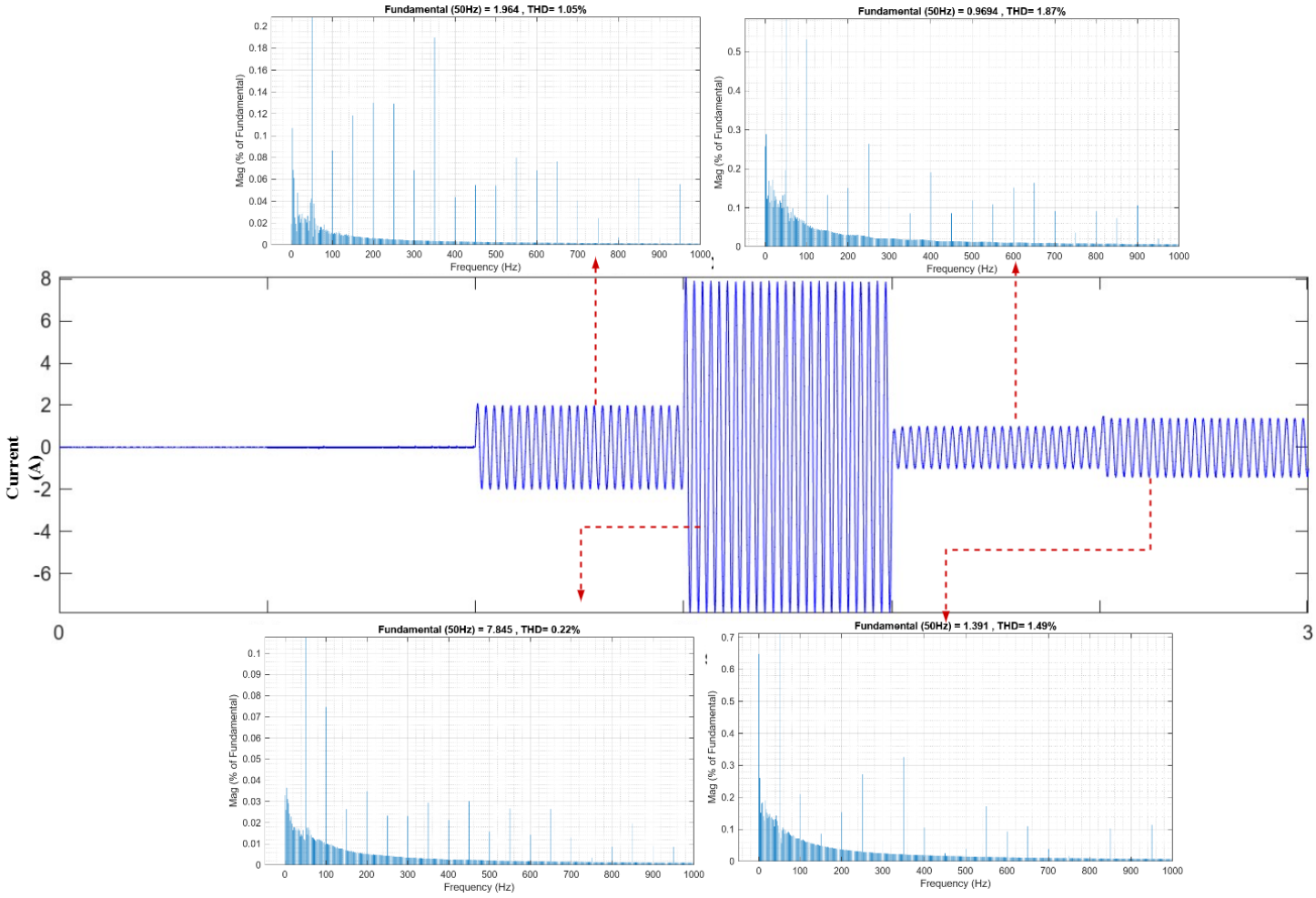

Figure 3.15: *A THD analysis for the grid injected current*

In both Fig. 3.14a and Fig 3.14b, transients occur in the P and Q variables when the other variable changes. These are due to the decoupling action and last for less than one quarter of the power frequency cycle; hence, they would not be expected to interfere with the normal sychronverter operations. Since addition of the RCL decoupling circuit put demand on the required inverter voltage, it is worth analysing the magnitude of voltages required when changes of both P and Q are invoked. In Fig. 3.14c it is shown that the voltage required is within 10% of the nominal voltage, which is a standard for many distribution voltages. The maximum RMS voltage change from the nominal value is $+7.1\%$ (from $240\,\mathrm{V}$ to $257\,\mathrm{V}$).

Finally, THD analysis was performed for each current section during P and Q variations. According to IEEE 1547 standard [133], the THD of the injected current by the grid-connected inverter must be below 5%. It is shown in Fig. 3.15 that the THD for each current section is below this specified value: the typical values of THS are 1.05%, 0.22% and 1.87% for the different P values (with $Q = 0$) of 1000 W, 4000 W and 500 W respectively; on the other hand, the THD was 1.49% when P was set to 500 W and Q to 500 var.

3.6.4 Response under grid frequency variations

This fourth case aims to analyse the response of the modified synchronverter when there are frequency variations in the weak grid. A totally decoupled synchronverter ($\gamma = 0.04$) is used. Similar to the previous cases, the synchronverter is initialized and synchronized to the grid at around $t = 0.5$ s. A step change in P, from 0 to 1000 W, is commanded at $t = 1$ s, followed by a step change in Q, from 0 to 200 var, at $t = 1.5$ s. This is important to invoke normal operation of the synchronverter at its limits before the insertion of frequency variations.

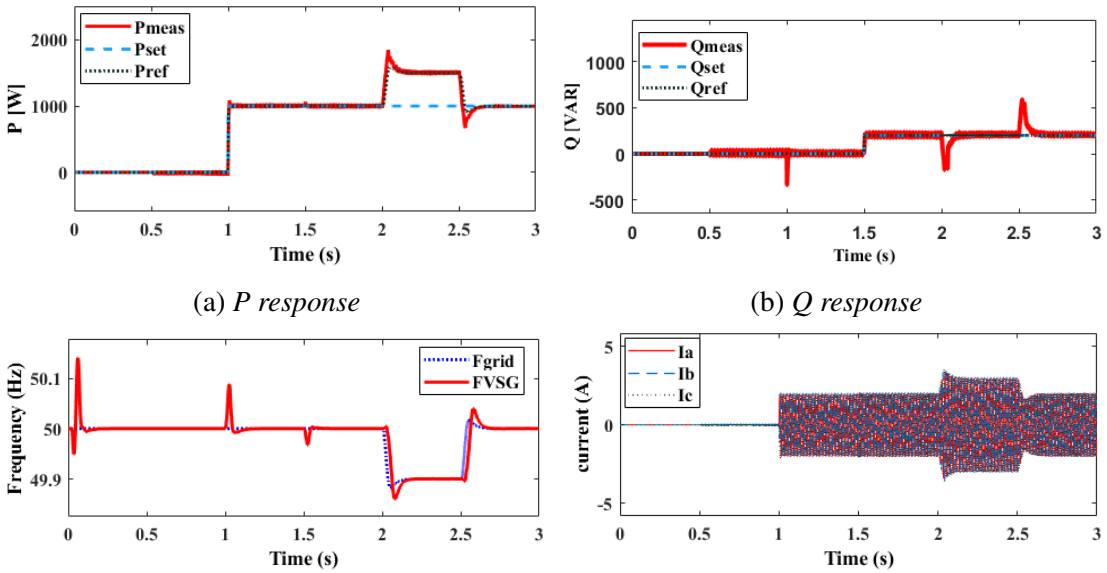

(a) *P response*

(b) *Q response*

(c) *Synchronverter's-grid frequency response*

(d) Supplied grid current

Figure 3.16: *Simulation results under 0.2% grid frequency drop*

It can be observed from Fig. 3.16a and Fig. 3.16b that, prior to the imposed frequency drop, $P_{\text{set}} = P_{\text{ref}}$ and $Q_{\text{set}} = Q_{\text{ref}}$. That is, there is no droop action and, hence, the grid

frequency and voltage are at their desired nominal values. At $t = 2\,\mathrm{s}$, a grid frequency drop of 0.2% is simulated. The grid recovers after 25 power frequency cycles, as shown in Fig. 3.16c. During this time, the synchronverter remains synchronized with the grid without producing large grid currents (Fig. 3.16d). Similarly, the synchronverter continues to supply power while helping the grid to recover to its nominal grid frequency. This is achieved by increasing the P supplied such that the $P_{\text{ref}} > P_{\text{set}}$ (Fig. 3.16a); the size of increase in P_{ref} depends on the value of the droop coefficient D_p. After the grid frequency recovery, the synchronverter adjusts the supplied additional P, which was for frequency recovery, to its setpoint such that $P_{\text{set}} = P_{\text{ref}}$ again. The measured Q follows its reference value albeit for some transients during P changes due to the decoupling actions. The synchronverter manages to track grid frequency without losing synchronism (Fig. 3.16c).

3.6.5 Response under grid voltage variations

The final case aims to validate the ability of the modified synchronverter to aid the grid recovering to its nominal voltage in the event of mild grid voltage variations. Similar to Sec. 3.6.4, a decoupled synchronverter ($\gamma = 0.04$) is initialized and synchronized to the grid at around $0.5\,\mathrm{s}$, and the same P and Q changes are invoked at the same times seen in the previous case. A voltage sag of 90% is simulated at $t = 2\,\mathrm{s}$, from which the grid recovers to its nominal RMS voltage after 25 power frequency cycles (Fig. 3.17d). In Fig. 3.17a) we see that the P supply is maintained at all times, with $P_{\text{set}} = P_{\text{ref}}$ because of the absence of frequency deviation.

Fig. 3.17b provides the Q response under this scenario. After the insertion of the grid voltage variation at $t = 2\,\mathrm{s}$, the generated Q is increased by the droop controller, necessary to aid the voltage recovery in the grid. This increase is maintained until the grid voltage recovers to its nominal value at around $t = 2.5\,\mathrm{s}$. During the voltage step change, there is an surge of grid current (Fig. 3.17e). The magnitude of this transient current, however, is less than 2 per units of the nominal rating grid current, as can be observed in zoomed in phase A current in Fig. 3.17e; therefore, the transient current is within the typical safe operating region of the semiconductor devices.

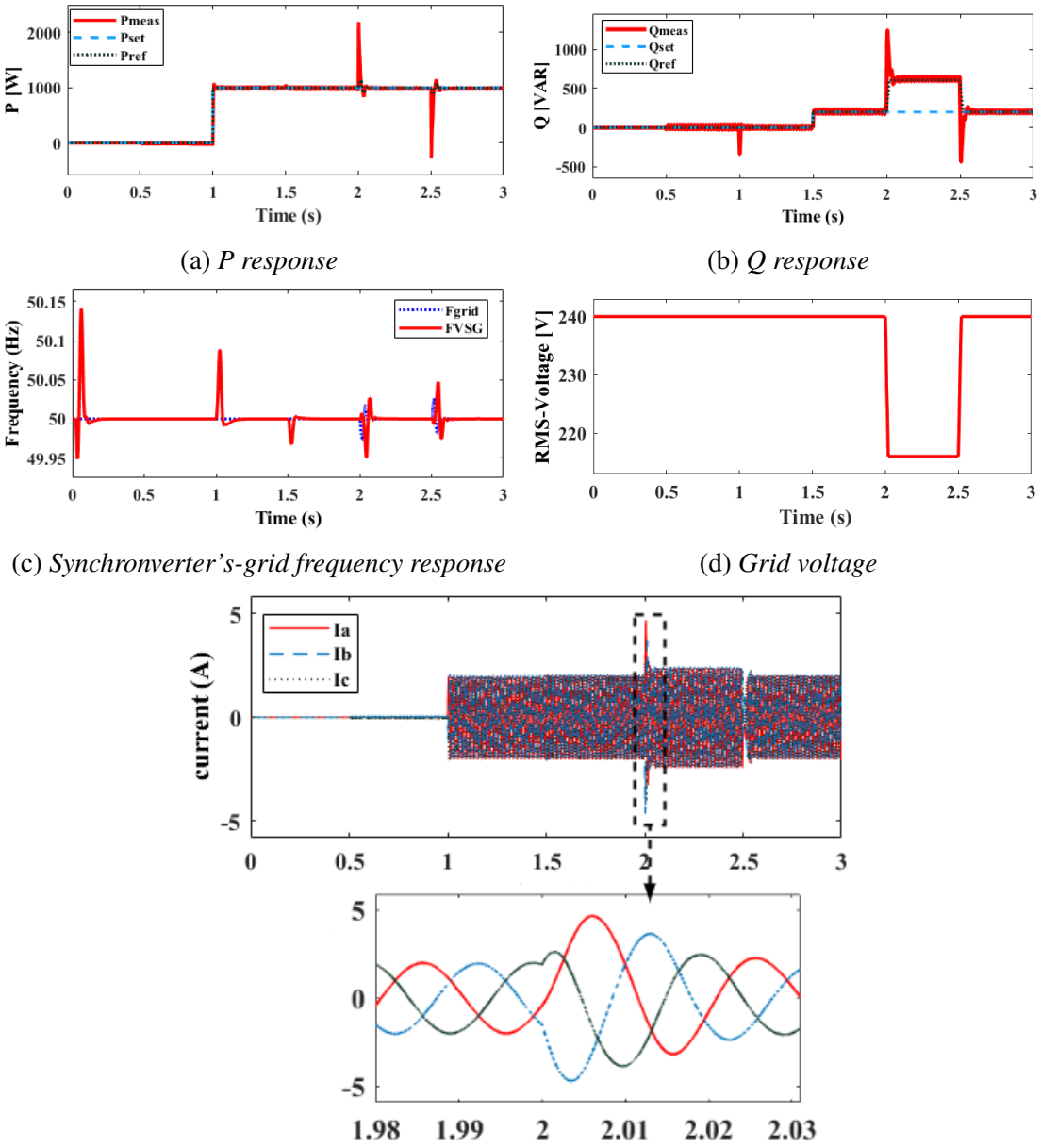

(a) *P response*

(b) *Q response*

(c) *Synchronverter's-grid frequency response*

(d) *Grid voltage*

(e) *Supplied grid current*

Figure 3.17: *Simulation results under a voltage sag of 90%*

3.7 Summary

In this chapter a novel PQ decoupling scheme, which operates on the basis of shifting of the center and radius modulation of the PQ power circle, was presented. The technique was demonstrated to provide a decoupled PQ control for a VSG connected to the weak grid. The implementation of the scheme requires modification of the virtual stator of the VSG by incorporating a RCL–PQ decoupling circuit. Hence, a conventional synchronverter as a representative of the VSG technologies was designed. The choice

for this particular VSG topology is based on the study by Tamrakar [47], which asserts that this topology provides best results in limiting RoCoF and frequency deviations on occurrence of the frequency contingency. Modifications were then performed on it for accommodating the proposed scheme. This was followed by the validation of the ability of proposed scheme to achieve a decouple PQ control for the synchronverter connected to a weak grid. Moreover, since the PSO requires the VSG to aid the grid in recovering from frequency and voltage deviations, to their nominal values. It was then demonstrated that, the synchronverter under the proposed scheme can support the grid during frequency contingencies by increasing its P supply. Furthermore, it was also demonstrated that the modified synchronverter can support the grid to recover to its nominal voltage during mild voltage sags. In case of the medium and severe voltage sags, however, large transient currents might be observed. These can destroy the VSG—power electronic semiconductor devices. Hence, the inclusion of a low voltage fault ride-through (LVRT) capability is essential for the VSG in the proposed scheme. This requirement stems from the increasingly rigorous standards set by power system operators (PSOs), necessitating VSGs to possess LVRT capabilities. Consequently, this prerequisite applies not only to VSGs operating within the proposed scheme but also to those utilizing any other PQ decoupling technique. The LVRT feature in grid-connected VSGs plays a crucial role in maintaining power system stability and preventing cascading failures. Chapter 4 is therefore dedicated to provide in detail discussion on LVRT for the VSGs.

Chapter 4

A novel Low Voltage Fault Ride Through (LVRT) for the VSG connected to the weak grid

A VSG is required to aid the grid to recovery to its nominal state when faults such as voltage sags occur in the grid. To achieve this, a VSG must have a LVRT capability. In this chapter a novel LVRT strategy using an active superconducting fault current limiter (SFCL) is presented. The designed active SFCL is operated using a finite control set model predictive control (FCS-MPC). In order to ride through low voltages (i.e. voltage sags), the active SFCL must be controlled in coordination with the virtual power circles based PQ decoupling scheme. Therefore, the presented LVRT strategy is designed based on this requirement. Simulations results are provided to test the validity of the presented LVRT strategy. It is demonstrated that, the VSG with the FCS-MPC based active SFCL can ride through voltage sags while supplying the required power as per grid codes. It is also shown that–with this strategy the maximum power harvest from RES-generators can be achieved during voltage sags with an improved transient response.

4.1 Introduction

Existence of voltage sags is inevitable, particularly in a system with high penetration of RES-generators, since they may be caused by a variety of commonplace events, including short circuit faults, sudden injection of large loads—such as large-motor starting—and overloads. Moreover, voltage sags may be experienced widely throughout the system—a node may experience voltage sag caused by a geographically distant fault—thus are a global problem caused by a local interruption. A voltage sag, by definition, is a

short duration reduction of the RMS voltage [140]. This may induce undesirably high currents in connected VSG units, risking potential damage to semiconductor devices and equipment owing to overheating; this is exacerbated by a low impedance between the VSG and grid. Limiting this current at the same time that the voltage is suppressed, however, limits the power transfer, potentially resulting in under-extraction of power from RE sources.

As mitigation to these risks, IEEE Std 1547-2018 explicitly requires distributed energy resources (DER), including Virtual Synchronous Generators (VSGs), to remain connected and support grid stability during disturbances, such as voltage sags, rather than disconnecting [141]. This prevents sudden cessation of operations, which could lead to power imbalances, high RoCoF, and relay triggering, especially in grids with high renewable energy penetration. Similarly, the European Network Code "Requirements for Generators" (RfG) [142] stipulates that power-generating modules, including RES and VSGs, must have low voltage ride-through (LVRT) capability. Article 21(3)(e) of the RfG specifically requires generators to remain connected during voltage sags and provide reactive power support to aid grid recovery.

Additionally, Germany's VDE-AR-N 4120 [143] and Australia's National Electricity Rules (NER) [144] further reinforce these requirements, mandating that all generators provide reactive power support and frequency stabilization during grid disturbances. These provisions highlight the global trend in grid code modifications to ensure grid-connected VSGs and RES actively contribute to system stability. Figure 4.1 illustrates a typical set of PQ requirements for a VSG during LVRT. These requirements are revised from the data provided in [62, 69, 145–148]. Essentially, the amount of Q and/or P that are required to be supplied by the RES-generator during fault is defined by the *bilateral agreement* between PSO and the RES-generator owner, or depending on the designed specifications if the RES-generator is owned by the PSO.

In chapter 3 an RCL–PQ decoupling circuit is introduced in the grid connected VSG system. The introduction of the series capacitor lowers the total equivalent interfacing impedance between the VSG and the grid, such that on observing from the grid to the VSG a small interfacing impedance is seen. This can result in a lage current flow during fault conditions such as on the occurrence of the voltage sags, which in turn can damage the VSG power semiconductor switches. The challenge is, therefore, to develop a control

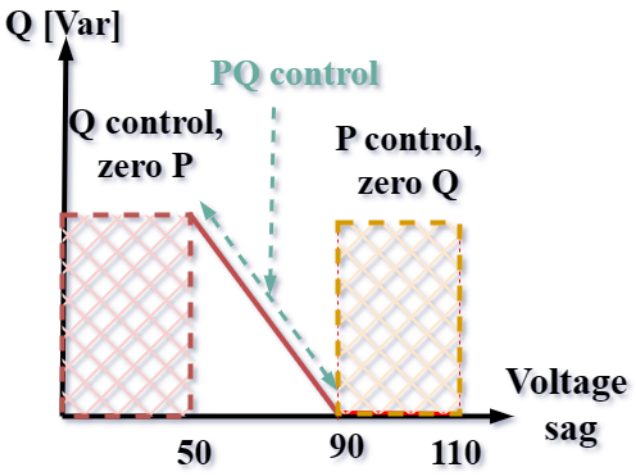

Figure 4.1: *A PQ-voltage sag variation requirement for a grid-connected RE generator. During normal grid conditions, or mild voltage sags, a VSG is required to supply, or continue to supply, P at unit power factor (zero Q). On the other hand, a VSG is required to change its control mode from P control to PQ control, or to Q control, when voltage sags are between 50 and 90%, or 0 and 50%, respectively.*

strategy for VSGs that satisfies LVRT requirements. Moreover, the strategy must offer a satisfactory transient response when transitioning through different PQ requirements. This chapter, therefore, presents a solution to this challenge by providing a novel LVRT strategy using a FCS-MPC based active SFCL. The strategy operates a FCS-MPC based active SFCL by its coordination with the virtual power circles based PQ decoupling scheme. It will be demonstrated that, the presented LVRT strategy can limit fault currents while adhering to the grid codes. This is achieved with a limited transient response of the supplied current.

The rest of the chapter is organised as follows: A critical literature review on the state of the art LVRT strategies is presented in section 4.2, while the effect of the symmetrical voltage sag to the operating PQ power circle is presented in section 4.4. This lays foundation for the development of the proposed LVRT strategy using an active SFC which is presented in section 4.5. The latter section starts by clarifying the need of an active SFCL LVRT strategy in operating a VSG with a low front end impedance, and then introduces the proposed design of an active SFCL which is operated using FCS-MPC. The mathematical analysis–during normal and abnormal grid conditions is presented in this section, as well as, how the grid codes can be adhered to at different voltage sags. Then, implementation of the proposed strategy is presented. Section 4.6 follows by providing simulation results to support the presented technique. The chapter is then

finalised in section 4.7 by providing its summary.

4.2 A critical literature review on the existing LVRT techniques

To this point, it can be concluded that the requirement for the LVRT is indispensable for the VSG connected to the power system with high penetration of RES. The state of art for LVRT methods can be categorised mainly in two groups: *software (controllers) based LVRT techniques* and *hardware based LVRT techniques*.

The software based LVRT techniques are the methods that involve limitation of the fault current while supplying the required power without introducing any component to the system. This means, these techniques provide LVRT by modification of the controller's operation on occurrence of the voltage sags. Some of these methods are detailed in [62–66, 148–151] . A simple PI current control based LVRT controller is developed for the single phase grid connected inverter in [63]. The technique involves injection of the active reactive current proportional to the magnitude of the voltage sag to provide dynamic reactive power support during faults. Similarly, in [149] a proportional–resonant (PR) current controller with harmonic compensator is designed for the inverter in a single phase transformerless solar photovoltaic system (SPV) to achieve a LVRT. The technique involve limiting the current during faults to its maximum peak current. The analysis in [63, 149] are limited to a strong grid and only balanced faults were considered. Moreover, the controller designs did not incorporate the VSG structure which limits their applicability in the low inertia power system.

A fuzzy logic current controller based on instantaneous power theory is developed to improve the LVRT of the SPV–system as per Malaysian grid codes in [65]. The results presented shows that during fault the reactive power is maintained at zero value which makes the approach insufficient in fulfilling the current–modified grid codes. In [148] injection of active current to provide dynamic voltage support is analysed. The method requires momentary raising of the rating of the inverter which creates a potential risk of occurrence of the thermal runaway to the semiconductor devices. Moreover, in both [65, 148] the control algorithm did not consider inertia emulation in its design.

A direct power angle control and voltage amplitude modulation based LVRT tech-

nique is proposed for a single phase VSG connected to a strong grid in [150]. The method requires a PLL for tracking the grid angle which results in a slow transient response. Moreover, the research did not investigate the ability of the VSG to supply reactive power during fault conditions which–thus–does not comply with the current–modified grid codes. A similar approach (to [150]) is used in [151]. This literature, however, considers a three phase inverter connected to a strong grid. To limit over current during faults the active power is controlled proportional to the squares of the grid voltage while reactive power is still maintained at zero. Hence, the approach fails to aid the grid in recovering to its nominal voltage during faults.

To comply with the modified grid codes, in particular [146], and assisting the grid to recover to its nominal voltage during faults an auxiliary voltage controller is proposed in [62]. The design is implemented using a universal controller such that during faults active power is curtailed while reactive power is increased. The response of the controller, however, took 10 cycles to curtail active power and 20 cycles to reach to the desired value of the reactive power. This response is insufficiently fast for the low inertia power system, in particular when a low impedance grid connected system. This is because of the large current that might flows during that period.

In [66] A LVRT is achieved on basis of transitioning, switching between voltage control mode to current control mode. This limits the magnitude of fault current and supplies reactive power during faults. The method, however, is prone to creating large transient currents during transitioning between the two modes. This is caused by the complexity in synchronising between the two modes. Moreover, the method is prone to power oscillations during the ride through. Furthermore, the switching between the two modes might add another two unnecessary transient events on top of the fault and fault recovery transient events. These might be extreme, in particular, for the VSG operating with a low grid interfacing impedance. To improve the latter concept (in [66]), an additional current control loop is added to control excitation of the VSG and hence suppressing the unbalanced currents during fault in [64]. The design, however, ignores the coupling that exists between P and Q and hence, makes the design unsuitable for the case of the very weak grid which is characterised by the PQ coupling effects.

Generally, the use of the software based solutions to provide LVRT are limited in their slow and poor transient response. This can result in operation of the circuit breaker

in system with the low interfacing impedance, such as a modified synchronverter with an RCL–PQ decoupling circuit. A cascading failure might occur which results in a blackout as the result of unintentional islanding of the VSGs in such phenomenon. *To improve transient response and limiting the fault current, hardware modifications such as inclusion of dynamic resistances or SFCL can be performed*. Dynamic resistances, crowbar circuits and their modifications are predominantly used in the WTG systems. On the other hand, the SFCL can be used in both SPV and WTG systems. Hence, due to this suitability SFCL have drawn significant attention from researchers.

By definition a SFCL refers to as a unit or a component that offers almost zero impedance during normal conditions and the impedance is increased to higher values during abnormal–fault conditions [152, 153]. This unique property provides a great potential for their deployment in the low inertia power systems. There are two types of SFCL, namely; *passive SFCL and active SFCL*. These two are distinguished by the fact that the latter has a potential of increasing system's impedance and adding a voltage during fault conditions, while the former adds impedance only.

The passive SFCL are further categorised into resistive SFCL (rSFCL), inductive SFCL and hybrid SFCL, depending on the type of impedance that is used to limit the fault current. In [154] the impact of rSFCL on voltage sags is investigated in a Korean distribution system. It was revealed that rSFCL can improve magnitudes of the voltage sag. A comparative analysis between rSFCL and inductive SFCL is done in [155]. The analysis revealed that, the rSFCL pose a great challenge in operation of the power system due to its dissipative nature such that it adds losses and complicates cooling system of the SFCL. On the other hand, inductive type SFCL shows poor transient performance. Thus, the authors recommended the use of hybrid SFCL. This recommendation, however, does not solve the performance problems of resistive or inductive component of the SFCL, but just aims to minimise their effects.

A power grid contains multiple points where SFCL might be installed. Therefore to improve transient performance of the system, the SFCL must be properly allocated and their coordination operation is required. In [156] the analogy to the insulation coordination is proposed for coordination of multiple SFCL in the power grid. In [157] optimal allocation of SCFL equipped with Superconducting Magnetic Energy Storage (SMES) is studied using particle swarm optimisation. The aim is to limit the fault current,

improving voltage drop, reducing energy loss, power deviations and evaluating optimal capacity of SMES in a meshed microgrid with SPV and WTG.

The researches in [154–157] focus on the limiting the fault current and the improvement of the voltage profile only. The studies were thus not intended to explore the LVRT and complying with the current–modified grid codes. Moreover, the analysis did not involve a system with a VSG. Hence, analysis on the impact of SFCL on reactive and active power control of the VSG is missing. Therefore, further research is required considering the use of SFCL in the grid connected VSG. To bridge this gap, a modified flux coupling rSCFL is designed for LVRT of the VSG under severe faults in [70]. It is demonstrated that the methodology can limit the transient current up to 1.3 times the rated current during faults. The method, however, is limited to severe faults and adds losses due to the use of rSFCL type. Moreover, the ability of the VSG to provide PQ control during LVRT was not investigated. The authors having identified this need, *calling for further research to investigate relationship between physical values of SFCL and the virtual impedance for PQ control during LVRT.*

The use of the active SFCL, on the other hand, is investigated in [67–69]. The original idea of the active type SFCL is presented in [67]. The presented SFCL is composed of the superconducting transformer (SCT), a PWM converter and a superconducting magnet. During normal conditions zero impedance is presented through flux compensation on the secondary side of the SCT which is achieved by regulating its current. On the other hand during fault conditions, a variable limiting impedance is presented depending on the current regulation. A similar approach is presented in [68] where an active type SFCL is used to limit fault current and suppress over-voltages in a distribution system, in particular when there is a phase to ground fault with an isolated neutral. In [69] a coordination of the active type SFCL and SMES to limit the fault current in case of minor fault, and achieving a safe islanding of the microgrid with multiple SPV units is presented.

The studies in [67–69] are limited to islanded systems. Therefore, the ability of the system to ride through fault and supply required active and reactive power is not investigated. Hence, the analysis is limited to the suppression of the current during symmetrical three phase faults (only) rather than providing a LVRT as required by the grid codes. Moreover, the analysis in [67] and [68] were presented for the power systems

with no RES-generators, while [69] considered a grid connected RES-generator that does not emulate any inertia. Furthermore, the design of the SFCL involved the use of the PI based current control approach. The tuning of the PI can be exhausting in particular for the sytem with PQ decoupling schemes. On top of these short comings, the use of the PI-based PWM current controllers have limited dynamic response which makes them insufficient for the low inertia power system.

From the detailed literature survey presented above, it is evident that there is a need for research for the LVRT for a VSG connected to the low inertia power system, particularly when the interfacing impedance between a VSG and the grid is low. Therefore, this research work bridges this gap by introducing a novel LVRT strategy using a FCS-MPC based active SFCL. The strategy controls the active SFCL via its coordination with the virtual impedance (the decoupling scheme). That, this work therefore extends the principles and the design of an active superconductor fault current limiters proposed in [67–69] by considering VSG technology in a low inertia power system, coordination with virtual impedance to provide linkage with the previous chapter, the use of FCS-MPC which simplifies the current control problem and utilization of such technology in provision of the LVRT. It is demonstrated via simulation results that, the VSG with the FCS-MPC based active SFCL can ride through voltage sags while supplying the required power as per current—modified grid codes. Moreover, it is shown that with the proposed strategy the maximum power harvest from RE-generators can be achieved during voltage sags with a improved transient response.

4.3 Why a superconducting device is required

Superconducting devices, particularly SFCLs, are uniquely suited for LVRT applications due to their ability to offer negligible impedance during normal conditions and rapidly increase impedance during faults. This capability ensures fault current limitation without disrupting normal operations. Additionally, *active* SFCLs can inject voltage to counteract sags, maintaining grid stability and maximizing power extraction from RES. These attributes make SFCLs indispensable in low-inertia systems where transient responses are critical.

Superconducting devices are inherently expensive due to the specialized materials and

technology required for their operation. To mitigate these costs, we propose leveraging existing inverters within the system and integrating flux coupling inductors to create a new active superconducting device. This innovation retains the benefits of superconducting principles while reducing overall system costs. Furthermore, this device can address extreme faults, such as short circuits, enhancing its utility beyond LVRT applications. This work serves as the initial step toward achieving such a system by incorporating an auxiliary inverter. In the future, this auxiliary inverter can be replaced by the existing inbuilt inverters within the system, reducing costs further. Coordination between two VSGs to achieve this functionality is proposed as future work as discussed in 6.

4.4 Symmetrical voltage sag and its effect to the PQ power circle

Figure 4.2 provides the equivalent impedance model of the grid connected VSG operated using virtual power circles based PQ decoupling scheme: R_v, L_v and C_v are the virtual components of the PQ decoupling circuit, L and R are the physical equivalent inductance and resistance between a VSG and the grid, $E(E_m < \delta + \theta)$ is the internal voltage of the VSG and $V(V_g < \theta)$ is the grid voltage.

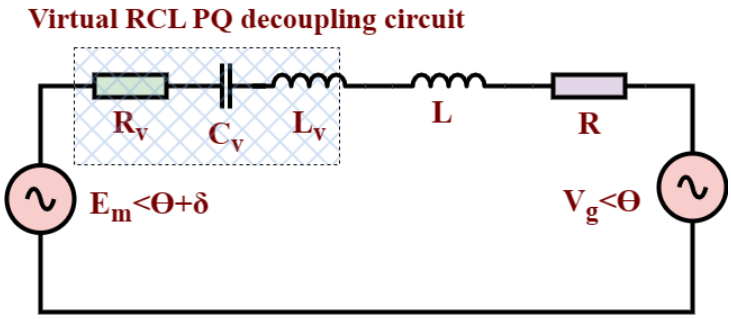

Figure 4.2: *Equivalent model of the grid connected VSG with an RCL PQ-decoupling circuit*

From Fig. 4.2 the current supplied to the grid is given by

$$I_g = \frac{E_m < \delta + \theta - V_g < \theta}{(X_{Lv} + X_{Cv} + X) + (R_v + R)} \tag{4.1}$$

where X_{Lv}, X_{Cv} and X are the reactance of L_v, C_v and L respectively. Since $R_v = -R$, then the magnitude of current I_g becomes

$$I_g = \frac{E_m < \delta + \theta - V_g < \theta}{X'_T} \tag{4.2}$$

where X'_T is the summation of the X_{Lv}, X_{Cv} and X which is quantified using γ [see Chapter 3]. On the occurrence of the voltage sag, high current flows unless it is limited. This is due to small X'_T such that, a small unintentional voltage difference between E_m and V_g is amplified to produce large current. Moreover, the sudden decrease in the grid voltage constrains the power transfer between the VSG and the grid as verified in subsection 4.6. This is due to the collapse of the virtual power circle [ref: (3.9) in chapter 3] to a much smaller (as shown in Fig. 4.3) circle contingent to the level of the voltage sag. Prior to the occurrence of the voltage sag, the system was operating

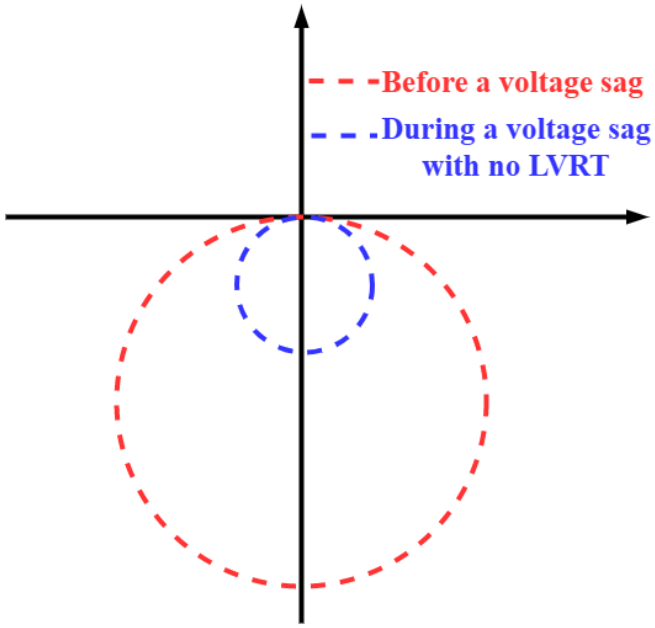

Figure 4.3: *PQ power circles before and during a voltage sag*

on the red PQ power circle. If no LVRT technique is deployed during voltage sag, the center coordinates and hence, the radius decreases as shown in Fig.4.3. This results to the decresease in the PQ free control zone, consequently to a PQ coupling problem and thus, failure of the the VSG to adhere to the grid codes.

4.5 A LVRT strategy using active SFCL for a VSG connected to a weak grid

The SFCLs have potential to be deployed to operate the low impedance based VSGs [152]. Their introduction into the system, however, may constraints power transfer between the VSG and the grid due to the sudden introduction of the impedance and, if care is not taken, this can even results in increasing the coupling between P and Q. Moreover, with the current trend of deployment of the virtual impedance for achieving a decoupled PQ control for the VSG, coordination control between the virtual impedance and the SFCL is required. To achieve this requirement, an active SFCL provides a great potential due to its ability to increase both impedance and voltage to the system.

Therefore, a LVRT technique based on active SFCL is presented in this chapter. The technique achieves a coordinated control between the virtual RCL–PQ decoupling circuit and the active SFCL. That is, the active SFCL is controlled such that it adds zero impedance and zero voltage during normal operation. On the other hand, during fault the active SFCL adds voltage to the system such that, on looking from the VSG to the grid, no voltage sag is detected. By this action, the operation of the VSG is maintained on the circle that was present prior to the occurrence of the voltage sag (the red circle in Fig. 4.3). The designed active SFCL is operated using a FCS-MPC. The benefits of using FCS-MPC and the analysis of the design is provided in subsection 4.5.1.

4.5.1 A FCS MPC based active SFCL design for LVRT of the VSG connected to a weak grid

Model predictive control (MPC) refers to the family of controllers that use model of the plant (system) to predict its future behaviour. Hence, the desired plant performance is achieved by applying the optimal control input that is obtained using a predefined optimisation criterion. That is, by using the model of the system the behaviours of its variables are predicted up to certain time interval (known as the prediction horizon), and then a cost function is formulated to related the behaviour of the predicted variables with their desired/reference performance. Finally, the control inputs that minimises the cost function are selected and applied to the plant [158].

A finite control set (FCS) MPC is based on the fact that there exists a fixed known number of switching states that can be generated by the power electronic converter (PEC). Thus, using the system model-the future behaviour of the variables can be predicted for each of the possible switching states. Then, a cost function can be formulated to select the optimal switching state. That is, among the possible set of the switching states, the one that minimises the cost function is selected as an optimal switching state and is therefore applied to switch the PEC. [159].

The FCS-MPC has gained significant attention to the control of PECs due to its simple structure, flexibility to handle multiple constraints using a single cost function, fast dynamic response which makes it a good candidate for improving transient response and due to its easiness in implementation. Moreover, it removes the need for the modulator and when compared with the sinusoidal pulse width modulation (SPWM) switching technique for PECs, it yields low harmonics in the converter output voltage. In [129, 160, 161] a FCS-MPC is combined with a VSG to improve primary frequency control of an islanded microgrid. A software base FCS-MPC is designed in [162] to improve FRT of the two paralleled operated VSGs.

To contribute to the current trend of deployment of FCS-MPC for PEC control, a FCS-MPC based active SFCL is designed in this research work for providing LVRT of the grid connected VSG. Although we used PI controllers in our conference paper presented at the ISGT Europe conference in 2023 [163], and the results were similar to those obtained using FCS-MPC, the latter technique offers significant advantages due to its simplicity in design by eliminating the complexity of controller tuning. Figure 4.4 provides a per phase circuit diagram of the FCS MPC based active SFCL connected to the VSG circuit operating under a virtual power circles based PQ decoupling scheme.

The active SFCL presented in Fig. 4.4 is constituted by an inverter controlled by the FCS-MPC, filtering inductance (L_f), a flux coupling inductors (L_1 and L_2) with mutual inductance M and parasitic resistance R_2. This configuration allows for precise control of system impedance and voltage injection. By coordinating the SFCL with the virtual power circles-based PQ decoupling scheme, the strategy ensures seamless integration with the VSG system. The model's ability to adapt to varying fault conditions while maintaining system stability and efficiency further justifies its selection. It can be observed, from Fig. 4.4, there are two circuits that are magnetically coupled to each

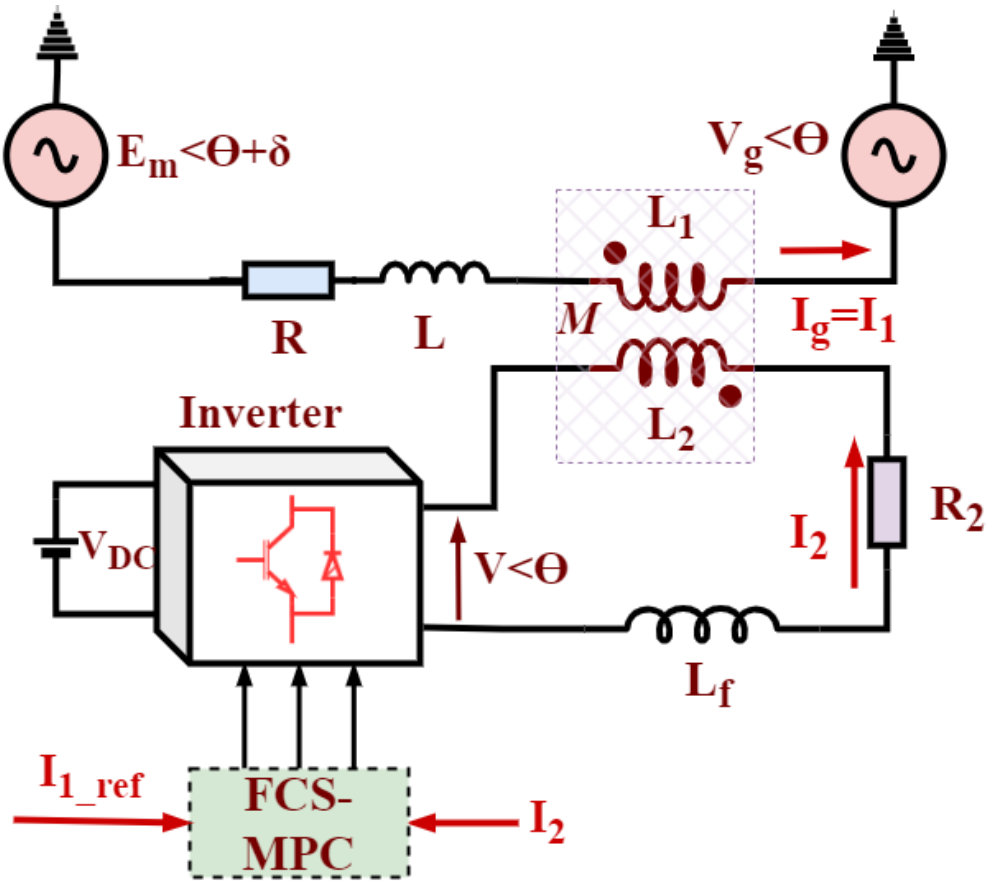

Figure 4.4: *A per phase circuit diagram of a FCS MPC based active SFCL connected to the VSG-grid system operated under virtual power circles based PQ decoupling scheme*

other; the first circuit, which shall be referred to as the main circuit, is composed of the VSG connected to the grid. Comparing this circuit diagram to the Fig. 4.2 there is an introduction of inductance L_1. It will be shown that, this inductance will have zero value during normal conditions. The current flowing in this circuit is I_1. The second circuit is formed by the second inductance L_2 of the coupling inductors. The current flowing in this circuit is I_2. Therefore

$$E_m < \delta + \theta = j(\omega L'_T)I_1 + j(\omega L_1)I_1 - j(\omega M)I_2 + V_g < \theta \tag{4.3}$$

and

$$V < \theta = j(\omega L_f)I_2 - j(\omega M)I_1 + j(\omega L_2)I_2 + I_2 R_2 \tag{4.4}$$

can be derived from Fig. 4.4 while considering the coupling effects between the flux coupling inductors [164]; L'_T is the inductance of X'_T.

Normal condition analysis

The aim is to control the current I_2 such that during normal operations $j(\omega L_1)I_1 - j(\omega M)I_2 + V_g < \theta = V_n < \theta$, where $V_n < \theta$ is the rated nominal grid voltage. Since, during normal operation $V_g < \theta = V_n < \theta$ then

$$j(\omega L_1)I_1 - j(\omega M)I_2 = 0,$$

$$I_2 = \frac{L_1}{M}I_1. \tag{4.5}$$

Therefore, during normal condition (4.3) and (4.4) becomes

$$E_m < \delta + \theta = j(\omega L'_T)I_1 + V_g < \theta \tag{4.6}$$

and

$$V < \theta = j\omega(L_f - \frac{M^2}{L_1} + \omega L_2)I_2 + I_2R_2, \tag{4.7}$$

respectively. It is observed in (4.6) that during normal conditions zero impedance is presented by the active SFCL. Hence, the active SFCL does not interfere with normal operations of the VSG. This is achieved at the expense of the current control in the auxiliary circuit. The reference current for this purpose is provided by (4.5). Equation (4.7) provides the voltage of the auxiliary circuit under this condition. This can be simplified by including the value of M which is given by

$$M = K\sqrt{L_1L_2} \tag{4.8}$$

where K is the coupling coefficient of the coupling inductors L_1 and L_2. Hence, by substituting (4.8) into (4.7)

$$V < \theta = j\omega(L_f - L_2(1 - K^2) + R_2)I_2. \tag{4.9}$$

It is, thus, observed in (4.9) that the inductance presented by the active SFCL in the auxiliary circuit depends on the value of coupling coefficient K. If the inductors (L_1 and L_2) are perfectly coupled (K), the inductance L_2 becomes zero during normal conditions.

Abnormal condition analysis

The abnormal condition in this case refers to deviation of the grid voltage V_g from its nominal rated condition such as on occurrence of the voltage sags. That is, V_g drops from $V_n < \theta$ to a value $V_g' < \theta$ contingent to the level of the voltage sag. Hence, (4.3) becomes

$$E_m < \delta + \theta = j(\omega L_T')I_1 + j(\omega L_1)I_1 - j(\omega M)I_2 + V_g' < \theta \tag{4.10}$$

where $V_g' < \theta = hV_n < \theta$, such that h is the voltage sag index. Therefore, there is a voltage difference between $V_n < \theta$ and $V_g' < \theta$. This can cause the collapse of the PQ power circle and result in high current flow, as well as, constraining the power transfer between a VSG and the grid. To ride through this voltage sag, the voltage difference must be supplied by the active SFCL such that when observing from the VSG to the grid, no voltage difference between normal grid condition and abnormal grid condition can be observed. To achieve this objective, the reference current is modified as follows

$$I_2 = \frac{V_g' < \theta - V_n < \theta}{j(\omega M)} + \frac{L_1}{M} I_1. \tag{4.11}$$

Let us, substitute (4.11) into (4.10) so as to analyse its impact, that is

$$E_m < \delta + \theta = j(\omega L_T')I_1 + V_n < \theta. \tag{4.12}$$

It is shown that (4.12) is same as (4.6). Thus by incorporating (4.11) in the design of the auxiliary controller, the low voltage condition can be masked by addition of series voltage by the active SFCL such that the fault condition is seen as normal condition by the VSG. This is equivalent to the continual operation to the PQ power circle that existed prior to the occurrence of the voltage sag.

Adherence to the grid codes

According to the Fig. 4.1, the modified grid codes require the magnitude of P and Q supplied by the VSG contingent to the magnitude of the voltage sag. That means, the power factor of the supplied current by the VSG changes from unit value (during normal conditions) to zero value during severe voltage sags. To quantify the current required

during each section (the three sections in Fig. 4.1, that is P control, PQ control and Q control) let us consider the equations of the supplied power as follows:

$$P = 3V_g I_p, \tag{4.13}$$

$$Q = 3V_g I_q \tag{4.14}$$

where $I_p = I\cos\phi$ and $I_q = I\sin\phi$ such that ϕ is the power factor angle and I is the amplitude of the supplied current by the VSG. If I_n is the rated nominal current of the VSG, then the current supplied for the three sections will be,

Constant P [$0.9V_n < V_g < 1.1V_n$]

$$I_p = I_n \tag{4.15}$$

where $I_q = 0$, that is the operation at the unity power factor.

PQ control region [$0.5V_n < V_g < 0.9V_n$]

$$I_p = \sqrt{I_n - I_q} \tag{4.16}$$

where I_p is determined from the Q–V droop control. That is, during voltage sag the determined magnitude of Q by droop action is applied into (4.14) to compute the value of I_q. This value is then used in (4.16) to evaluate I_p which is applied to (4.13) to determine the reference P.

Constant Q [$0.5V_n > V_g$]

$$I_q = I_n \tag{4.17}$$

where $I_p = 0$, that is operation at at zero power factor. This means that, during severe voltage sags, current will be limited to its maximum value rated value and only reactive power will be supplied.

Fundamentally, the contemporary modified grid codes determines the magnitude of current I_1 that should flow in the main circuit during LVRT. This current is used in (4.11) to determine the reference current for the auxiliary circuit.

A FCS-MPC based controller design for the auxiliary circuit

The objective of the auxiliary controller is to fast-track the reference current given by Equation (4.11). *This is a current control problem that can be effectively addressed using FCS-MPC due to its robust design capabilities and dynamic performance* [158]. Moreover, FCS-MPC is well-suited for this task due to its simplicity in design and flexibility in handling multiple constraints. These attributes make it an optimal choice for managing transient faults in low-inertia systems. Furthermore, FCS-MPC offers several other advantages that justify its use in this thesis, these include:

- Direct Switching State Optimization: By directly optimizing the switching states of the power electronic converter, FCS-MPC simplifies control structure and avoids the need for modulators.
- Constraint Handling: The ability to incorporate multiple system constraints into a single cost function ensures precise operation under fault conditions.
- Fast Response Time: The quick dynamic response of FCS-MPC is essential for limiting fault currents and maintaining system stability during voltage sags.
- Harmonic Reduction: Compared to traditional techniques like sinusoidal pulse width modulation, FCS-MPC produces lower harmonic distortion in the converter output.

By leveraging these advantages, FCS-MPC enhances the performance of the active SFCL in providing fault ride-through capability in weak grid conditions.

To design a FCS MPC based current controller, the inverter model must be established and its corresponding switching states (a FCS). Moreover, the load model of the auxiliary circuit must be defined for the current prediction within the defined horizon. Finally, the cost function must be established for determination of the optimal switching states to be applied to converter. This is done using a concept of rolling optimization.

The inverter model of the auxiliary circuit

A three phase three leg inverter is used in the auxiliary circuit as shown in Fig. 4.6. It is composed of two switches operating in complimentary mode in each leg. Each

switch has two states ['ON'=1 or 'OFF'=0]. Hence, due to the complimentary mode operation–which is necessary for avoiding the short circuiting of the converter's legs, each leg has two possible states [1 or 0]. This forms a combination of eight possible switching states. If S_x is a switching state of each leg, where $x = [a, b, c]$ that is a phase index, then each possible combination of switching states generates a voltage vector V' relating the three phases. The switch state S_x relates the phase voltage (V_x) with the DC voltage (V_{DC}), that is, $V_x = S_x V_{DC}$. Hence, the voltage vector is given by

$$V' = \frac{2}{3}(V_a + aV_b + a^2V_c) \tag{4.18}$$

where a is the unitary vector ($e^{j\frac{2\pi}{3}}$) representing 120 degrees phase displacement between phases.

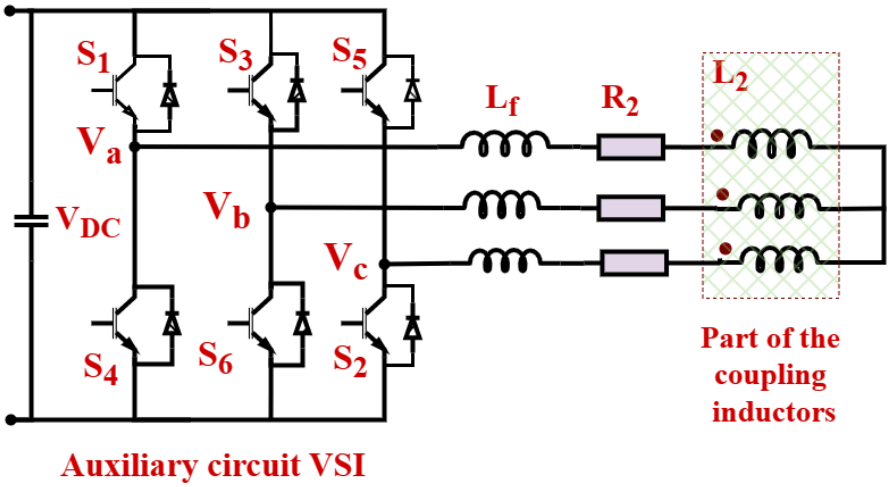

Figure 4.5: *Auxiliary circuit of the active SFCL*

Table 4.1 provides a finite control set of 8 possible switching states with their corresponding output voltage vector V'. Therefore, for every sampling instant these states will be rolled through the cost function. The switching state of the voltage vector V' that minimises the objective function will be applied to the inverter.

The auxiliary circuit current model and its prediction

The current I_2 to be controlled can be found by applying the Kirchhoff's Voltage Law (KVL) around the auxiliary circuit (ref: Fig. 4.4),

Table 4.1: *Switching states of the 3-phase VSI with their corresponding voltage vectors*

S_a	S_b	S_c	Voltage vector V'
0	0	0	$V_0 = 0$
1	0	0	$V_1 = \frac{2}{3}V_{DC}$
1	1	0	$V_2 = (\frac{1}{3} + j\frac{\sqrt{3}}{3})V_{DC}$
0	1	0	$V_3 = (-\frac{1}{3} + j\frac{\sqrt{3}}{3})V_{DC}$
0	1	1	$V_4 = -\frac{2}{3}V_{DC}$
0	0	1	$V_5 = (-\frac{1}{3} - j\frac{\sqrt{3}}{3})V_{DC}$
1	0	1	$V_6 = (\frac{1}{3} - j\frac{\sqrt{3}}{3})V_{DC}$
1	1	1	$V_7 = 0$

$$v = (L_f + L_2)\frac{dI_2}{dt} + I_2R_2 - M\frac{dI_1}{dt} \tag{4.19}$$

where $v = V < \theta$. From (4.11), $\frac{dI_1}{dt}$ is given by

$$\frac{dI_1}{dt} = \frac{M}{L_1}\frac{dI_2}{dt} - \frac{e}{L_1} \tag{4.20}$$

where $e = V_g' < \theta - V_n < \theta$. Hence, after substituting (4.20) and the value of M, (4.19) becomes

$$v = (L_f + L_2(1 - K^2))\frac{dI_2}{dt} + I_2R_2 + K\sqrt{\frac{L_2}{L_1}}e. \tag{4.21}$$

Therefore, (4.21) is used for auxiliary current prediction. That is, by using forward Euler approximation, the derivative term in (4.21) can be approximated as

$$\frac{dI_2}{dt} \approx \frac{I_2(k+1) - I_2(k)}{T_s} \tag{4.22}$$

where T_s is the sampling period, k is the sampling instant. Hence, the one step predicted current is

$$I_2(k+1) = \frac{T_s}{L_f + L_2(1 - K^2)}(v(k) - K\sqrt{\frac{L_2}{L_1}}e(k)) + (1 - \frac{T_sR_2}{L_f + L_2(1 - K^2)})I_2(k) \tag{4.23}$$

where $v(k)$ is the input control voltage which is equal to voltage vector V' in the inverter model, $e(k) = v_g(k) - v_n(k)$: $v_g(k)$ and $v_n(k)$ are the measured grid voltage and the rated nominal grid voltage at every sampling instant, respectively.

Reference current and the cost function

The reference current is obtained from (4.11) which implicitly contains I_1. This current is determined from the impedance model (see: 3.10). Therefore, the impedance model must be redefined to include the fact that the decoupling scheme will always see the nominal rated grid voltage ($V_n < \theta$) instead of the grid voltage ($V_g < \theta$). Hence, I_1 is determined from (4.12) and thus the reference current becomes

$$I_{ref} = \frac{V_g' < \theta - V_n < \theta}{j(\omega M)} + \frac{L_1}{M}\left(\frac{E_m < \delta + \theta - V_n < \theta}{j(\omega L_T)}\right). \tag{4.24}$$

At every sampling instant, (4.24) is equivalent to

$$I_{ref}(k+1) = \frac{e(k)}{j(\omega M)} + \frac{L_1}{M}\frac{e_1(k)}{j(\omega L_T)}, \tag{4.25}$$

where $e_1(k) = e_i(k) - v_n(k)$ such that $e_i(k)$ is the value of $E_m < \delta$ at every sampling instant.

Cost function

The objective of the auxiliary current controller is to minimise the error between the reference current and the predicted current, that is

$$g = |I_{ref}(k+1) - I_2(k+1)|. \tag{4.26}$$

4.5.2 Implementation of a FCS MPC based active SFCL LVRT strategy for the grid connected VSG

The analysis provided in subsection 4.5.1 are based on the per phase representation of the system. The designed VSG, however, is a three phase unit. Therefore, in order to use the same equations in the analysis for implementation purposes, the three phase measured quantities should be converted into orthogonal coordinates using a unitary operator 'a'. Moreover, the computed current using impedance model (see chapter 3) should be transformed, first, into its equivalent three phase quantities and finally, into orthogonal coordinates using 'a'. Figure 4.6 provides the block diagram of the VSG operated under virtual power circle PQ decoupling scheme and with an active SFCL

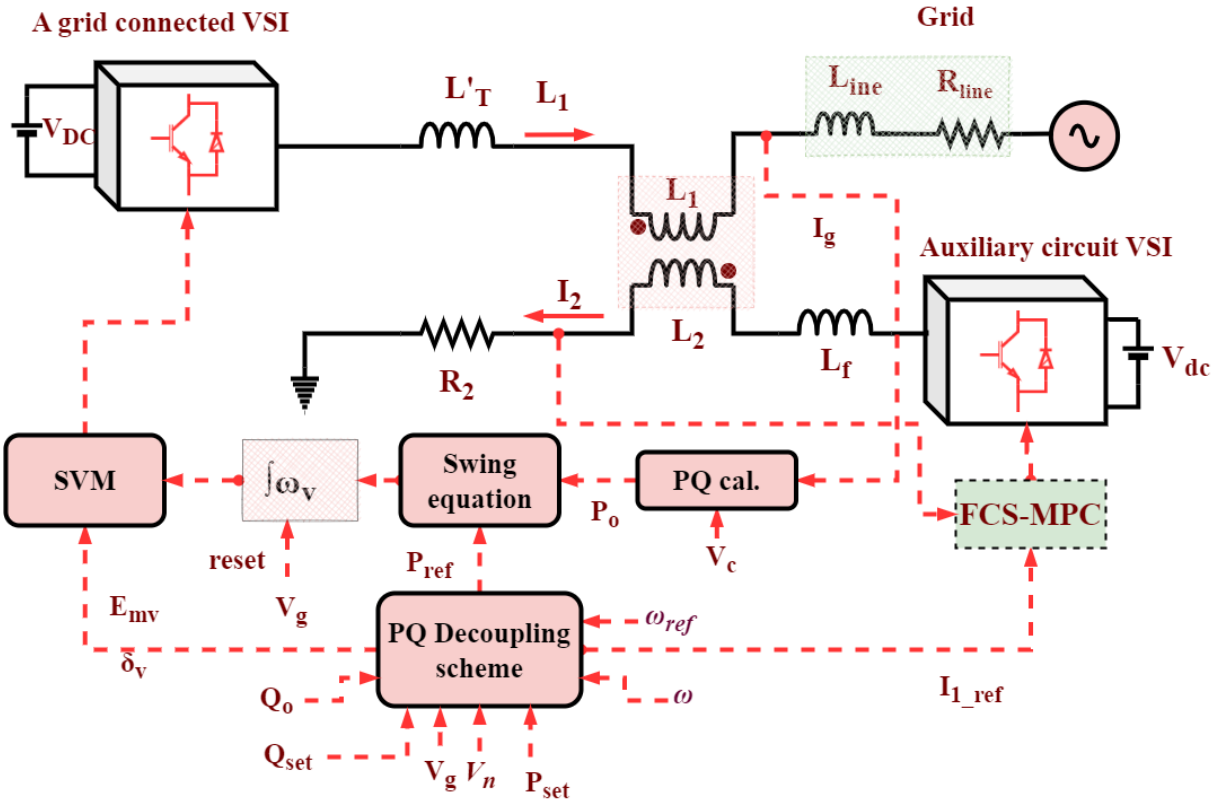

Figure 4.6: *A block diagram of the VSG with PQ decoupling scheme and active SFCL driven by FCS-MPC*

driven by the FCS-MPC. It is can be observed that the difference with the implementation diagram presented in chapter 3 is the addition of the flux coupling inductors and the auxiliary circuit with its corresponding FCS-MPC based controller.

Modifications to the synchronverter controller presented in chapter 3

The technique presented is that, the flux coupling inductors to be physically presented in the circuit but operational wise they are non existent (see 4.5.1). This is implemented by replacing the measured grid voltage (V_g) by nominal rated grid voltage (V_n) in the impedance model. The rest of operation remains as in chapter 3. For the sake of completeness, the operation of the proposed PQ decoupling scheme in chapter 3; the purpose of the PQ decoupling scheme is to select the virtual power circle through which a decoupled PQ control is achieved. To select the required virtual power circle, power reference references (P_{ref} and Q_{ref}) must be computed. These are calculated on basis of the P–f and Q–V droop controllers (see chapter 3, equation (3.5)), which require the measured values of grid angular frequency ω and voltage (V_g) as well as

the defined/specified values of angular frequency (ω_{ref}), reference voltage ($V_{ref} = V_n$), Q_{set} and P_{set}. Then γ is obtained as discussed in chapter 3, from which then the virtual capacitance C_v is computed. Moreover, the required magnitude of the internal voltage (E_m) and power angle (δ) are as well computed as follows:

$$E_m = \left(\frac{2\gamma\sqrt{X^2 + R^2}}{3V_g} Q_{\text{ref}} \right) + V_g. \tag{4.27}$$

$$\delta = \arcsin \left(\frac{2\gamma\sqrt{X^2 + R^2}}{3V_g E_m} P_{ref} \right). \tag{4.28}$$

The modified synchronverter (see chapter 3), however, receives virtual power angle (δ_v) and virtual amplitude of the internal voltage (E_{mv}) as input to its modulator. These are computed from the impedance model of the grid connected inverter (given in Fig. 3.10). The model is slightly modified, that is, instead of using the measured grid voltage ($V_g \leq \theta$) it uses the rated grid voltage ($V_n \leq \theta$). That is,

$$I_{1ref} = \frac{E_m \leq (\theta + \delta) - V_g \leq \theta}{Z_v + Z} \tag{4.29}$$

$$E_{mv} \leq (\theta + \delta_v) = E_m \leq (\theta + \delta) - (Z_v I_{1ref}) \tag{4.30}$$

These implements (4.12), such that $I_1 = I_{1ref}$. Hence, the main circuit will never observes any voltage sags. Then, I_{1ref} is used to compute the reference current (I_{ref}) in the FCS-MPC controller while δ_v and E_{mv} are used in the SVM block to generate switching signals for the VSG in the main circuit.

Implementation of the FCS-MPC for the auxiliary inverter

Figure 4.7 provide the flow diagram for the operation of the FCS-MPC based auxiliary controller.It is shown that to generate the optimal switching states for the power semiconductor switches of the auxiliary VSI, the auxiliary current I_2 is measured and then rolling optimization follows. That is, for each of the eight voltage vectors given in table 4.1, a one step ahead auxiliary current prediction is done. Then, the voltage vector V' that minimises the cost function (formulated using the predicted current–as per equation (4.23) and reference current which is formulated as per equation (4.25))is selected. The

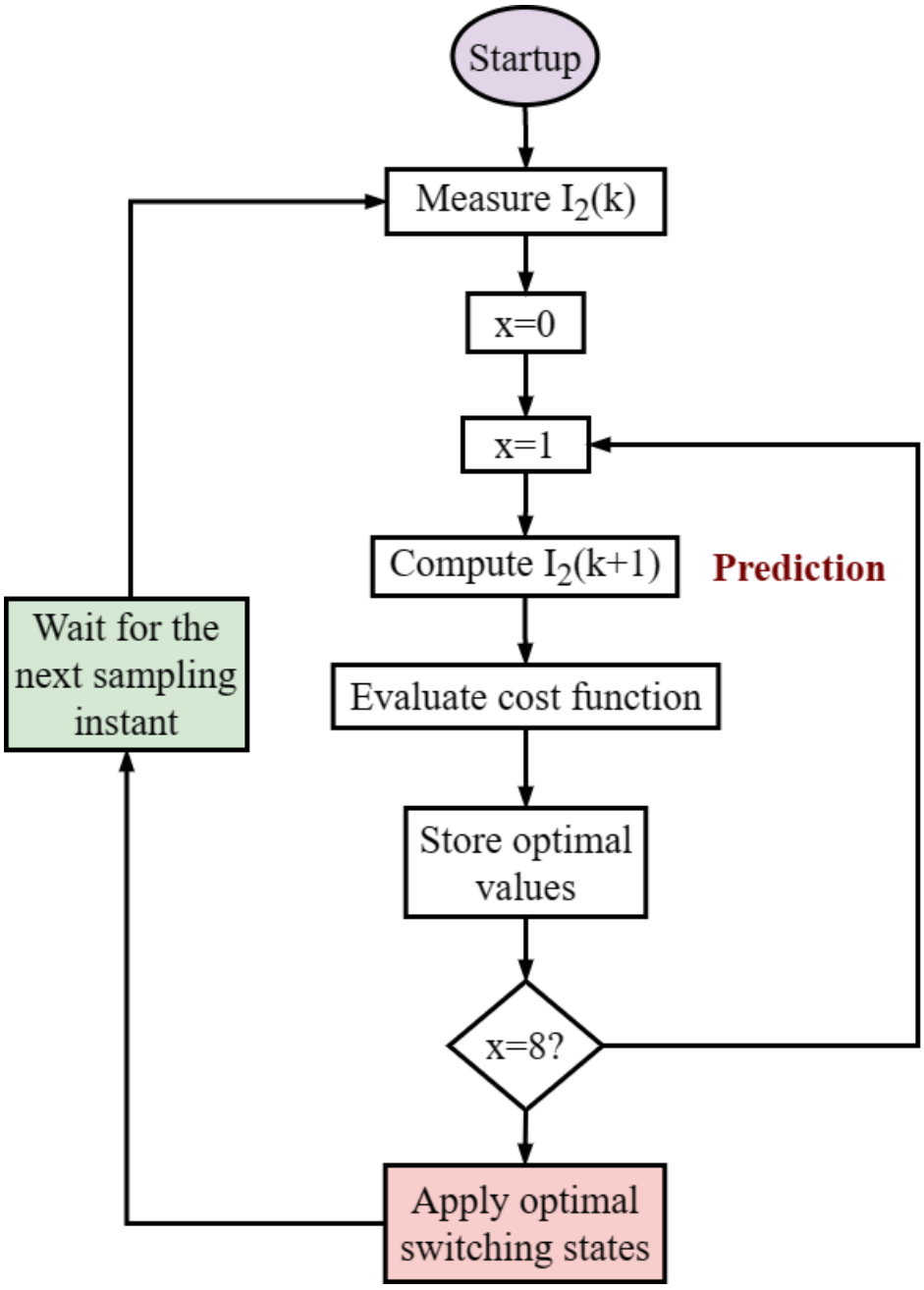

Figure 4.7: *A flow diagram of the FCS-MPC controller for the the auxiliary VSI*

selected voltage vector V'_{opt} is constituted by the optimal switching states of the VSI. These switching states are then applied to the auxiliary VSI.

The predicted current requires measurement of the grid voltage (V_g), auxiliary current(I_2) and knowledge–values of rated nominal grid voltage (V_n) and the values of the flux coupling circuit (L_1, L_2, K). To design these values, let us consider the reference current (I_{ref}) as given by (4.25) which can be rewritten as:

$$I_{ref} = \frac{\Delta V_g}{j\omega M} + \frac{L_1}{M} I_{1ref} \tag{4.31}$$

The following can be observed from (4.31);

i . Under normal conditions $\Delta V_g = 0$, hence, $I_{ref} = \frac{L_1}{M} I_{1ref}$. Since $M = K\sqrt{L_1 L_2}$, then $I_{ref} = \frac{1}{K}\sqrt{\frac{L_1}{L_2}} I_{1ref}$. If $K \approx 1$ and $L_1 \approx L_2$, then $I_{ref} = I_{1ref}$. This means that both auxiliary circuit and main circuit are having same current under normal conditions.

ii. If $I_1 = I_2$, then the main circuit and auxiliary circuit can be equivalently designed. This results to a concept of the double VSG design and operation. That is, instead of designing a separate auxiliary circuit, another VSG with similar ratings and same interfacing impedance can be used as an auxiliary circuit. Therefore, same parameters for the VSG and auxiliary circuit has been used in this thesis. That is, a total interfacing impedance of 10 mH is used in the auxiliary circuit, which is equivalent to $(L_i + Lg)$ in parallel with C_f (see chapter 3). This inductive impedance is distributed between L_f and L_2, where 90% is assigned to L_f and 10% to L_2. This assignment is to ensure sufficient filtering by L_f and equivalent quality of the current I_2 to I_1.

iii. During abnormal conditions (that voltage sag) $\Delta V_g > 0$, therefore there occurs a change in I_{ref} by $\frac{\Delta V_g}{j\omega M}$. That is to say, the change/the increase of current in auxiliary circuit is limited by M only. Hence, M can be designed by the levels of the current that is expected to increase. In our particular case, since $K = 1$, and $L_1 = L_2$ then, $M = L_1 = L_2$.

The current prediction is performed for a one step ahead only, while it is known that the long horizons ensures stability and good performance. This is because, in FCS-MPC the possible solutions which are used to solve the optimization problem grow exponentially with the prediction horizon. This results to the intractability problem to the FCS-MPC for the real time applications [165]. It is also known that, the near infinite horizon performance can be achieved with short finite horizons by using a suitable terminal cost function. Determining and computing that terminal cost in a short time (switching period of the inverter) is, however, still an open challenge.

4.6 Simulation and results analysis

To test the efficacy of the proposed FCS-MPC based active SFCL LVRT strategy of the grid connected VSG, a grid connected synchronverter system operated under virtual power circles based PQ decoupling scheme as presented in chapter 3 is modified to include the FCS-MPC based active SFCL as shown in Fig. 4.8. This figure is a per phase block diagram representation of the system considered for simulation studies. The structure of the active SFCL is as provided in Fig. 4.4 and its controller is designed as per subsection 4.5.1. The parameters of grid and synchronverter are as provided in chapter 3, while the parameters of the auxiliary circuit are as given in Table 4.2.

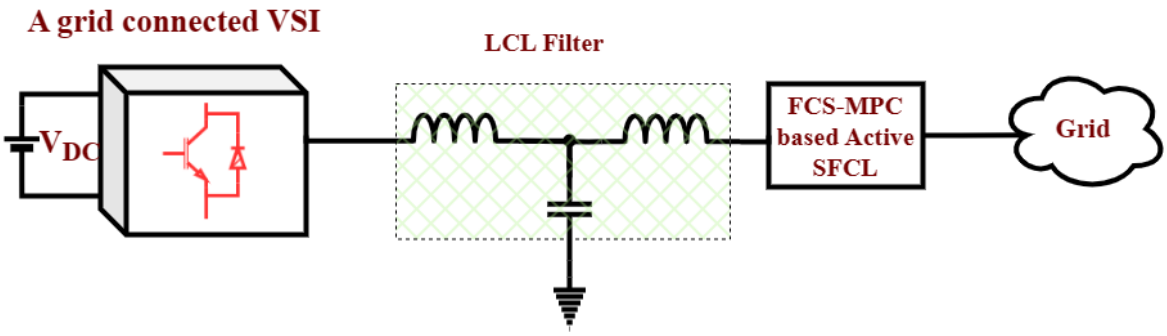

Figure 4.8: A block diagram of the per phase representation of the system used for simulation studies

Table 4.2: *Auxiliary circuit parameters.*

Parameter	Value
DC bus voltage (V_{DC})	$700V$
L_f	$9mF$
$L_1 = L_2 = M$	$2mF$
K	1
R_2	0.5Ω
T_s	$25e^{-6}$

A total of three cases are provided to test the validity of the presented LVRT strategy in relation to the adherence to the current-modified grid codes as given in Fig. 4.1. To provide a better analysis with comparisons to when the strategy is not deployed, two synchronverters are used. That is, the synchronverter presented in chapter 3 and the one which has been modified as per Fig. 4.8. The former shall be referred to as VSG2 while the latter VSG1. The first case aims at analysing the response of the systems' under P

control, that is during mild voltage sags and normal grid conditions. The second case aims at exploring the response of the synchronverters under medium voltage sags. That is, when they are required to transit from the P control at unity power factor to PQ control using droop controllers. The third case, explores the response of the synchronverters when it transit from P control at unity power factor to Q control. Under all cases, the interest is on investigating current responses and maximization of the power transfers.

4.6.1 *Case I: P control during mild voltage sags*

During normal grid conditions and during mild voltage sags, VSGs are required to continue with normal operation as shown in Fig. 4.1. That is, maintaining P control at unit power factor. Therefore, this case is set to demonstrate the response of VSG1 and VSG2 on the occurrence of the mild voltage sag. The simulation results for this scenario are as shown in Fig. 4.9. To obtain these results, systems are initialised and synchronised

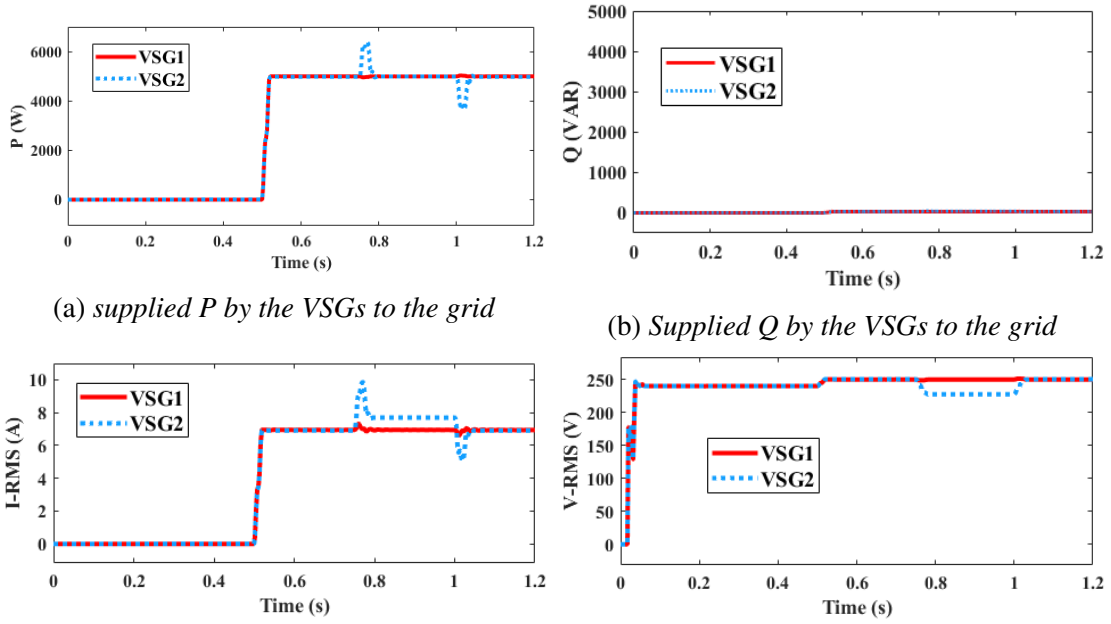

(a) *supplied P by the VSGs to the grid*

(b) *Supplied Q by the VSGs to the grid*

(c) *Supplied current to the grid by the VSGs*

(d) *Capacitor voltage of the VSGs*

Figure 4.9: *Simulation results: Per phase comparative analysis of the response of the VSG1 and VSG2 under a voltage sag of 90%)*

to the grid at 0.2 s. Then, a step change in P is set at 0.5 s from 0 to the rated power of the VSGs, that is 5000 W. It is shown in Fig. 4.9a that all of the VSGs respond to this command and supplies the required P. A voltage sag of 90% is then introduced at time 0.75 s, and the grid recovers to its nominal voltage after 0.25 s. Despite of the occurrence of this voltage sag, it is shown in Fig. 4.9b that both VSGs maintains Q at zero value,

while P is maintained at its rated value as shown in Fig. 4.9a. Hence, both VSG1 and VSG2 obey the current–modified grid codes. Moreover, it is shown in the latter figure that, the VSG1 has a better transient response than VSG2. Figure 4.9c provides the current supplied by both of the VSGs. It is shown that, during a voltage sagging period, there is increase in current for the VSG2. This is due to the decrease of its capacitor voltage as shown in Fig. 4.9d. This is because the VSG2 observes a full voltage sag. Hence, to maintain the constant P supply, current must be increased. However, achieving this during moderate and severe voltage sags may not be feasible, as the significant increase in current could potentially damage the power semiconductor devices of the VSG. This is clearly demonstrated in case 4.6.3. To limit this effect, current is limited to its maximum which means P is curtailed as elaborated in case 4.6.2. This means power transfer during voltage sagging period is limited which upset the power balance in system and resulting in cascading failure. On the other hand, it is shown that the current for VSG1 remains at its rated value and the rated power is supplied during voltage sagging period. This is due to the utilisation of the FCS-MPC based active SFCL such that it compensates for the reduction of the RMS voltage. Hence, VSG1 detects no change in voltage as shown in Fig. 4.9d. Therefore, this ensures maximum utilisation of the available RES-power.

4.6.2 *Case II: PQ control during medium voltage sags*

According to the modified grid codes as shown in Fig. 4.1, a VSG must curtail its P supply, to supply both P and Q during medium voltage sags. This is easily achieved by using Q–V droop controllers and limiting current to its rated value as narrated in subsection 4.5.1. Occurrence of the voltage sags and limitation of the current to its maximum value, however, limits the maximum power that can be transferred to the grid during voltage sagging period. This may provoke frequency stability problem and may even results in a cascading failure. The power transfer can be improved by introducing a FCS-MPC based active SFCL in the circuit, such that maximum power can be harvested from VSGs (RE-generators) while adhering to the grid codes. This is demonstrated in this case as shown in Fig. 4.10.

Similar to case 4.6.1, systems are initialised and synchronised to the grid at around 0.2 s. A step increase in P is set at 0.5s to supply the maximum rated power. A voltage

sag of 70% is introduced at 0.75 s and the grid recovers to its nominal voltage at 1 s. It is shown in Fig. 4.10c that the same maximum RMS current is maintained for both VSGs, noting the difference that a VSG1 has better transient response than VSG2. Moreover,

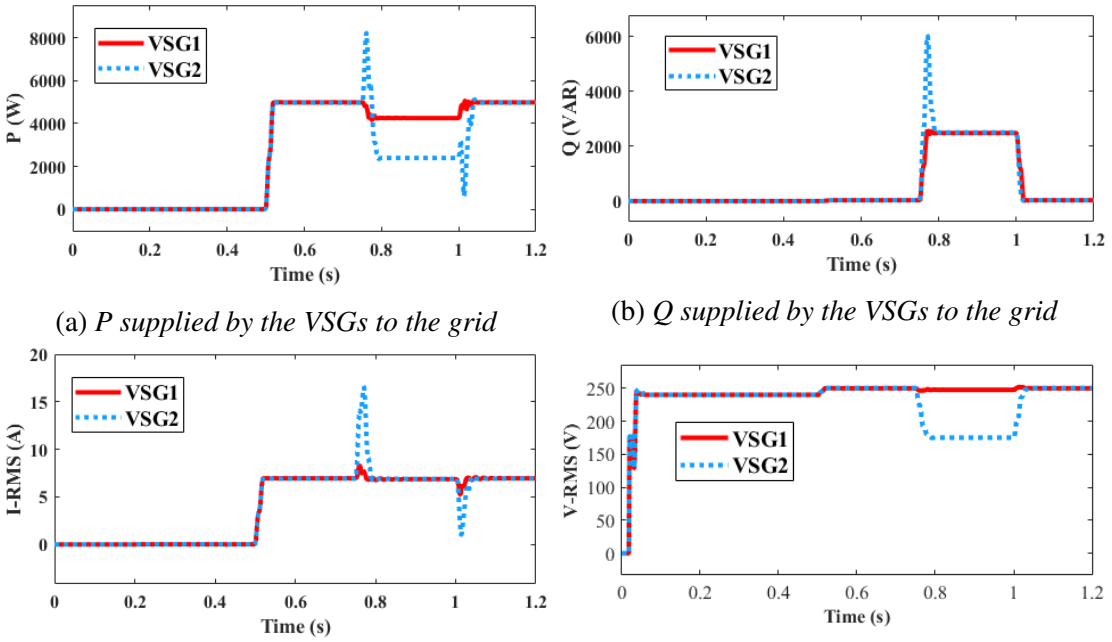

(a) *P supplied by the VSGs to the grid*

(b) *Q supplied by the VSGs to the grid*

(c) *Supplied current to the grid by the VSGs*

(d) *Capacitor voltage of the VSGs*

Figure 4.10: *Simulation results: Per phase comparative analysis of the response of the VSG1 and VSG2 under a voltage sag of 70%)*

Fig. 4.10b shows that same Q is supplied by both VSGs. Similarly to Fig. 4.10c, VSG1 shows better transient response. Contrary to the current and Q response, it is shown in Fig. 4.10a that there is much more curtailing in P for the VSG2 compared to VSG1. This is due to the ability of the VSG1 to maintain operation on the PQ power circle that existed prior to the occurrence of the voltage sag. This is achieved by compensation of the decreased voltage by the FCS-MPC based active SFCL. This is different to the VSG2 such that collapsing of the PQ power circle due to onset of the voltage sags (as shown in Fig. 4.3), the power transfer from VSG2 to the grid is limited. The non collapse of the PQ power for the VSG1 is due to the fact that, the VSG sees no such sag as shown in Fig. 4.10d. In this figure, it is also shown that the VSG2 observes a full voltage sag. The sudden decline in P supply from the VSG2 during voltage sags has two disadvantages. First, it might cause power imbalance problems which might results in frequency instability problems. This is due to the upsetting of the power balance in the system. Secondly, to the power producers supplying maximum power maximize their

profit. Hence, this decline constraints potential income gain. Therefore, the deployment of the FCS-MPC based SFCL for LVRT ensures multiple benefits for grid connected VSG.

4.6.3 *Case III: P to Q control during extreme voltage sags*

This case is set to demonstrate the ability of the presented LVRT strategy in riding through extreme voltage sags. Systems are initialised and synchronised to the grid at around 0.2 s as in previous cases. A step increase in P from 0 to 5000 W is invoked at 0.5 s as shown in Fig. 4.11a. This power is supplied at unity power factor as it can be seen in Figs. 4.11a and 4.11b, that is between 0.5 s and 0.75 s P is 5000 s while Q is zero, respectively. This is a constant P-control during normal condition as per grid codes as shown in Fig. 4.1. A voltage sag of 30% is introduced at 0.75 s and the grid recovers to its normal condition after 0.25 s. According to Fig. 4.1 this is a severe sag,

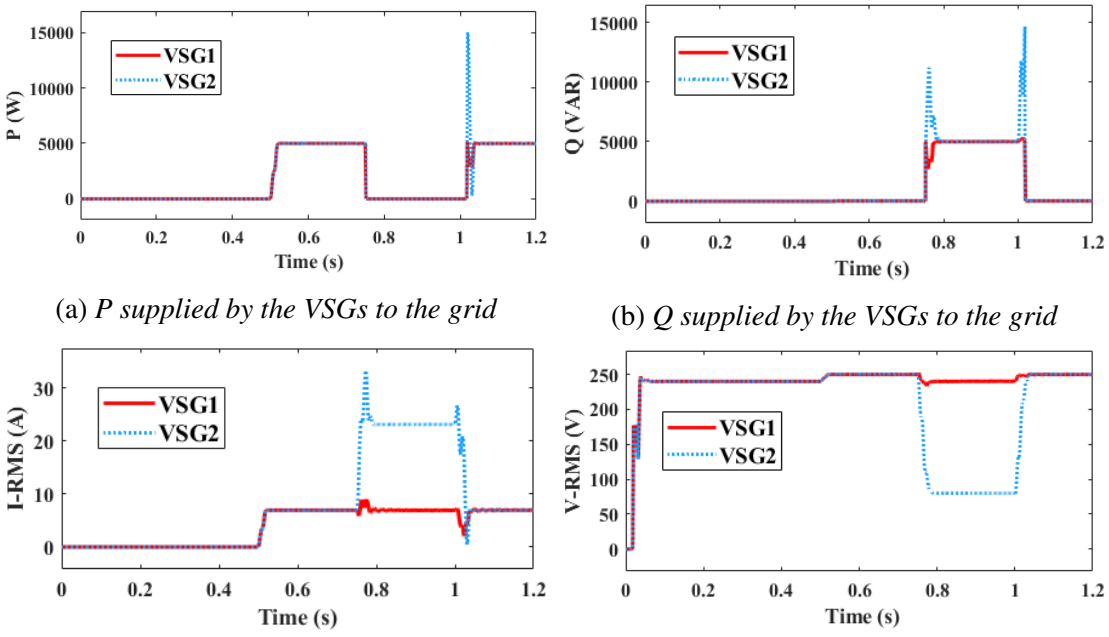

(a) *P supplied by the VSGs to the grid*

(b) *Q supplied by the VSGs to the grid*

(c) *Supplied current to the grid by the VSGs*

(d) *Capacitor voltage of the VSGs*

Figure 4.11: *Simulation results: Per phase comparative analysis of the response of the VSG1 and VSG2 under a voltage sag ofof 30%)*

hence the VSGs must transit from P control to Q control. This is achieved as shown in Figs. 4.11a and 4.11b, that is P goes to zero and Q goes to its rated value to aid the grid recovering to its nominal voltage. This control is maintained until when the grid recovers to its nominal voltage at 1 s.

It is shown in Fig. 4.11c that, to ride through this voltage sag (while adhering to the grid codes and ensuring maximum power harvest from the RE-generator) for a VSG2 with no any LVRT strategy, a huge current flows. The current is almost 6 times the nominal rating current. This is sufficient to destroy the power semiconductor devices of the VSG. This current could be limited as in case 4.6.2, however, the Q transferred will have to be curtailed. Therefore, this case demonstrates how detrimental it can be by trying to harvest the maximum power during voltage sags without using active SFCL. Moreover, there are two poor transient events in current responses for VSG2, that is, during inception of the sag and during voltage recovery. On the other hand, it is shown that the VSG1 which uses a FCS-MPC based active SFCL for LVRT, can ride through the initiated voltage sag with almost perfect transient events as shown in Fig. 4.11c while adhering to the current modified grid codes. It is shown both current (in Fig. 4.11c) and power in Fig. 4.9a are maintained at the rated value. This is due to ability of the proposed strategy to maintain operation on the virtual PQ power circle that was present prior to the occurrence of the voltage sag. Therefore, the use of FCS-MPC based active SFCL for providing LVRT improves both transient responses on the occurrence of the voltage sags and during grid voltage recovery, as well as maximises the power transfer during voltage sagging period.

4.7 Summary

A FCS-MPC based active SFCL design for the LVRT of the grid connected VSG has been presented in this chapter. It has been demonstrated that, the design ensures maximum power harvest during voltage sags with improved transient response. The major constraint to this approach is the cost of the system due to the addition of the flux coupling inductors and an auxiliary VSI. One of the mitigative approaches in minimising the cost of the system is by replacing the auxiliary VSI with another VSG, such that one can aid the other on occurance of the voltage sags. This will remove the additional cost for the auxiliary VSI. This approach, however, requires a proper design and coordination between the two VSGs. This is left as a future work in this thesis as discussed in chapter 6.

Chapter 5

Inertia Estimation Methods in a Power System

This chapter provides a literature review of the methods for estimating inertia constants in a power system. The challenges of applicability of these methods in the low inertia power systems are highlighted. Then, a neural network based method is presented as a way forward for stochastic inertia estimation in the low inertia power system. The method uses as a simple multilayer perceptron (MLP) neural network. To obtain inertia of the system, the inertia active power response is estimated together with its corresponding RoCoF and supplied to the MLP neural network. The active power is estimated by analysing the power flows in the system. That is, the change in the active power flows in a respective bus is observed and averaged in a window of 2 s. Then, the correspond RoCoF in that particular bus is evaluated in a similar manner. These data are obtained from the phasor measurement units (PMU). Hence, inertia of the power system is explicitly estimated. The applicability of the method is validated by using the New England power system and its corresponding weak grid. The latter is obtained by modifying the former system, that is, by replacing the synchronous generators (SG) with RES. It is validated that the method can perform online estimation of the system's inertia under normal operating conditions. The method is computationally inexpensive and explicitly extracts inertia which is an added advantage over most of the model-based estimation approaches.

Chapters 3 and 4 collectively address the design and control of a Virtual Synchronous Generator (VSG) connected to a weak grid, forming the foundation for this chapter's focus on inertia estimation in such grids. This chapter serves as a crucial step in the overarching research framework by providing the methodology needed to estimate system inertia accurately, a key requirement for designing an adaptive VSG. The ultimate objective is to enable a VSG capable of dynamically adjusting its parameters based on

real-time inertia estimation, enhancing its performance in weak grid conditions. While this chapter lays the groundwork for such adaptive functionality, the integration of the VSG design from Chapters 3 and 4 with the inertia estimation methodology remains an open task, outlined as future work in Chapter 6. This relationship underscores the progressive and interconnected structure of the research, demonstrating how each chapter contributes to the broader goal of advancing VSG technology in weak grid applications.

5.1 Introduction

The stochastic nature of renewable energy sources (RES) impacts the number of synchronous generators (SG) committed to the system, leading to variable system inertia. Low inertia poses a threat to the system's security and stability, necessitating proper planning to optimize available resources during frequency contingencies. Therefore, continuously understanding the system's inertia values is essential. With accurate knowledge of available inertia, adaptive protective systems can be designed, and resources can be allocated appropriately to limit the rate of change of frequency (RoCoF) and contain frequency deviations during contingencies.

There is a large literature on proposed methods for estimation of the power system's inertia. Nevertheless, very few papers provide a comprehensive classification of these methods [97, 166]. Evelyn et al. [97] classified inertia estimation methods according to the time horizon in which the estimation is performed; where the methods are classified into offline estimation, online estimation and forecasting methods. In *offline methods*, inertia is estimated after occurrence of frequency excursions in the system. These methods are important for systems' analysis and planning [24]. However, they are not suitable for adaptive control schemes since they are based on post-mortem analysis [167]. On the other hand, *online methods* involve monitoring and estimation of the system's inertia on real time. These methods are vital for adaptive protection schemes [168, 169]. *Forecasting methods* involve prediction of the inertia that will be available in the system in the future. This is important in operating low inertia power system since the time for containing frequency deviations is limited [97]. Hence, prior understanding of the available inertia is important for advance deployment of mitigative measures [170].

Tan et al. [166] classified inertia estimation methods according to the type of the

model and magnitude of the disturbance that was used for the estimation. In the model based estimation, methods are classified into a single synchronous generator (SG) inertia estimation and regional wise estimation. While, in terms of the magnitude of disturbance, the methods are categorized into small disturbance based (SDB) approaches and large disturbance based (LDB) approaches. Generally, in SDB inertia is estimated by using data from the ambient measurements of frequency and power, whereas LDB involves the use of transient frequency measurements and a known or estimated size of disturbance for inertia estimation.

Contrary to [166] and [97], this work classifies inertia according to the deployment of the swing equation in estimation. In a power system, frequency dynamics are governed by the available inertia prior to the occurrence of a frequency contingency. The relationship between inertia and frequency dynamics in the power system is quantified by using a swing equation. Hence, the state of the art methods deployed by the PSO and the proposed methods on literature are based on the utilisation of the swing equation. Some literature uses it directly, while others indirectly. Therefore, inertia estimation methods can be classified into *direct swing equation based methods*, *indirect swing equation based methods* and *statistical method* as shown in Figure 5.1. Before providing descriptions of the latter classification, lets first analyse the swing equation. Frequency variations in the power systems are caused by the mismatch between the supply and demand. In the traditional power system, this mismatch is defined by the imbalance in mechanical and electrical power seen by the SGs. The rate of change of the speed (frequency) in each of the SG is governed by its available inertia and the respective power change that it has sensed. This relationship is quantified by the swing equation which is

$$2H \cdot \frac{d(\Delta f)}{dt} + D \cdot \Delta f = \Delta P_m(t) - \Delta P_e(t) \tag{5.1}$$

where H is the inertia constant, f is the frequency, $\frac{d(\Delta f)}{dt}$ is the RoCoF, D is the damping, P_m is the mechanical power, P_e is the electrical power and Δ denotes change from steady state value. Since, inertia response lasts for short duration (up to 5s), the change in mechanical power is assumed to be constant during this period. Thus (5.1) becomes

$$2H \cdot \frac{d(\Delta f)}{dt} + D \cdot \Delta f = -\Delta P_e(t). \tag{5.2}$$

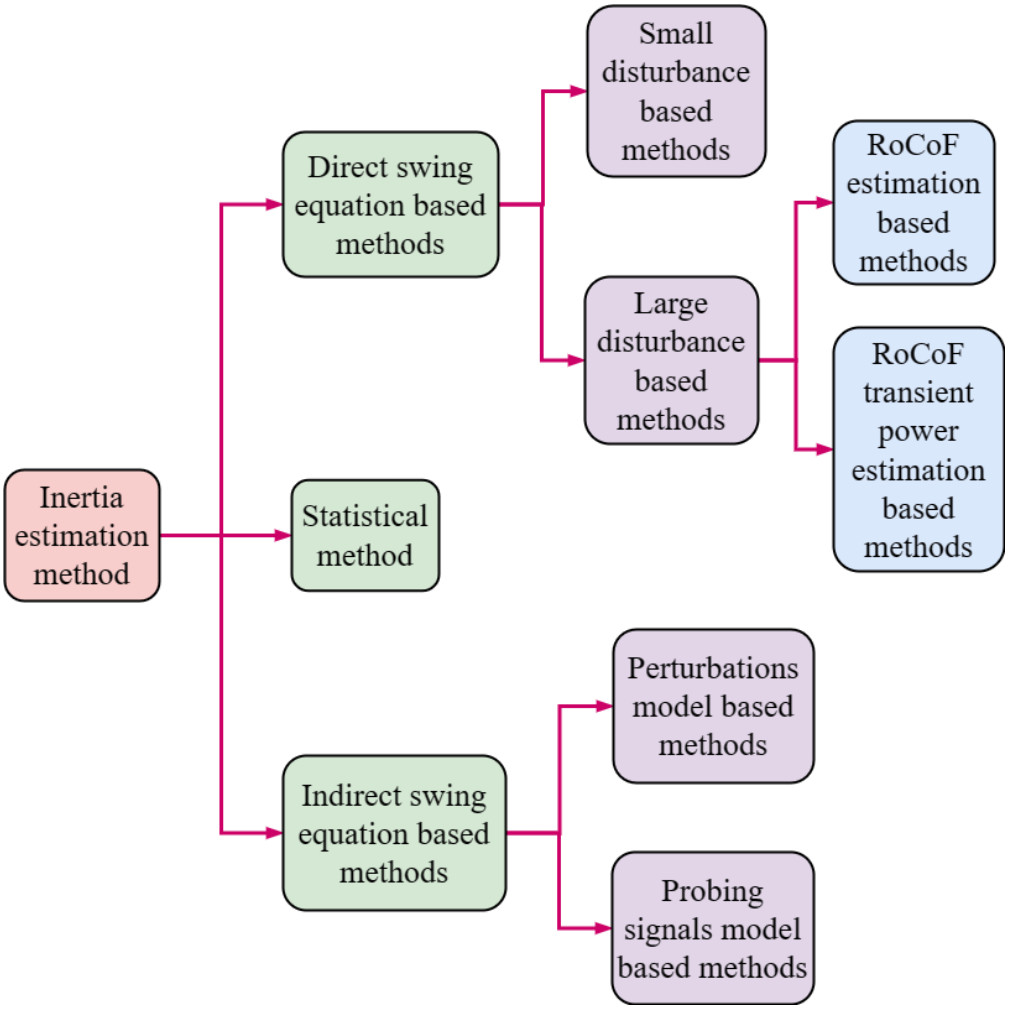

Figure 5.1: *Classification of inertia estimation method*

Since a power system is composed of many SGs, it is desirable/required to provide a full system performance/response. In that context, the SGs are aggregated and represented by the single equivalent generator [24, 71]. Therefore, inter machine oscillations and transmission system performance are ignored. Hence

$$2H_{sys} \cdot \frac{d(\Delta f_{COI})}{dt} + D \cdot \Delta f_{COI} = -\Delta P_e(t) \tag{5.3}$$

is used for load-frequency control analysis in the power system; where H_{sys} is the equivalent inertia constant of the generators and f_{COI} is the center of inertia frequency. H_{sys} is the weighted mean of the inertia constants of the generators such that weights applied to each inertia constant are the individual power ratings of the generators (s_k). This is quantified as

$$H_{sys} = \frac{\sum_{k=1}^{N} H_k \cdot s_k}{S_B}. \tag{5.4}$$

where S_B is the base power. f_{COI} is the center of inertia frequency, which is defined as the weighted mean frequency in which the mean weights are the individual machine's inertia constant (H_k). This is given by

$$f_{COI} = \frac{\sum_{k=1}^{N} H_k \cdot f_k}{\sum_{k=1}^{N} H_k}. \tag{5.5}$$

The concept of the center of inertia frequency is significantly important since in a multi-generator system, frequency oscillates [24]. Hence, f_{COI} provides the best system's frequency representation of analysis. Equation (5.3) can thus be rearranged to be

$$\frac{d(\Delta f_{COI})}{dt} + (\frac{D}{2H_{sys}}) \cdot \Delta f_{COI} = \frac{-\Delta P}{2H_{sys}}. \tag{5.6}$$

From this rearrangement, it can be observed that at the onset of the disturbance (that is prior to the occurrence of the change in active power the system is at steady state, hence the change starts at $t = 0$ where $\Delta f_{COI} = 0$), RoCoF is

$$\frac{d(\Delta f_{COI})}{dt} = \frac{-\Delta P}{2H_{sys}}. \tag{5.7}$$

This means that, RoCoF is determined by the size of the disturbance and the available inertia in the system. Therefore, if both RoCoF and the size of imbalance/disturbance can be accurately determined, then inertia constant of the system can easily be estimated. With this knowledge, we can now provide a comprehensive literature review on inertia estimation methods in power systems, as detailed in Section 5.2. This review is crucial because it establishes a foundation for developing new inertia estimation methods for low inertia power systems. Additionally, it will identify clear research gaps that will be addressed in our proposed approach–a neural network based inertia estimation method, outlined in Section 5.3. Section 5.4 verifies the validity of the proposed approach by using the New England power system and its corresponding modified system. The latter is done by replacing the SGs with RES generators–so as to test the efficacy of the proposed approach in a system with large amount of RES generators. The chapter is concluded with a summary provided in Section 5.6.

5.2 A literature review of the inertia estimation methods in power systems

Figure 5.1 provides classification of the inertia estimation methods, where the methods are categorized into; *direct swing equation based methods*, *statistical based method* and *indirect swing equation based methods* which are explained in a sequel.

5.2.1 Direct swing equation based methods

In this approach, a simplified swing equation is used directly. Based on (5.7), if both the RoCoF and the size of the power imbalance are known, system's inertia can easily be estimated. RoCoF is the resulting effect of the occurrence of the disturbance in the system; a *disturbance* refers to as an event in the power system that upsets the power balance in the system. Thus, from the known size of the disturbance in the system, RoCoF can be estimated and hence system's inertia. Hence, inertia estimation methods are categorized into *large disturbance based methods* and *small disturbance based methods*.

Large disturbance based (LDB) methods

These are methods which rely on the occurrence of the large disturbances on system such as loss of generation, load rejection, faults in the system (e.g. symmetrical short circuit) etc. Once a disturbance has occurred, active power balance in the power system is disturbed such that frequency dynamics are stimulated. First few seconds (approximately 2 seconds) from the occurrence of the disturbance, frequency dynamics (RoCof and frequency nadir) are entirely dependent on the available inertia in the system. Hence, if both RoCoF and the size of imbalance are known or can be estimated, then inertia can easily be estimated based on the simplified swing equation as given in (5.7). Therefore, depending on which parameter is estimated and which is known, LBD methods are further classified into; *RoCoF estimation based methods* and *RoCoF—transient power estimation based methods*.

LDB–RoCoF estimation based methods

In these methods, inertia is estimated by evaluating RoCoF from the transient frequency at the onset of the known size of the disturbance using (5.7) directly. The measured transient frequency includes noise and oscillatory components, impacting the accuracy of this method. This noise affects the determination of the disturbance onset and the Rate of Change of Frequency (RoCoF) calculations, both of which are crucial for the successful application of this approach.

The methodology was first introduced by Inoue et al. [171] in 1997, when estimating inertia of the power system of Japan. A combination of 10 events from the load rejections, line switching and the loss of the generations were used. Noise influence from the transient signal were eliminated by using moving a average filter. The onset of the disturbances were identified by measuring RoCoF, that is, if RoCoF exceeds 0.04 Hz/s for the first time then an event is deemed to have started. While, RoCoF for inertia estimation is evaluated by using a fifth order curve fitting approach. The curve fitting is important in circumventing the oscillatory components of the transient signals. After fitting a polynomial, RoCoF is estimated by evaluating the derivative of the polynomial at the onset of the disturbance. Then (5.7), with the known size of a disturbance and the estimated RoCoF, is used to evaluate the inertia of the power system.

In Refs. [172, 173] the method deployed by Inoue et al. [171] was used to estimate inertia in the WECC power system. In [173], inertia is estimated from 32 real events which involved loss of generations from 2009 to 2011. While in [172], the method was deployed in an effort to build a computerized model for estimating inertia during disturbances. A total of 388 major disturbances on the system were collected from May, 2002 to June, 2004. However, the model was built using only 137 events in which inertia was successfully computed. Based on this fact, these events results into the frequency below the pre-specified threshold. Despite this success, the method resulted into significant errors. Therefore, authors in [172], called for more precise methods for filtering and RoCoF estimation.

On the other hand, the inertia constant of the GB power system was estimated using transient frequency from synchrophasor measurements in Refs. [96, 174]. To improve the accuracy of the method, frequency is estimated from the time derivative of the phase angle. Moreover, contrary to [171–173], the onset of a disturbance is determined

using modified detrended fluctuation analysis (DFA). Furthermore, determination of the RoCoF from the derivative of the fitted fifth order polynomial on the transient frequency is confirmed to be unsuitable in GB power system [174]. Alternatively, Ashton et al. [96] used a low pass filter to circumvent the oscillations. Then, an averaging sliding window approach with a window size of 500ms on the frequency measurement was used to estimate RoCoF. This method of estimating RoCoF is free from the dependency of the frequency effects outside the inertia control time scale, which constrain the curve fitting approach.

Contrary to proposed methodologies in [96, 171–174], Sun et al. [175] estimated RoCoF using a linear frequency model. The model used is a linear function of the constant average frequency and unknown-time variable RoCoF and noise. By appropriate sampling of the transient frequency signals during a disturbance, several values of RoCoF can be fitted into the model. Therefore, the accurate value of RoCoF is estimated by using least squares method. This method is based on calculation of the inertia from the wide area measurements (WAMS) through using phasor measurements units (PMU).

The proposed methodologies in [96, 171–175] ***result, nonetheless, in inaccurate estimation of system inertia***. This is primarily due to the assumption that the size of disturbance is known. This assumption is invalid, due to the fact that power change during a disturbance is dictated by frequency and voltage dynamics in the system [31, 176]. Therefore, incorrect size of the event results into an inaccurate inertia estimate. Moreover, the methods are offline and based on post mortem analysis. Hence, they are not suitable for the inertia adaptive protection schemes.

LDB RoCoF-transient power estimation based methods

In these methods, the size of the disturbance is estimated based on the active power dynamics on the occurrence of the disturbance. These dynamics to a large extent are influenced by the voltage and frequency response of the system. Hence, the size of the disturbance is estimated considering these influencing factors. Then, RoCoF is estimated and (5.7) is directly used to estimate the available inertia in the system. This approach aims at improving the accuracy of the inertia estimate from the assumption that the size of the disturbance is known. In [30] a frequency dependent function (R approach) is introduced to capture the effects of the frequency dynamics on the size of the disturbance.

The frequency dependent power dynamics are associated with the governor's action and the frequency dependent loads.

On the other hand, Zografos et al. [32] models the effects of the voltage fluctuation on the size of the disturbance. At the onset of the disturbance, voltage fluctuates which invokes the variation of the active power [177]. Therefore, Zografos and Ghandhari [32] introduced a voltage dependent function (V approach) to capture these voltage dynamics on the size of the disturbance. While, [31] combined R and V approach to model both voltage and frequency dynamics (RV approach) on calculating the size of the disturbance. Contrary to RV approach, in [30] inertia is estimated by minimization of the cost function after aggregating frequency and voltage dynamics on the swing equation. The function is minimized by using particle swarm optimization technique.

In [33, 34] four sliding windows are used to estimate inertia of the power system after the occurrence of the disturbance. Two windows are used for estimating the size of the disturbance, while the other two are used for RoCoF estimation. The two literatures differ on the estimation of the onset of the disturbance; while [33] assumes a known time of the onset of the event, [34] uses the convergent properties of the windowing process to estimate the onset of the disturbance. This improves the accuracy of the estimate compared to the assumption of the known time of the onset of the disturbance.

The analysed methodologies in [30–34] are suitable for a large power system dominated by SGs. This is because they ignore variation of the size of the disturbance by the non-synchronous devices such as the response from the RES, ESS and HVDC links (that is inertia emulation from the VSGs) [178]. Therefore, Wilson et al. [178] models the effects of the non-synchronous devices in estimation of the size of the disturbance. The efficacy of the method is tested on Scottish Power networks. On the other hand, Chitaranjan et al. [177] considers a small islanded power system (a microgrid), where the size of the disturbance is estimated by using a fifth order polynomial fit on the active power measurements in a window of 1 s after the occurrence of the disturbance. Moreover, contrary to [171, 172], a variable order polynomial fit is used on the frequency measurements in the same time frame to estimate RoCoF. These modifications showed improvements in the inertia estimate by considering the contributions from the VSGs. Despite of the noticeable improvements from the transient frequency based estimation methods, the accuracy of the inertia estimate of the latter methodologies is challenged by

the determination of the onset of the disturbance. Moreover, most of the methods are offline which limits their applicability in adaptive control or protection schemes.

Figure 5.2 provides general procedures for inertia estimation using LDB methods. It should be noted that the size of disturbance can either be known, or estimated from transient power measurements using curve fitting approach or by incorporating the change of size of disturbance from voltage and frequency dynamics as narrated above.

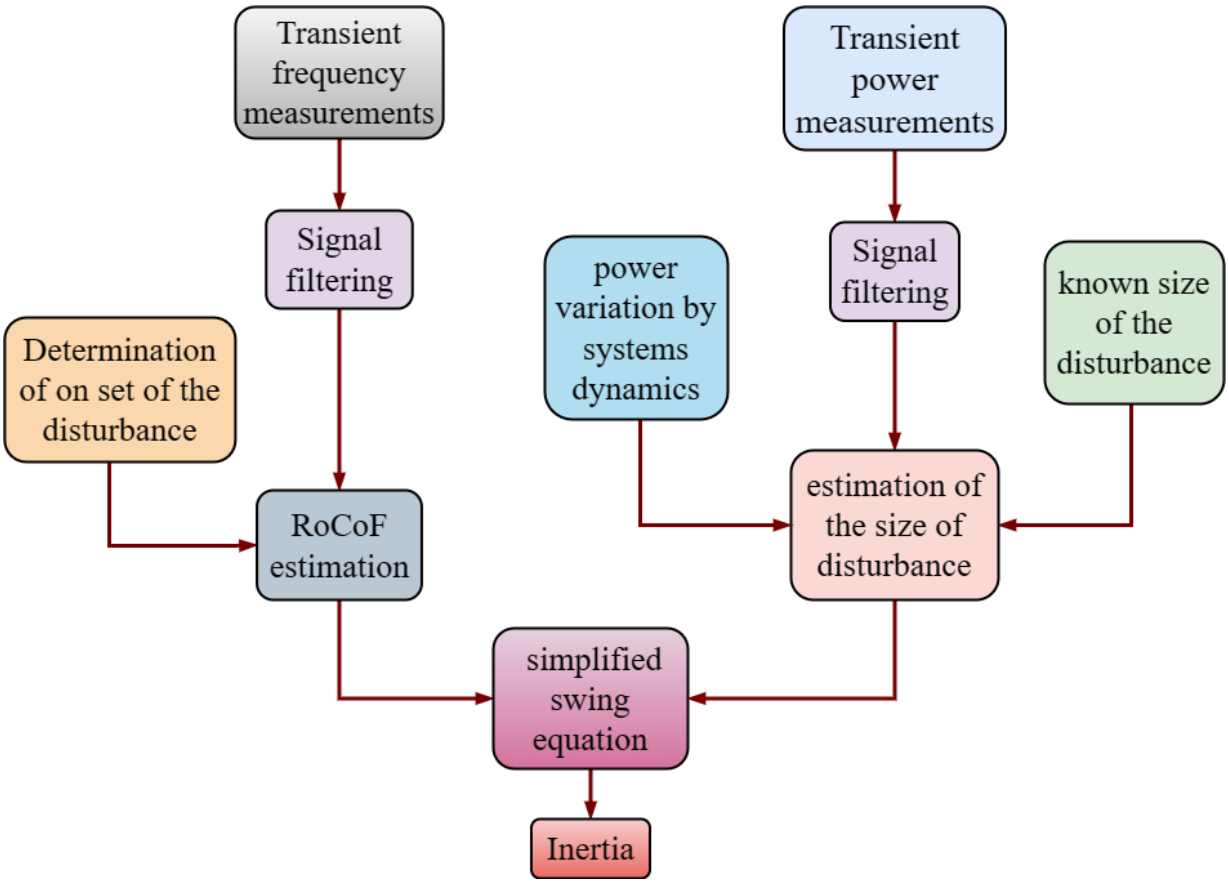

Figure 5.2: *Procedures for LDB based inertia estimation methods in power systems*

Challenges of the LDB methods

The major challenges of the LDB methods are the limited accuracy of the inertia estimate and difficulties in the online implementation of the methods. The accuracy of the estimate is limited by the difficulties in estimating RoCoF–particularly in a low inertia power system where there are significant oscillations. Moreover, the accuracy of the inertia

estimate is limited by the complexity in determining the onset of the disturbances and their accurate sizes. On the other hand, these methodologies are contingent to the occurrence of the large disturbances on the system. These events rarely occur in the system and hence, makes it difficult to continuously monitor inertia and set back practical applicability of the method. The number of these events may be increased by deliberately setting up the disturbances on line. This method, however, is expensive and intrusive to the system. Furthermore, the fragmentation of the system by the penetration of RES and its corresponding frequency variations complicates the inertia estimation process using LDB methods.

Small disturbances-perturbation based (SDB) methods

In these methods a power system is perturbed by the active power variations and (5.7) is directly used for the estimation of the available inertia at the time. Figure 5.3 provides the general procedures for the estimation of the system's inertia by using SDB methods. This approach was firstly introduced by Naoki et al. [179] while estimating the inertia of the power system of Japan. The active power perturbations were created by a device known as the modulator. This device injects a small signal of the active power variations that creates power frequency changes. Following frequency variations, RoCoF is estimated using averaging window and then (5.7) is deployed to estimate the inertia of the power system. Despite its simplicity in estimating the available inertia, the method is intrusive to the system and threatens the system security.

Instead of using a modulator, Best et al. [180] considered the perturbations of the active power in a flow switch on the high voltage direct current (HVDC) interconnector which interconnects between Ireland and GB power systems. Inertia is estimated by observing the active power importation and exportation on the HVDC interconnector. Following an active power perturb, that is either exportation or importation of the active power, frequency dynamics are invoked in the system. From these dyamics, RoCoF is estimated and inertia is directly estimated using (5.7). The method is quite straight forward and requires few measurements. However, it lacks accuracy which is caused by the inaccuracy in determining the size of the active power perturb. That is, the method does not include frequency and voltage dynamics on determining the magnitude of the change in the active power. Therefore, the method suffers from the same drawbacks as

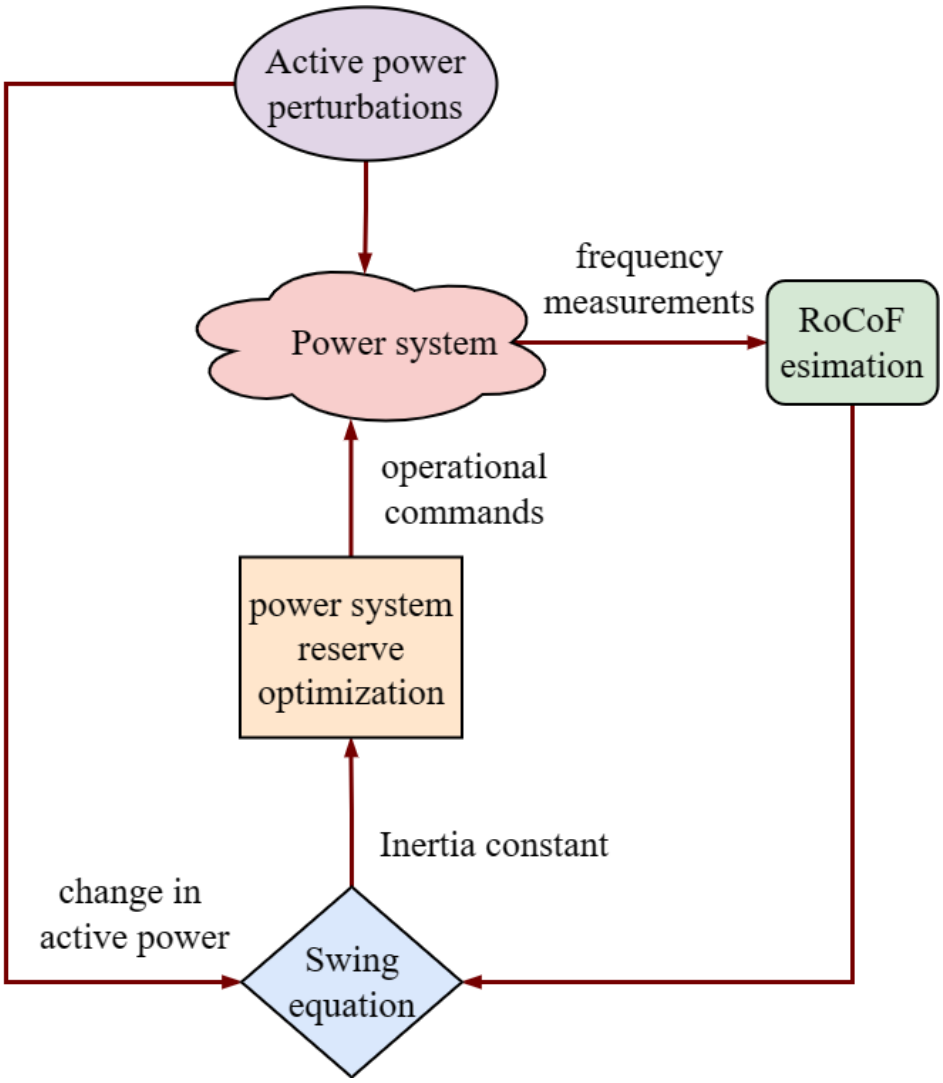

Figure 5.3: *Procedures for SDB based inertia estimation methods in power systems*

LDB methods in a sense of calculating the change in the active power that should be used for the inertia estimation.

5.2.2 Statistical methods

The challenges and difficulties of implementing online inertia estimation from disturbance based techniques, led [181] to propose a statistical method for inertia estimation in the Nordic power systems. The method involves identifying the number of SGs that are committed online, which is achieved by monitoring the status of their (SGs) grid connected circuit breakers (CB). This is easily achieved by using supervisory control and data acquisition (SCADA) system. Once the number of the online committed SG is evaluated, the total inertia constant of the system is evaluated as weighted mean of inertia

constants as given in (5.4). This methodology provides continuously online monitoring of the system's inertia.

The statistical method is simple, straight forward and easily implementable. It has been successfully implemented in the Nordic [181] and in the GB power systems [97]. However, the method can results into significant errors particularly in a system with high penetration of renewables. *This is because, the method considers only inertia from the SGs [182]. Therefore, with the current trend towards synthetic inertia (VSGs), this method yield unsatisfactory inertia estimate*. Moreover, information of the ratings of the generating units in its totality may not be available to the PSO [177].

5.2.3 Indirect swing equation based methods

Indirect swing equation based methods refers to the methods that involve identification of the power system models from the WAMS–data, and extracting inertia from the identified models. The fitted model (to the obtained data through WAMS) implicitly contain inertia as one of its parameters. Therefore, with the prior knowledge of the frequency response of a power system as quantified by the swing equation–*appropriate parameter estimation technique* can be used to extract the values of inertia constant. In this approach, methods can be categorized into groups basing on the type of fitted model (model structure), inertia extraction method and or system excitation methods. The latter technique is used in this research work where the methods are classified into *perturbations-model based methods and probing signals-model based methods*.

Perturbations-model based methods

In this approach, the system is excited by applying small active power perturbations which do not interfere with the operating conditions of the system. From the measurements of the excited system, a dynamic model which implicitly contains inertia is obtained. Inertia constant of the system is then extracted from the fitted dynamic model. This allows inertia to be estimated from the WAMS-data. Cao et al. [183] obtained a probabilistic model from the *historical events* of the inertia variations and frequency variations. The model is trained offline to predict inertia variations based on the frequency variations. Following training, the model is deployed online to estimate inertia. The system inertia is estimated as a summation of the last observed inertia value and the inertia variations

obtained from the trained model. This approach requires the knowledge of the current value of the inertia constant, which was obtained by using the *statistical method*. The use of the statistical methods can results in a serious errors as detailed in subsection 5.2.2. Moreover, the method fails to estimate inertia during large disturbances as they were not incorporated in the training data set. Furthermore, the method is computationally expensive and requires a large amount of data for training.

On the other hand, in [14, 24, 35–37] small perturbations of the active power are used during *normal power systems operations* to excite the frequency variations in the system. By using PMU, the acquire measurements are then taken. These are used in system identification process to fit a model and extract inertia values. In [35] an autoregressive moving average exogenous (ARMAX) model is fitted on the measured data. The ARMAX model is then converted to a transfer function (TF) for inertia extraction. The obtained TF is of higher orders, and therefore is reduced to lower orders and the impulse function is used to extract the inertia values. In [14] and [24] the TFs are obtained from the measurements and their corresponding inertias are extracted from the reduced TF by working out their corresponding gains. While, in [36] inertia constant is obtained from the TF by using a unit impulse response. Contrary to the latter methods, in [37] the reduced TF is converted to state space model and inertia is extracted from the eigenvalues of its corresponding dynamic matrix. These methods are beneficial in estimating inertia from ambient data measurements.

Figure 5.4 provides the general procedures for the inertia estimation process by using the perturbation–model based estimation methods. These methods, however, are computationally burdensome and can introduce significant time delays which hinder their applicability particularly for the adaptive protection schemes. This is due to the resulting higher order TF which requires a technique for its reduction to a lower order TF and a corresponding technique for extracting inertia constant. Hence, this results in the cumulative errors [183] which lower the accuracy of the inertia estimate.

Probing signals–model based methods

These are the methods which involve injection of a small signal (probing signals) for exciting power-frequency dynamics in the power system. Following system excitation, the input–probing signals and output–measured responses are used to identify the dy-

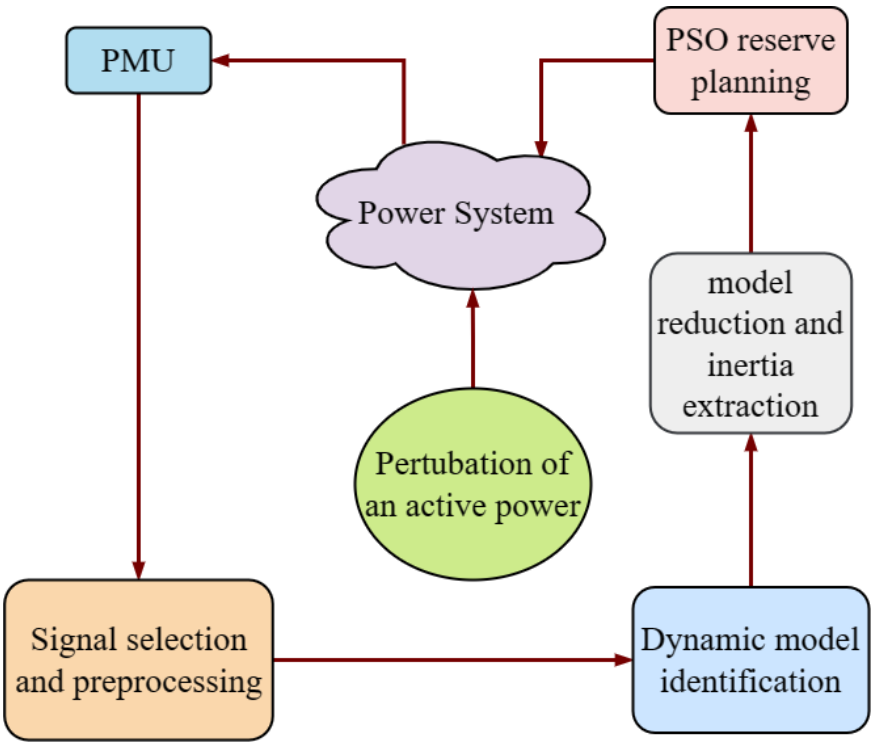

Figure 5.4: *General procedures for perturbation based inertia estimation*

namic model of the power system and then, inertia is extracted from the identified model. Contrary to the perturbation model based methods, in this approach the exciting signals need not to be a perturb of an active power, for example in [184] the power-frequency dynamics were invoked by the injection of the voltage signals. Moreover, these methods involve grey box modelling which is contrary to the black box modelling approaches which were deployed in the perturbation–model based methods. Hence, a known order model is fitted to the input-output data. The method is deployed in [185] for the online identification of a dynamic model of the power system, where a well designed multi-sine signals are used as probing signals. A similar approach is used in [184] where a TF is identified from the power-frequency data resulting after injection of the probing signals. In this approach, the probing signals are the voltage multi-sine signals that are injected to a bus of a power system by the power electronic devices. The measured responses and input probing signals are then deployed for the system identification, where two TFs are identified which are simplified to obtain a swing equation. Inertia constant is then directly extracted from the obtained swing equation.

On the other hand, in [186] a dynamic model of a SG is identified from the online

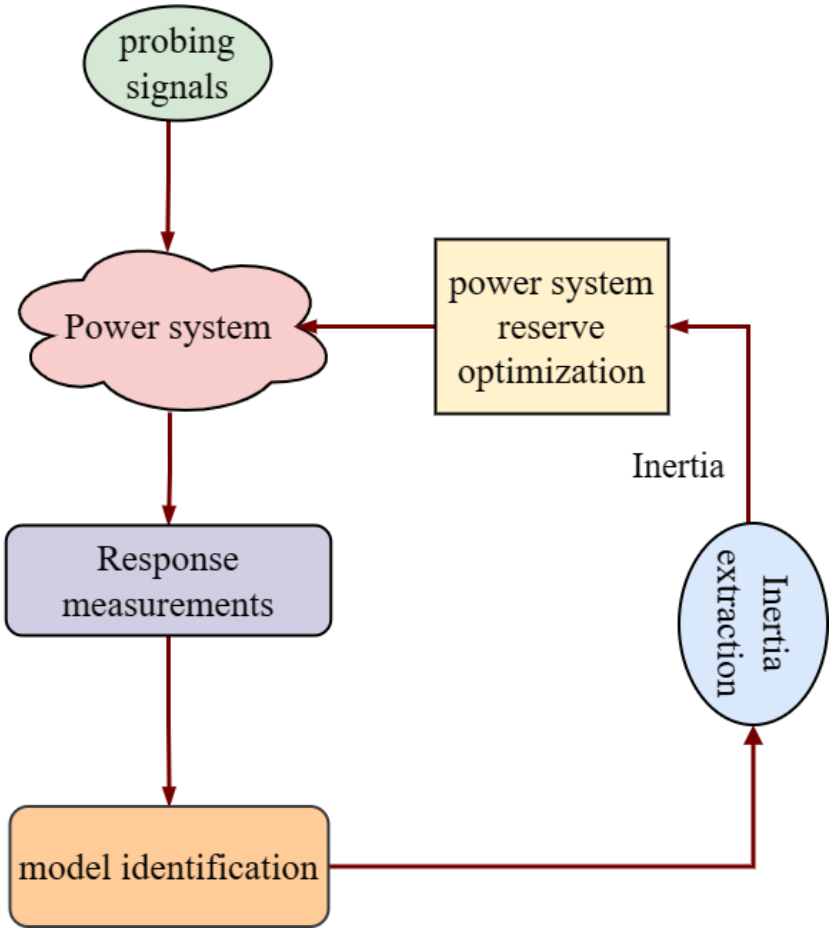

Figure 5.5: *Probing signals-modal based power system's inertia constant estimation*

measurements of the power and voltage. The method uses field voltage of the generator as the probing signals. These exciting signals are measured together with the voltage and active power which are the output responses. A nonlinear third order TF is then fitted to these measurements, and quantification of the SG parameters follows. This method is suitable for the inertia estimation in the system were SGs are the dominant generating units.

Fitting of the known model structure is advantageous in easiness of the quantification of the values of the inertia constants over the black box modelling approaches. However, the approach is intrusive and hence, threaten security of the power system particularly in a low inertia scenario which is characterized by the high systems' oscillations. Moreover, selection of the bus for injection of the probing signals is very challenging and hence, this hinders practical implementation of the methodology.

Penetration of the inertia-less RES generation into power systems results in a low time–varying inertia which exposes the system into the risks of the frequency instability.

Therefore, in circumventing this problem inertia of the power system must be known for optimization of the available system resources and for developing adaptive protection schemes. From the literature survey above it can be observed that most of the proposed inertia estimation methods discussed are disturbance based, offline and with a limited accuracy, which hinders their applicability in systems with high penetration of renewables. Moreover, some of the online inertia estimation methods discussed are intrusive to the system and they are based on post events which limits their application for the adaptive protection scheme. Therefore, there is still a need for researches on developing a suitable online stochastic inertia estimation for inertia-adaptive protection of the power system with high penetration of REs. This chapter therefore, proposes a neural network based method as a way forward for the online estimation of the inertia of a power system with high penetration of RE-generations. To obtain system inertia, the method uses as a simple multilayer perceptron (MLP) neural network supplied with RoCoF and inertia response active power as discussed in Section 5.3 which follows. The efficacy of the proposed methodology is validated by using the New England power system in a strong and weak grid scenarios. That is, under 0% penetration of RES and with variable percentage of RES as presented in Section 5.4. The method is non-intrusive to system and explicitly extracts inertia. Hence, it has a potential to be utilized for the adaptive protection schemes such as inertia adaptive VSGs.

5.3 A neural network–based online estimation of the stochastic inertia in a power system

In power systems, frequency excursions depend on the magnitude of disturbances (power changes) and the system's inertia. In low-inertia power systems dominated by renewable energy sources (RES), even small power changes can induce significant frequency oscillations. The intermittent nature of RES, combined with the stochastic behavior of loads, leads to power variability that excites the system, causing frequency deviations. With the widespread deployment of Phasor Measurement Units (PMUs) within Wide Area Measurement Systems (WAMS), it is now possible to capture frequency profiles, Rate of Change of Frequency (RoCoF), and corresponding power changes in real time. These data can be used to construct models for inertia estimation.

However, traditional data-driven approaches often fall short in providing the adaptability and robustness required for protective measures in low-inertia systems. To address these limitations, this study employs an artificial neural network (ANN)-based method. ANNs are particularly well-suited for this application due to their proven capability to approximate complex, nonlinear relationships between input and output data with high accuracy [105]. This makes ANN methods a superior choice for capturing the intricate dynamics of low-inertia systems and enabling adaptive inertia protection strategies. The proposed methodology entails three stages: *data acquisition, ANN model training and validation, and deployment of the ANN model for online inertia estimation in the power system*.

5.3.1 Data acquisition

The first stage involves identification of the right system variables that can be used for training the ANN model. As stated earlier, frequency excursions in the system depend on the size of disturbance and the system's inertia. Therefore, as portrayed in (5.7), the data of interests for training the ANN model are *RoCoF, size of the perturbation/disturbance and inertia constant*. Thus to obtain the required data sets, a small active power perturbation is set up as shown in Fig. 5.6 for a known value of the inertia constant. In this particular case, inertia is known through a lower bound method. Then, the corresponding frequency response is measured and RoCoF is estimated. This is done by either curve fitting approach from the frequency measurement or by averaging the RoCoFs measured from the PMUs within a window of 2 s following an active power perturbation. Exclusion of the data beyond the first 2 s is important for making sure that the *governor's response is excluded in RoCoF estimation*. The obtained RoCoF, its corresponding inertia constant and the active power variation are then stored. This process repeats until sufficient amount of data for training is captured. These data must sufficiently capture the necessary dynamics in the system. That is, using a lower bound method, the maximum and minimum inertia of the system can be known. For example, In GB inertia of the system has declined from 9 s in 2008 to 3 s 2020 [24], and is expected to further decline to 1.8 s by the end of 2025 [25]. This anticipation is established using a lower bound method. Hence, inertia constants are randomly changed within these bounds to sufficiently represent the systems' dynamics. The obtained data are then vectorized for

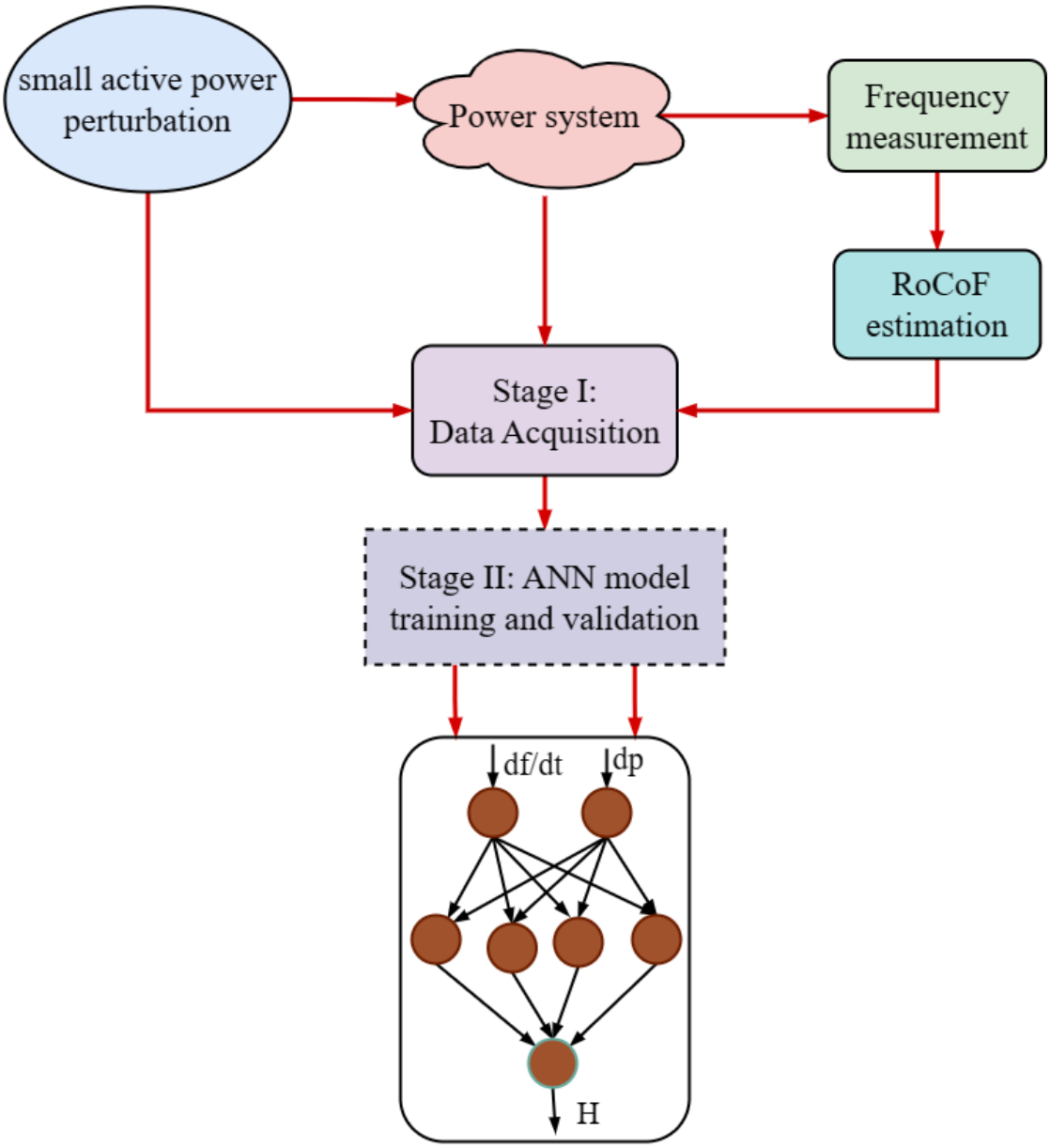

Figure 5.6: *Conceptualization diagram for stage I and II*

model training and validation purposes. This is done as

$$X_1 = [\Delta P_1, \Delta P_2, ...\Delta P_n], \tag{5.8}$$

$$X_2 = [\Delta \frac{df}{dt}_1, \Delta \frac{df}{dt}_2, ...\Delta \frac{df}{dt}_n], \tag{5.9}$$

$$Y_1 = [H_1, H_2, ...H_n]. \tag{5.10}$$

where X_1 and X_2 are the input data, representing change in active power and their corresponding RoCoFs–respectively, to the ANN model; and Y_1 is the inertia constant available at each change of the active power.

5.3.2 Model training and validation

There are numerous ANN models such that the choice for a particular model depends on the nature of the acquired data set. In this case, X_1, X_2 and Y_1 are static/same under the same repeatable conditions, therefore, *forward ANN is chosen*. Structurally, forward ANN is composed of the input layer, hidden layer and output layer. Based on the acquired data, it is observed that the input layer should be composed of two neurons, while the output layer is composed of one neural. The choice of neurons for the hidden layer is selected using the trial and error method. It should be noted that too many neurons can result in over-fitting while a limited number of neurons fails to capture the nonlinear dynamics between our variables of interest. Therefore, in this research work, 20 neurons were deemed optimal for the hidden error.

In training, the biasing weights were updated based on the mean square error (MSE). That is, the average squared differences between the predicted $H_{n_{predicted}}$ and the targeted $H_{n_{actual}}$ which is

$$MSE = \frac{1}{N}\sum_{n=1}^{N}\left(\frac{H_{n_{actual}} - H_{n_{predicted}}}{H_{n_{actual}}}\right)^2. \tag{5.11}$$

Since the penetration of RE generations marks the increased non-linearity in the system, then sigmoid functions were used in the hidden layer while recti-linear activation function was used for the output layer. Finally, Levenberg-Marquardt backpropagation was used for training the ANN model in MATLAB/Simulink environment. 70% of the data were used for training, 15% for testing and the last 15% for model validation. Figure 5.7 shows the errors between the predicted inertia values and the actual inertia values. It is verified that for both training, validation and testing data most of the errors are near to zero. This verifies our model for online deployment.

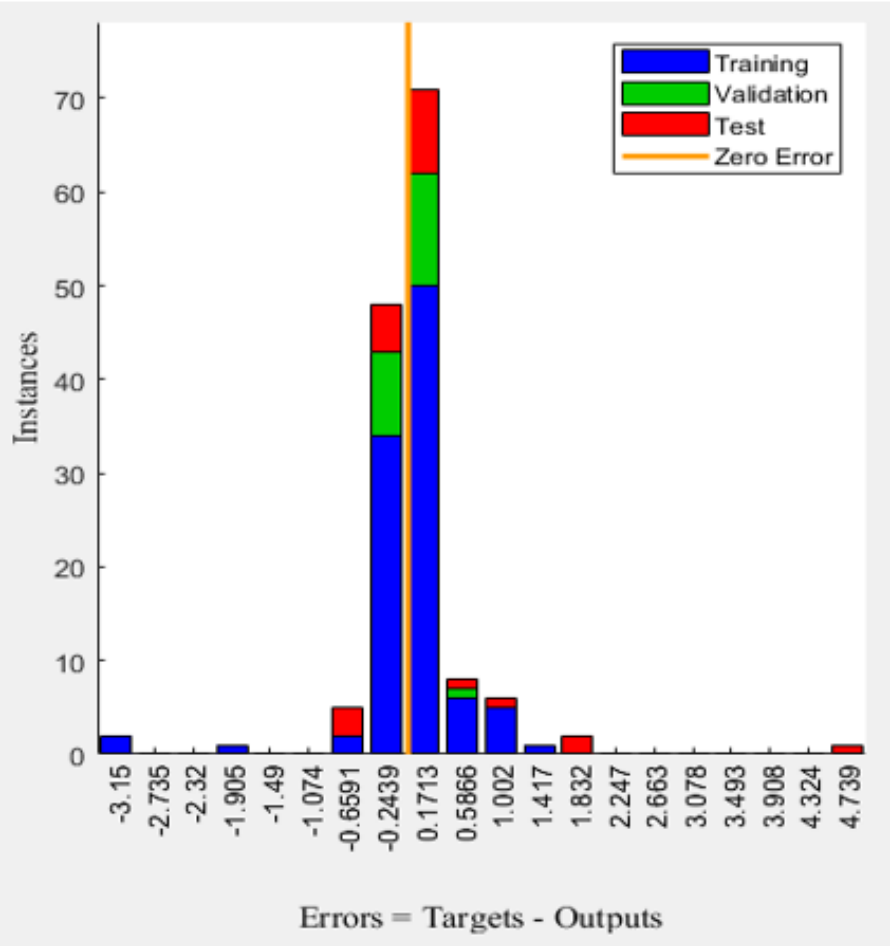

Figure 5.7: *Errors between targets and actual inertia constants during training and ANN model validation*

5.3.3 Online deployment of the ANN trained model

Figure. 5.8 summarizes the online deployment of the trained ANN model for the inertia estimation. The model takes advantage of the stochasticity of both the demand and supply to set up active power perturbations in the system. Based on the change in active power during both ambient and transient conditions, the frequency response can be measured using PMUs. Then, RoCoF can be estimated using the curve fitting approach or by averaging the measured RoCoFs from the PMUs in the appropriate time frame. Finally, the estimated RoCoF and active power variations can be presented to the trained ANN and explicitly inertia constant can be estimated.

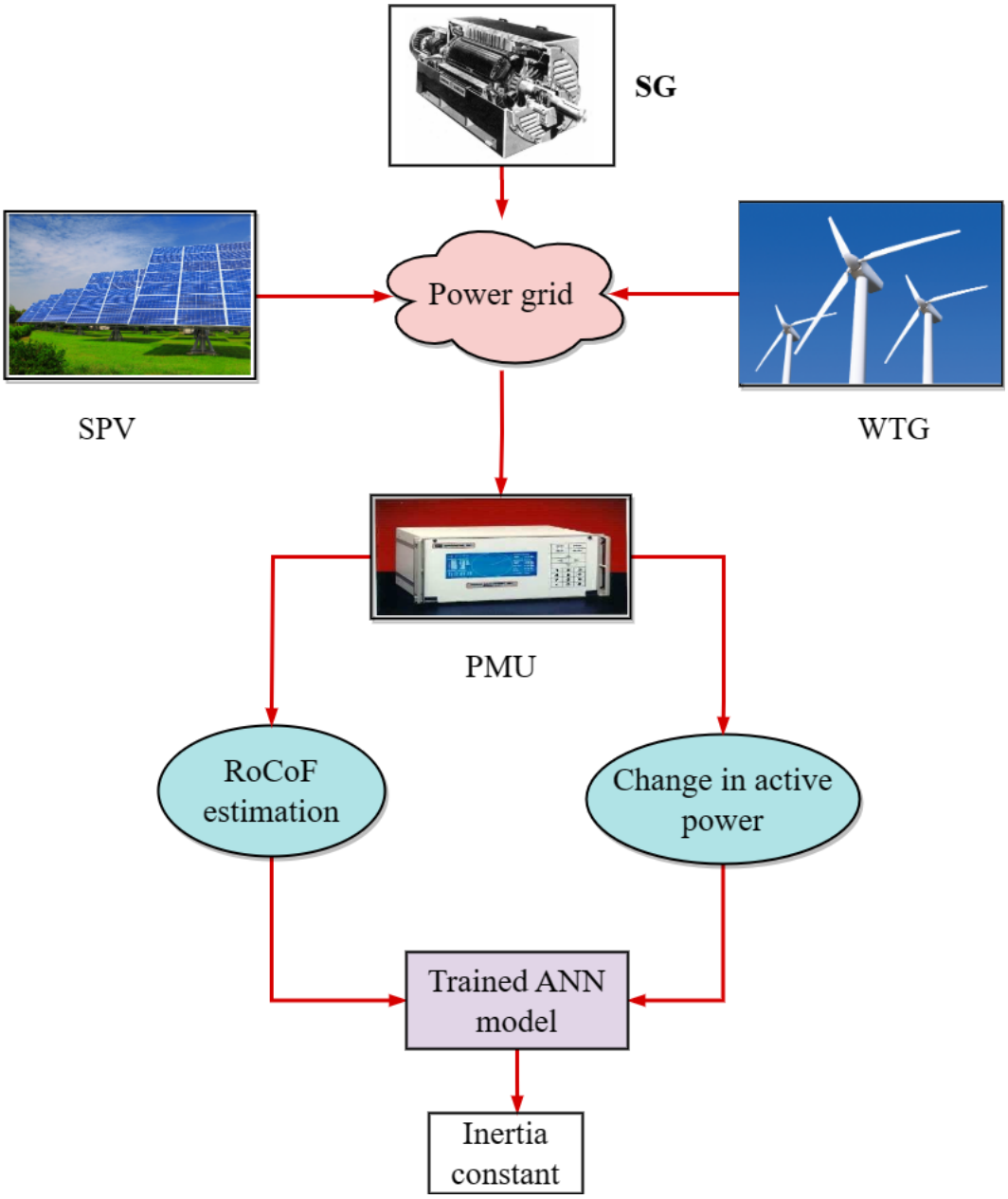

Figure 5.8: *Online ANN based power system's inertia estimation*

5.3.4 Performance evaluation of the methodology

In order to test the efficacy of the proposed method, a power system consisting of a composite mixture of SGs, SPV and WTG is developed in a MATLAB/Simulink environment as shown in Fig. 5.9. The SPV and WTG represent RE sources which are interfaced by the voltage source inverter (VSI). This is because, these are the fastest in growing RE sources as detailed in chapter 1. The dynamics of such power system is represented by

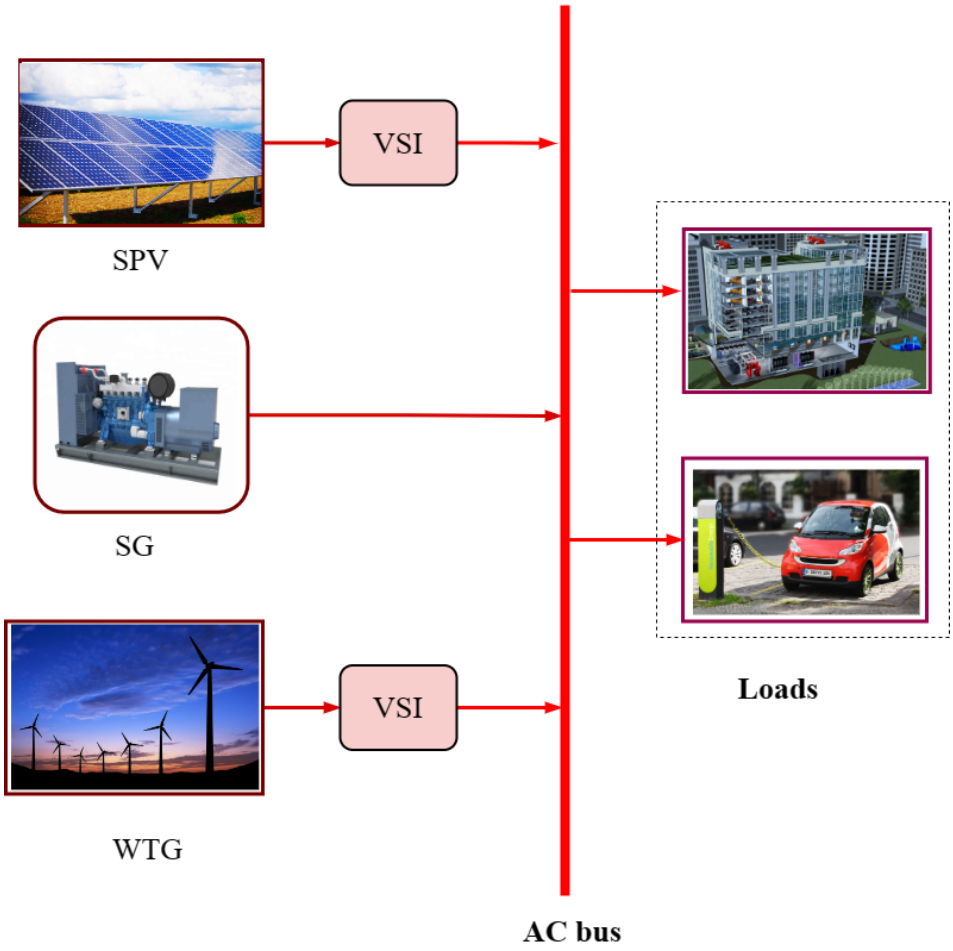

Figure 5.9: *Deployed LFC model for inertia estimation studies*

$$2H\frac{df}{dt} = \Delta P_m(t) - \Delta P_e(t) + \Delta P_{SPV}(t) + \Delta P_{WTG}(t) \tag{5.12}$$

where $P_m(t)$ is the change in mechanical power input to the SG, $\Delta P_e(t)$ change in the electrical power output of the SG, $\Delta P_{WTG}(t)$ is the change in power generated by the WTG system and $\Delta P_{SPV}(t)$ is the change in the power generated by the SPV system.

Frequency control in the modeled power system is achieved using SGs. That is inertia control and primary frequency control. The latter is achieved by using droop controller while secondary control has been implemented by using proportional–integral (PI) controller. The power from the SPV and WTG are aggregated as inertia-less and they account for a decrease of inertia. Then, known inertia values are randomly set between 1.8 s and 9 s, these values are based on the decline of inertia from 2008 to 2020 (9 s to 3 s) as presented in [24], and the expected decline in 2025 (3 s to 1.8 s) as presented in the GB power system [25]. In every power system, the maximum size of the sudden

increase in load is known. Therefore, small known perturbations representing active power change are set and their responses are measured. From the measured responses, RoCoF is estimated using fifth order polynomial–curve fitting approach. To evaluate the performance of the trained network, known inertia values under different penetration of RE generations is set and the ability of the ANN to find these values is validated. The set values of inertia constant were 2 s, 3 s and 5 s representing the expected decline of inertia in GB.

A known inertia value of 2 s is set in the model, and a small micro-perturbation in the ambient condition is deployed to set up dynamics in the system. RoCoF is determined which is fed to the ANN model and inertia is estimated. In this test, the estimated inertia value was found to be 1.89 s. To further validate the proposed method, inertia value is changed to 3s and a small perturbation is injected into the system. Following the similar procedures as when the inertia value was 2 s, the estimated inertia value is found to be 3.09 s. Moreover, the system is tested under transient conditions which presumes a sudden increase of a major portion of the load in the system. During the scenario inertia constant of the system was set at 5 s and the corresponding estimated value using the proposed method is found to be 5.1 s. Therefore, this validates the efficacy of the

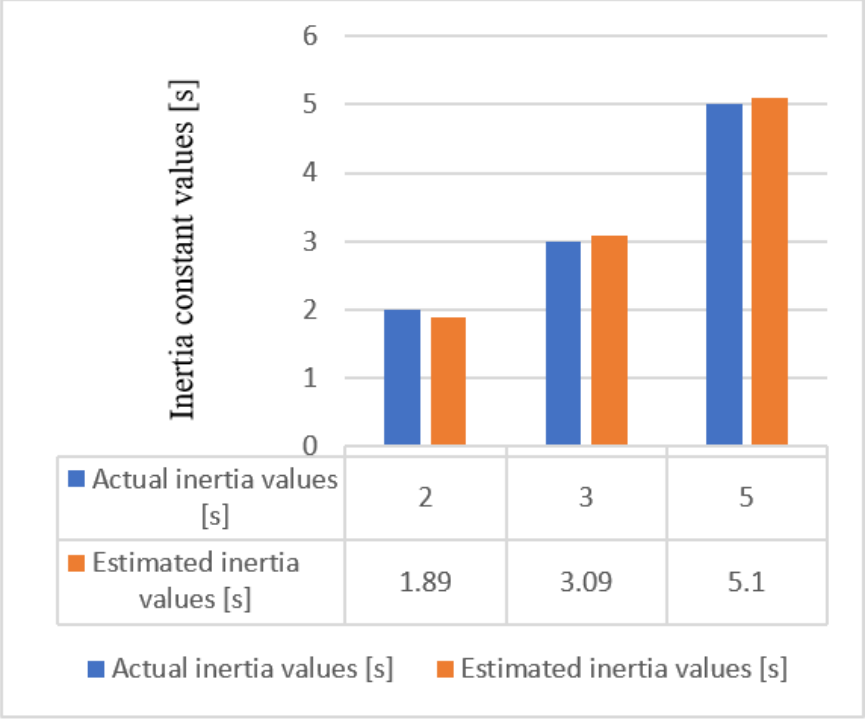

Figure 5.10: *Comparison of the estimated and actual inertia values*

system in estimating the inertia of the power system during both ambient and transient

conditions. Figure 5.10 provides comparison of the actual and estimated inertia values as detailed in the given three cases in this section.

5.4 Performance validation of the methodology: A case study of the New England power system

The New England power system, also refereed to as IEEE bus 39, is an interconnected power system which is constituted by 19 loads, 12 transformers and 10 SGs. The latter include a different mix of prime movers such as steam, hydro and nuclear. Moreover, the system can be modified by replacing the SGs RES generators such as SPV and WTG. Furthermore, the system is well documented and exhibits characteristics very close to a real power system. Hence, it is a suitable candidate for inertia estimation studies. Figure 5.11 provides a simplified single line diagram of the IEEE bus39.

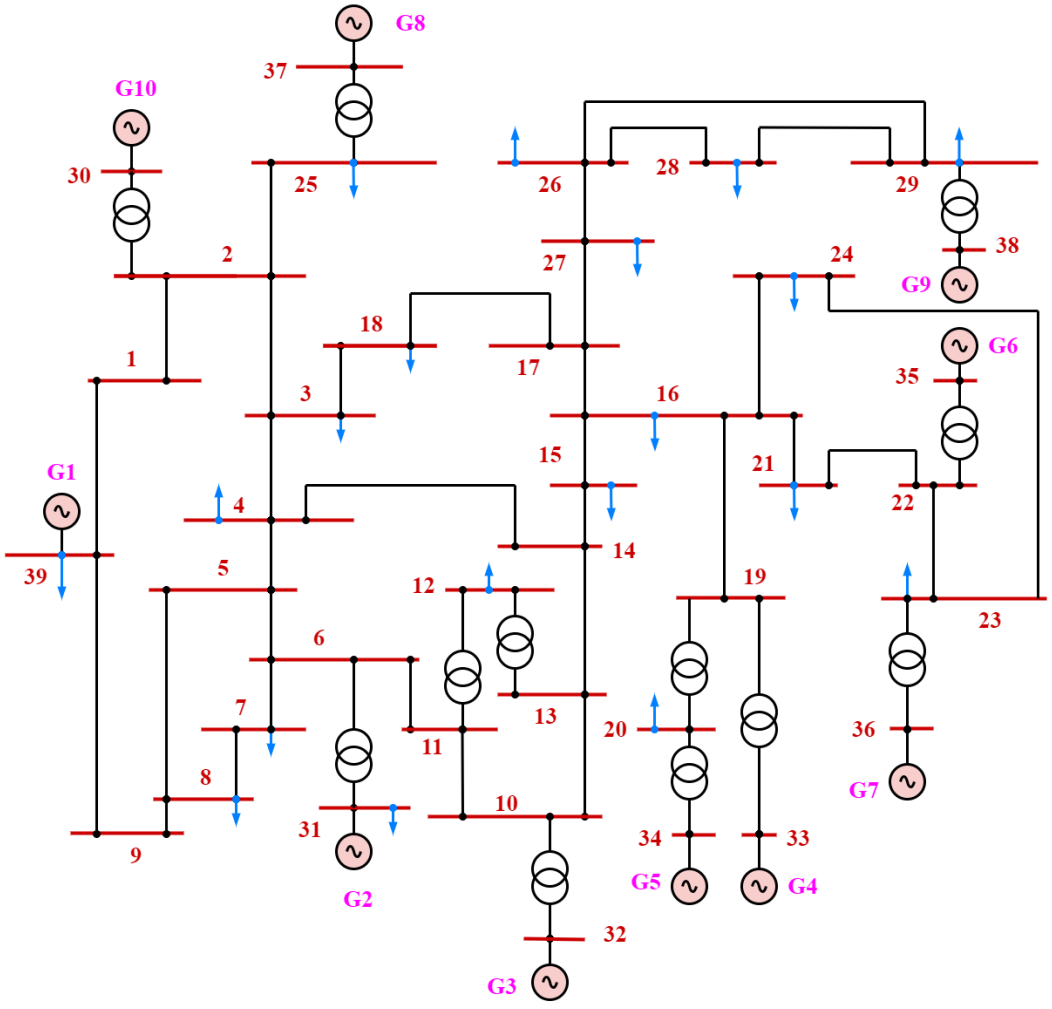

Figure 5.11: *The New England power system*

5.4.1 Case I: Performance verification under strong grid with no RES generators

The first step is to verify the applicability of the proposed methodology in a strong grid without RES generators. A typical New England power system, as shown in Fig. 5.11, is simulated under a step change in load demand. Inertia estimation is then performed for each synchronous generator (SG) and for the aggregated system. The former values are compared with the known inertia values of the respective generators, while the latter is compared with an aggregated inertia estimate of the system. This estimate is calculated using (5.4), which utilizes the known inertia values of the synchronous generators (SGs) and their respective apparent power ratings.

Simulations are performed under a DigSILENT PowerFactory 15.1 software. Table 5.1 provides the parameters SGs and loads at each respective load bus in the New England Power system as given in the DigSILENT PowerFactory 15.1. It is imperative

Table 5.1: *Generators' parameters*

Bus No.	Generator	MVA ratings	Inertia constant (s)
39	G1	10000	5
31	G2	700	4.329
32	G3	800	4.475
33	G4	800	3.575
34	G5	300	4.333
35	G6	800	4.35
36	G7	700	3.771
37	G8	700	3.45
38	G9	1000	3.47
30	G10	1000	4.25

to note that there are two parallel machines at bus 34, while the ratings provided in Table 5.1 are for only one generator. Taking this into account, the system inertia is calculated to be $H_{sys} = 7.833$ using (5.4) under the system base power of 10000 MVA. The system is simulated with the loads as given in Table 5.2. To set up frequency variations for inertia estimations, a 50% step change in load demand is set up at load bus No. 15. This is done in the 5th second while simulation is carried out for 15 s. Root mean square/Electromagnetic transient (RMS/EMT) type simulation is set to effectively capture frequency and power transients.To estimate the inertia of each SG, the active power (P) for each generator is measured along with the corresponding RoCoFs at their

Table 5.2: *Loadings*

Bus No.	P (MW)	Q (Mvar)	Bus No.	P (MW)	Q (Mvar)
39	1104	250	4	500	184
7	233.8	84	8	552	176
12	7.5	88	15	320	153
16	329	32.3	18	158	30
20	628	103	21	274	115
23	247.5	84.6	24	308.6	-92.2
25	224	47.2	26	139	17
27	281	75.5	28	206	27.6
29	283.5	26.9	31	9.2	4.6
3	322	2.4			

respective buses. Figure 5.12 provides P supplied by the generators and the power received at bus 15 (where a step change in power occurs). The latter is the sum of the

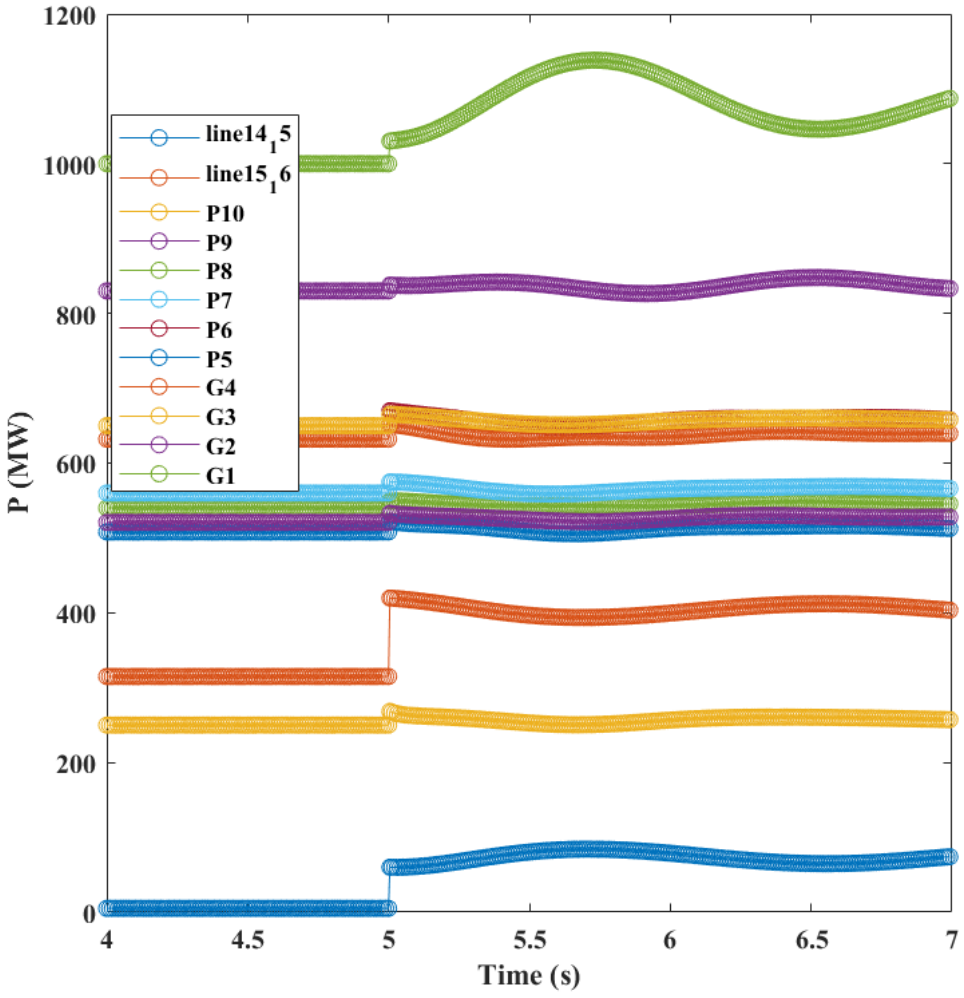

Figure 5.12: *Power supplied by the generators and lines (line 14_15 and line 15_16)*

power received from the line extending from bus 14 to 15 (named: line $14_1 15$) and from the line extending from bus 13 to 15 (named: line $15_1 16$). We have specifically taken a snapshot from the 4th to the 7th second to illustrate two points. First, it demonstrates that there was a consistent power supply before the load demand change at the 5th second. Second, the remaining 2 seconds provide a time-frame for estimation, ensuring that the data excludes the governor responses of the SGs. It is shown in Fig. 5.12 that there are power swings after 5th s. Hence, (5.13) provides the power supplied by the inertia response

$$\Delta P = P_{av}^{+} - P^{-} \tag{5.13}$$

where P^{-} refers to the power supplied by the generator or the line prior to the occurrence of the perturbation, the step change in power. While, P_{av} is the summation of powers within a window of 2 s after occurrence of the perturbation. Thus, Table 5.3 provides powers supplied by the generators due to the inertia responses and inertia response power received at bus 15, when a step change of 50% occurs in the latter bus. The per unit

Table 5.3: *Powers due to inertia response*

Item	ΔP (MW)	ΔP (in p.u)
G1	82.2	0.00822
G2	6.25	0.00893
G3	7.45	0.00931
G4	6.31	0.00789
G5	5.52	0.0184
G6	7.56	0.00945
G7	5.84	0.00834
G8	5.23	0.00747
G9	7.81	0.00781
G10	7.62	0.00762
Bus 15	157.4118	0.01574

values (p.u) in Table 5.3 are calculated with respect to each of the generator ratings, while for the load bus 15 system base value is used.

Figure 5.13 provides RoCoFs for each of generator buses and the load bus 15. Similarly, the RoCoFs are evaluated by averaging the values obtained from the PMU at a window of 2 s. Table 5.4provides results for this case. The RoCoFs and ΔP are then used for inertia estimation using the trained ANN model. Table 5.5 summarizes the results while Fig 5.14 provides its corresponding pictorial representation. It is shown that the methodology can estimate inertia's of both generators and the system (as an

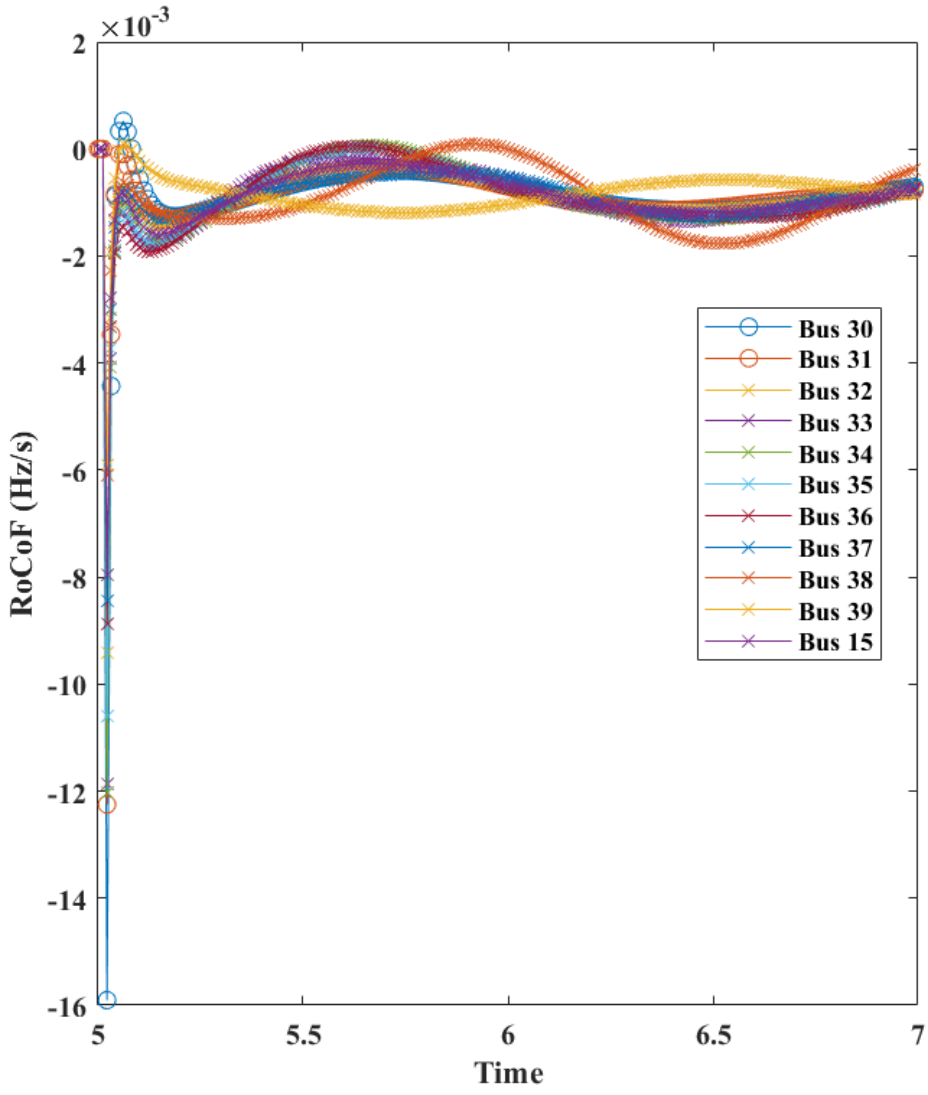

Figure 5.13: *RoCoFs at the generator buses and at load bus 15*

Table 5.4: *Average RoCoFs at the window of 2 s*

Bus No	RoCoF (Hz/s)
39	0.000831
31	0.0008905
32	0.0008929
33	0.0009168
34	0.0009224
35	0.0009205
36	0.0009192
37	0.0008936
38	0.0009246
30	0.0009016
Bus 15	0.0009501

aggregate at the point of perturbation) with an accuracy of more than 90%. In this case, power flows in the lines prior and after perturbation have been used to estimate the inertia power responses, for example in the load bus 15 the step change in load demand was 50% of the initial load (320 MW) which is 160 MW. The power evaluated through power flows technique, however, is 157.4118 MW. This introduces some errors in the estimation process.

Table 5.5: *Table of results*

Item	Actual H (s)	Actual H (s)	% Error
G1	5	4.95	1
G2	4.329	4.601	6.3
G3	4.475	4.710	5.25
G4	3.575	3.703	3.58
G5	4.333	4.687	8.17
G6	4.35	4.533	4.21
G7	3.771	3.637	3.55
G8	3.471	3.58	3.14
G9	3.45	3.223	6.58
G10	4.2	4.226	0.62
Bus 15	7.833	8.263	5.5

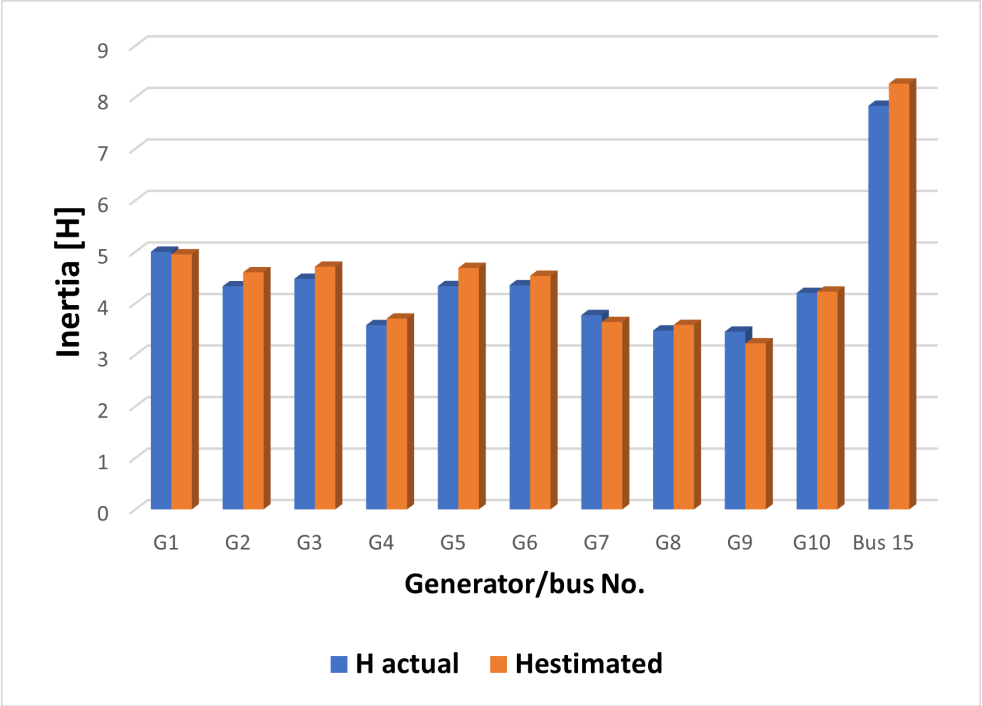

Figure 5.14: *Comparison of the estimated and actual inertia values*

5.4.2 Case II: Performance verification in the grid with RES generators

To test the validity of the proposed methodology under the weak grid, SGs in the New England power systems are replaced by the inertia-less RES generators as shown in Fig. 5.15. Two cases are simulated, that is, the RES penetration is increased from 0% as shown in case I (see 5.4.1) to 20% and 65%. To start with generators G2, G7, G9 and G10 are replaced by SPV generations. This marks the increased of RES penetration from 0% to 20%. A 50% step load change is set up in the load bus 15 in the 5th s similarly to the case I. Figure 5.16 provides the corresponding power flows in this case. It is shown in this figure that, the SPV systems supplies constant power. That is, the provide zero active power in response to the step change in the load demand; that is they are inertia-less. Similar procedures to case I, are then followed to estimate both RoCoF and the size of perturbation (ΔP). Table 5.6 provides estimated RoCoF, estimated ΔP, actual inertia and estimated inertia when RES penetrations varies from 0%, 20% and 65%. The latter case is obtained when the system in Fig. 5.11 is modified by replacing the SGs G1, G9 and G10 by SPV systems. The actual inertias in the Table 5.6 are obtained by using

Table 5.6: *Table of results*

% RES	RoCoF	ΔP	Actual H (s)	Estimated H (s)	% Error
0	0.000950	0.01574	7.833	8.263	5.5
20	0.0011	0.015643	6.5	7	7.7
65	0.0028	0.0146103	2.1	2.4	14.3

(5.4) under the system base power of 10,000 MVA. It can be observed that, the error in estimation increases as percentage RES increases. This is due to the increase in oscillations on the measured RoCoFs and active power inertia response which affects their estimates. That is, a 50% step load in change which corresponds to 0.016 (p.u) was set, an error of 1.62% in its estimation is incurred when there is 0% RES in the system while an error of 8.7% is incurred where there is 65% RES in the system. Despite, these errors, it is shown that the proposed methodology can estimate inertia under both weak and strong grid with a considerable accuracy (with an accuracy of more than 85%).

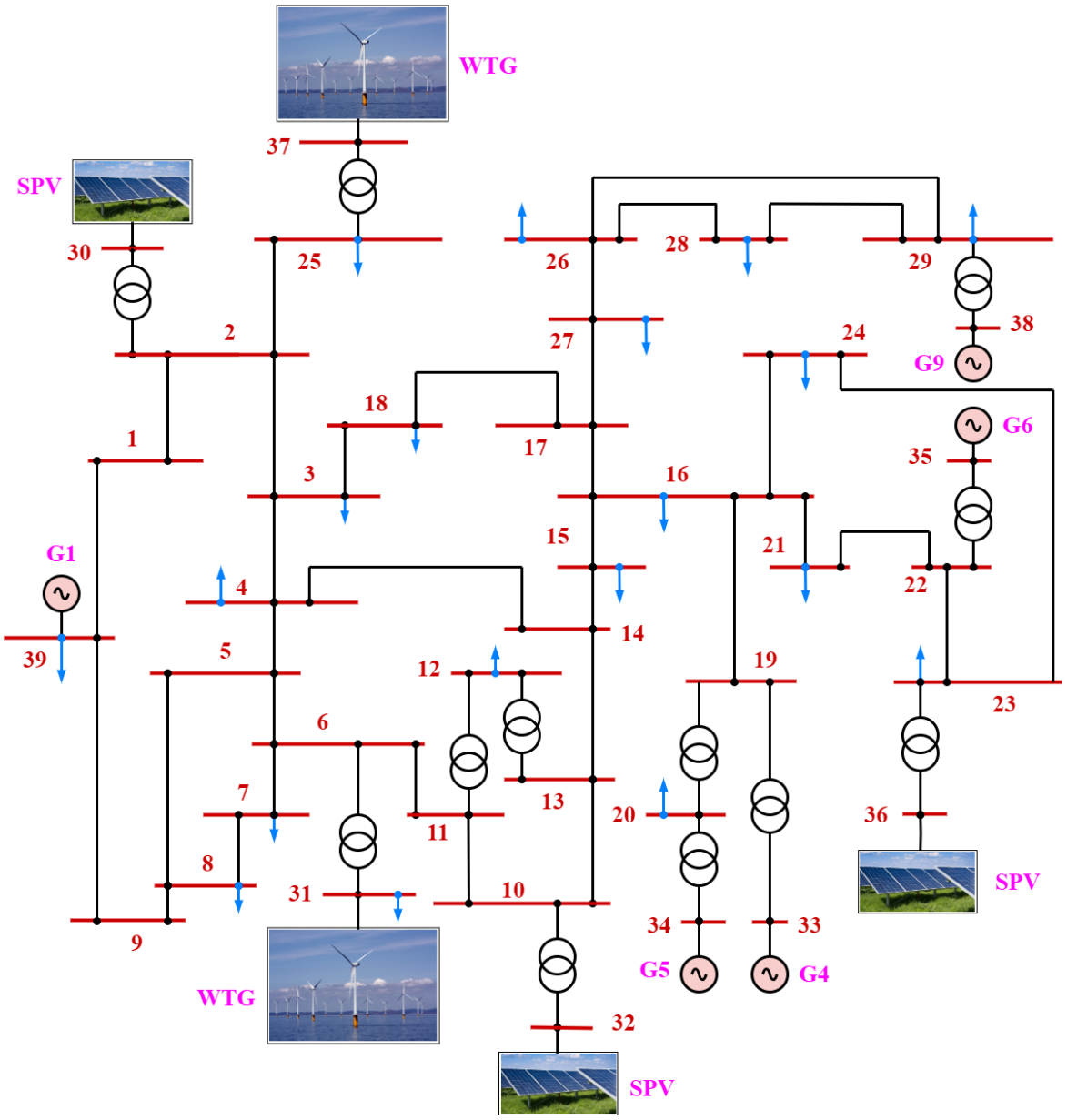

Figure 5.15: *The modified New England power system with RES generators*

5.5 Limitations of the proposed methodology

Despite the success of the proposed methodology as verified in Section 5.4, the following are the limitations of the proposed methodology;

- The training model assumes ideal data conditions, neglecting critical challenges such as measurement uncertainty and bandwidth limitations. In practical power systems, measurement data are often influenced by noise stemming from sensor inaccuracies, communication errors, and environmental disturbances [187]. Phasor Measurement Units (PMUs), which are widely used for system monitoring, are

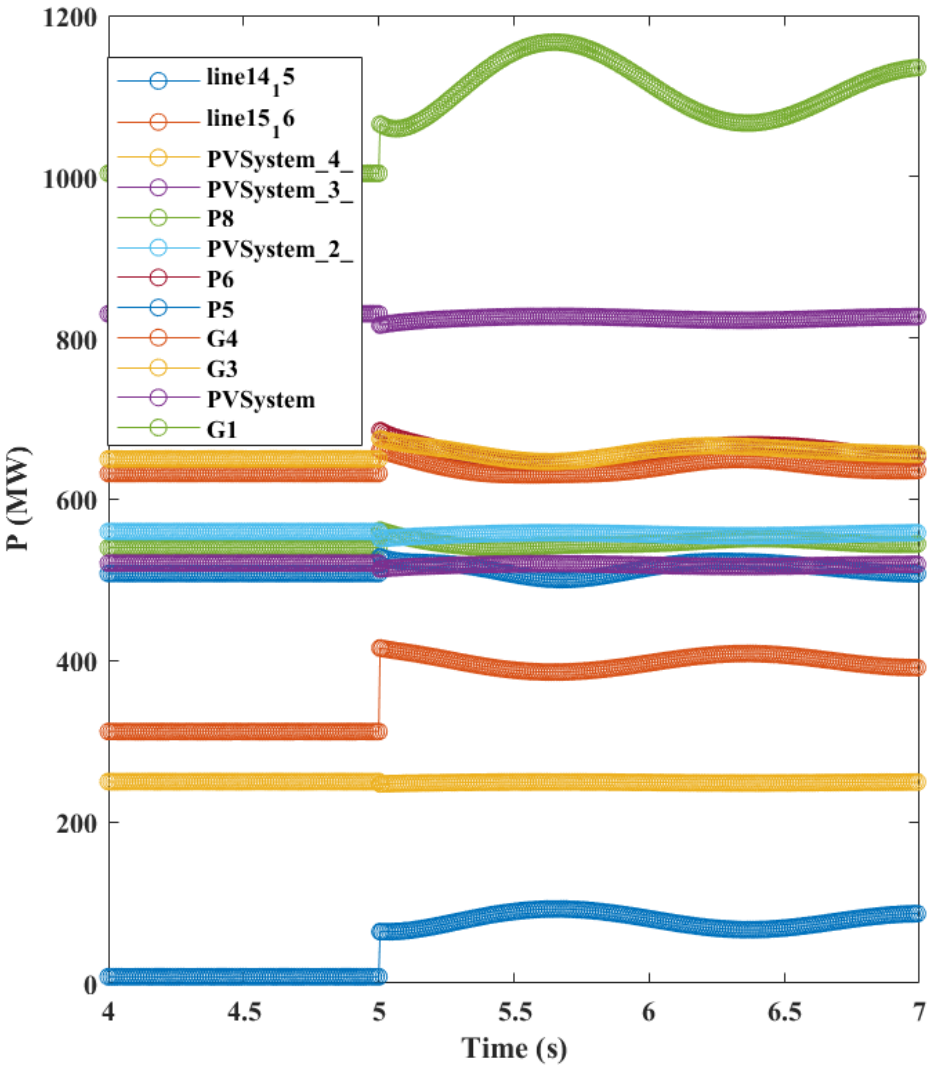

Figure 5.16: *Power supplied by the generators and lines (line 14_15 and line 15_16)*

particularly susceptible to these issues, as their high-resolution measurements can amplify the impact of noise and introduce additional variability. Furthermore, bandwidth constraints in measurement and communication devices can limit the resolution and responsiveness of the data, potentially degrading the model's performance in real-world scenarios. To address these limitations, future work should incorporate realistic noise profiles and account for bandwidth limitations in the training dataset, thereby improving the robustness and adaptability of the model for practical applications.

- Applying the trained model to large, interconnected power systems with diverse

inertia characteristics might require significant customization, reducing its scalability [188].

- The training model relies on simplified assumptions about system dynamics such as swing equation holds irrespective to the decline in inertia levels in a power system and deployment of fast frequency reserves, which may not hold true under all operational conditions.

5.6 Summary

This chapter presented a thorough literature review on inertia estimation methods in the power systems. Through which, the need for a new online inertia estimation method was identified particularly for designing adaptive inertia protection schemes. To address this challenge, a neural network based approach was presented. It was shown that the method can perform online estimation of the system's inertia under normal operating conditions. This was validated under both a strong grid and weak grid with considerable penetration of RES as shown in case 5.4.1 and case 5.4.2, respectively. The latter is achieved with an accuracy of more than 85% (see 5.6) while the former with more than 90% accuracy. In these cases inertia is explicitly estimated which is contrary to the system identification method in which inertia is implicitly contained in the identified model. To further improve accuracy of the proposed methodology, future works should consider improving accuracy of the estimate of the inertia response active power.

Chapter 6

Conclusion and future works

This chapter draws conclusions of this thesis and identifies the potential future works

6.1 Conclusion

This research work explored control methods for a virtual synchronous generator (VSG) connected to an electrical power system with high penetration of renewable energies (REs)–a weak grid. The results presented are significantly important in operation of the modern power systems as we are moving towards 100% RE–systems by 2050.

In this thesis—the challenges faced by power system operators (PSO) in operating such systems are thoroughly analysed, together with their counter measures. A snapshot of these is given by figures 2.3 and 2.4 respectively. *This lays a foundation block for exploring new operational measures of the modern power systems*. This is discussed in the chapter 2. Moreover, the chapter identifies the need for the virtual synchronous generators (VSGs) in operating the low inertia power systems.

Chapter 3, then, explores control methods for VSGs. In particular, when a VSG is connected to a weak grid, it faces with a PQ coupling problem. Thus, this chapter presented a new PQ decoupling technique using virtual impedance. Contrary to many literature's, as presented in Subsection 3.3.1, *we analytically establish the type and required magnitudes of the virtual impedance's as presented in Subsection 3.3.2*. To test the validity of the proposed scheme, a systematic design of the VSG–synchronverter is presented. In particular, *design of the virtual stator is provided in Subsection 3.4.2*. The chapter proceeds by providing implementation of the proposed scheme and simulation

results. It is verified that, the scheme can provide a decoupled PQ control with sudden changes in power requirements as shown in figure 3.14c. *This elucidates the ability of the scheme to adapt to the intermittent nature of RES and sudden changing in loads, which is important considering the variable nature of the weak grid*. This is achieved with simplicity in control of the VSG such that it is controlled as a conventional SG. That is P–control using a power angle and Q–control using internal voltage amplitude modulation. Moreover, the VSG operated using the proposed PQ decoupling technique is capable of supporting frequency regulation in the grid without inducing large transient grid currents during frequency variations, as elaborated in Subsections 3.6.4. This is aligns with the requirements that is set by power system operators through grid codes. That is, the RES must participate in provision of the frequency regulation in system. Hence, this provides a promise in practical deployment of the VSGs operating under the proposed scheme. *This, however assumes that, there is sufficient power reserve in the system. Quantification of the amount of the power reserves to be equipped with VSG is a new challenge*. This includes both, deciding how much curtailing from MPP is required to ensure sufficient reserve and or optimal sizing of the energy storage system to be incorporated with VSG so that it can participate in frequency regulation.

Moreover, despite the ability of the scheme to adapt to the changes of the X and R as presented in Subsection 3.3.1, it is imperative to have a robust method for determination of the grid impedance. In our study, the values of X and R are the inputs to the scheme. That means, any potential mismatches might results in control errors. Furthermore, the addition of the series capacitor lowers the VSG to grid interfacing impedance, hence high currents might result on occurrence of severe faults, such as severe voltage sags as shown in 4.11c for the VSG 1. This requires a fault ride through technique.

Chapter 4, thus, presented a new fault ride through technique using an active superconductor fault current limiter (ASFCL). *The design of the VSG incorporated with an ASFCL is as given by figure 4.4*. The ASFCL is a power electronic based unit whose controller was developed using a finite control set (FCS) model predictive control approach. This adds to the current trend of development of the MPC approaches in the field of power electronics. The FCS-MPC in this particular case–offers simplicity in design and implementation of the strategy. *By using ASFCL, a VSG can ride through faults while ensuring maximum power harvest as shown in Subsection 4.6.3*. This is achieve while

current is limited to its rated value as shown in figure 4.11c. Moreover, on the occurrence of the voltage sags, a VSG operated using virtual power circles based PQ decoupling scheme which is incorporated with ASFCL has *a better transient response* compared to the instantaneous limitation of the current (see figures 4.10c and 4.11c). This ensures that, the designed VSG adhere to the modified grid codes as given in figure 4.1. Hence, this enhances practicability of deployment of the designed VSG with ASFCL in the weak grid where occurrence of the voltages sags is inevitable. The simulation results presented in chapter considers symmetrical voltage sags. Therefore, it is imperative to explore the response of the designed system under unbalanced voltage sags. Moreover, the ASFCL involves addition of the inverter and flux coupling inductors. These add costs and complexity of the system.

Lastly, chapter 5 presented a comprehensive review on the state of the art inertia estimation methods–that are both in practice and from the researches. *This is crucial for establishment of new inertia estimation methods for the low inertia power systems*. Moreover, a neural network based inertia estimation method was presented as a way forward of estimating inertia a the low inertia power systems. The method is simple in design and tuning as it uses forward ANN models as shown in Subsection 5.3.2. The New England power system was used to validate the efficacy of the method. The system was modified to accommodate RES (with penetration level up to 65%) and it was shown that the method can estimate inertia under such scenario with an accuracy of more than 85% as shown in Table 5.6. The proposed methodology explicitly estimates inertia online. This can be used as an input to inertia adaptive protection schemes, as well as, when optimising resources for containing frequency deviations and limiting RoCoF for ensuring security of the system. This is a first attempt to estimate inertia without introducing any perturbations to the system. That is, inertia is estimated by just analysing power flows in the system and RoCoF measurements from the PMU. By considering the change in active power, the inertia response power was estimated by taking the difference between the power flow prior to the change and an average of the active power in a window of 2 s from the instant of change. This was shown (see Table 5.6) to accumulate errors as RES penetration levels increased. Hence, it imperative to improve its estimation method.

Conclusively, this research serves as a driving stone towards achieving a goal of 100%

REs systems with simplicity and easiness in RE–generators control while guaranteeing stability and security of the system.

6.2 Future works

On top of this research, as we transit towards 100% RE systems, the following are the potential research topics–future works, that can be considered towards achieving the targeted goal;

- *An improved double finite control set model predictive control based VSGs for the low inertia power system*—In chapter 3 a decoupled PQ control scheme for a VSG connected to a weak gird was presented. The VSG deploying the presented scheme was shown to easily achieve a decoupled PQ control similarly to the SG connected to the conventional strong grid. This removes the difficulties of the tuning of the VSGs such as–the synchronverter and provides easiness in its control. The designed VSG was further improved to provide low voltage ride through (LVRT) by additional of an auxiliary inverter with flux coupling inductors as presented in chapter 4. This was necessary since the VSG operated by the virtual power circles based PQ decoupling scheme is characterised by the total low interfacing impedance between the VSG–internal voltage (E) and the weak grid. This would have resulted in the high transient currents and the poor power transfer during low voltage ride through (LVRT). Hence, the use of the auxiliary inverter maximizes power transfer and suppresses transient currents.

  The incorporation of the auxiliary inverter in the grid connected VSG system *add costs and complexity of its control*. It results in a two power electronic inverters with two different principles of operation. The main inverter (VSG) is the voltage controlled inverter, while auxiliary inverter is the current controlled inverter. To minimise costs, the auxiliary controller can be replaced by another VSG. This VSG must therefore, be capable of being voltage and current controlled at the same time. This can easily be achieved using FCS-MPC. That is, one of the advantages of the FCS-MPC is multi objective optimization and its capability to handle multiple constraints using single objective function. Hence, the cost function for the latter VSG can be formulated to fast track both desired voltage and current. This means

that, there is a need–first to rejuvenate the VSG control using FCS-MPC, and then forming a coordinated control between two VSGs to aid each other during faults. This idea is supported by the fact that, in the grid connected system such as a solar photovoltaic (SPV) system–a number of solar panels are connected in series to form a solar strings. Hence each string can have its own inverter and every two of the inverters can be interconnected by the flux coupling inductors and thus, the concept of the double FCS-MPC based VSGs looks to capture attention. In developing such control method *there are many questions to be answered–which includes–how can they aid each other during faults—should one of the VSGs be islanded? can power transferred still be maximized during LVRT?* All these questions should be taken into consideration in the future works.

- *Inertia based optimal scheduling of the power sources in the low inertia power grid*–conventionally, inertia of the power system has not been considered in the system's unit commitment formulation. This has to change, however, with the influx penetration of REs. That is, its imperative for the inertia to be included in scheduling of the available power resources in the grid. This is important for the secure operation of the system. The fact that inertia has become a time-varying quantity threatens the system security particularly during low inertia periods. This is exacerbated by the decline in both power reserve and spinning reserve (SR). The availability of the SR ensured power balance in the system and hence–played a key role in the operation and control of the traditional power systems. Furthermore, the decline in the power reserve required for the frequency control in the low inertia power system is a result of the intermittent nature of REs and the hence–the desire to maximize power extraction from RE by operating at their maximum power point (MPP).

  The concept of the VSG shows potential in overcoming the challenge of the decline of the inertia, however in order to fully mimicking SG and ensuring frequency stability—there should be available power reserve that can be dispatched instantaneously analogous to the SG inertia response. To this end curtailing operation of the RE seems to be one of the options– *in this sense, however, the question of interest becomes how much curtailing from the MPP is required?*– knowing that, this kind of operation results in significant losses and hence can

maximize investment costs and unit cost of the electrical energy. Therefore, more research is required to answer this question, and one approach is to formulate a unit commitment problem in power system basing on inertia variation–that is–variation in power reserve in the system.

- *Experimentation*: the methodologies presented in this thesis are validated through comprehensive simulations, no experimental setups were conducted. The decision to focus solely on simulations was driven by several factors:

  - Resource constraints: Establishing a laboratory-scale experimental setup for testing low voltage ride-through (LVRT) in Virtual Synchronous Generators (VSGs) requires significant financial and infrastructural investments. These include acquiring hardware such as power converters, real-time simulators, and measurement equipment, which were beyond the scope of this work.
  - Focus on theoretical and simulation-based Validation: The primary objective of this work was to propose, develop, and validate novel control strategies and estimation methods. Simulations were deemed sufficient for proof-of-concept validation, ensuring the methodologies' robustness and applicability in practical scenarios.

  Future work should, therefore, prioritize experimental validation to bridge the gap between simulation and real-world applications. Setting up a laboratory-scale VSG system to test the presented methodologies would provide valuable insights into their performance under real operating conditions. Such experimentation would also facilitate the identification of implementation challenges and refine the proposed solutions for deployment in modern power systems.

Bibliography

[1] X. Luo, J. Wang, J. D. Wojcik, J. Wang, D. Li, M. Draganescu, Y. Li, and S. Miao, "Review of voltage and frequency grid code specifications for electrical energy storage applications," *Energies*, vol. 11, no. 5, p. 1070, 2018.

[2] H. R. Chamorro, A. D. Orjuela-Cañón, D. Ganger, M. Persson, F. Gonzalez-Longatt, L. Alvarado-Barrios, V. K. Sood, and W. Martinez, "Data-driven trajectory prediction of grid power frequency based on neural models," *Electronics*, vol. 10, no. 2, p. 151, 2021.

[3] Z. A. Obaid, L. M. Cipcigan, L. Abrahim, and M. T. Muhssin, "Frequency control of future power systems: reviewing and evaluating challenges and new control methods," *Journal of Modern Power Systems and Clean Energy*, vol. 7, no. 1, pp. 9–25, 2019.

[4] Q. Hong, M. Nedd, S. Norris, I. Abdulhadi, M. Karimi, V. Terzija, B. Marshall, K. Bell, and C. Booth, "Fast frequency response for effective frequency control in power systems with low inertia," *The Journal of Engineering*, vol. 2019, no. 16, pp. 1696–1702, 2019.

[5] M. Eremia and M. Shahidehpour, *Handbook of electrical power system dynamics: modeling, stability, and control*. John Wiley & Sons, 2013, vol. 92.

[6] S. C. Johnson, D. J. Papageorgiou, D. S. Mallapragada, T. A. Deetjen, J. D. Rhodes, and M. E. Webber, "Evaluating rotational inertia as a component of grid reliability with high penetrations of variable renewable energy," *Energy*, vol. 180, pp. 258–271, 2019.

[7] ENTSO-E, "A system operability framework document: Operating a low inertia system," 2020.

[8] R. Azizipanah-Abarghooee, M. Malekpour, M. Paolone, and V. Terzija, "A new approach to the online estimation of the loss of generation size in power systems," *IEEE Transactions on Power Systems*, vol. 34, no. 3, pp. 2103–2113, 2018.

[9] T. Amraee, M. G. Darebaghi, A. Soroudi, and A. Keane, "Probabilistic under frequency load shedding considering rocof relays of distributed generators," *IEEE Transactions on Power Systems*, vol. 33, no. 4, pp. 3587–3598, 2017.

[10] D. Das, *Electrica Power Systems*. New Age International Ltd, 2006.

[11] P. Gupta, R. Bhatia, and D. Jain, "Active rocof relay for islanding detection," *IEEE Transactions on Power Delivery*, vol. 32, no. 1, pp. 420–429, 2016.

[12] A. Adrees, J. Milanović, and P. Mancarella, "Effect of inertia heterogeneity on frequency dynamics of low-inertia power systems," *IET Generation, Transmission & Distribution*, vol. 13, no. 14, pp. 2951–2958, 2019.

[13] M. Rezkalla, M. Pertl, and M. Marinelli, "Electric power system inertia: Requirements, challenges and solutions," *Electrical Engineering*, vol. 100, no. 4, pp. 2677–2693, 2018.

[14] P. Makolo, R. Zamora, and T.-T. Lie, "Heuristic inertia estimation technique for power networks with high penetration of RES," in *2020 2nd International Conference on Smart Power & Internet Energy Systems (SPIES)*. IEEE, 2020, pp. 356–361.

[15] P. Tielens and D. Van Hertem, "The relevance of inertia in power systems," *Renewable and Sustainable Energy Reviews*, vol. 55, pp. 999–1009, 2016.

[16] V. Krakowski, E. Assoumou, V. Mazauric, and N. Maïzi, "Reprint of feasible path toward 40–100% renewable energy shares for power supply in france by 2050: A prospective analysis," *Applied energy*, vol. 184, pp. 1529–1550, 2016.

[17] I. Boie, C. Kost, S. Bohn, M. Agsten, P. Bretschneider, O. Snigovyi, M. Pudlik, M. Ragwitz, T. Schlegl, and D. Westermann, "Opportunities and challenges of

high renewable energy deployment and electricity exchange for north africa and europe–scenarios for power sector and transmission infrastructure in 2030 and 2050," *Renewable Energy*, vol. 87, pp. 130–144, 2016.

[18] L. Al-Ghussain, A. M. Abubaker, and A. D. Ahmad, "Superposition of renewable-energy supply from multiple sites maximizes demand-matching: Towards 100% renewable grids in 2050," *Applied Energy*, vol. 284, p. 116402, 2021.

[19] M. A. Basit, S. Dilshad, R. Badar, and S. M. Sami ur Rehman, "Limitations, challenges, and solution approaches in grid-connected renewable energy systems," *International Journal of Energy Research*, vol. 44, no. 6, pp. 4132–4162, 2020.

[20] IRENA, "Smart electrification with renewables: Driving the transformation of energy services," 2022.

[21] P. Makolo, R. Zamora, and T.-T. Lie, "The role of inertia for grid flexibility under high penetration of variable renewables-a review of challenges and solutions," *Renewable and Sustainable Energy Reviews*, vol. 147, p. 111223, 2021.

[22] S. Homan, N. Mac Dowell, and S. Brown, "Grid frequency volatility in future low inertia scenarios: Challenges and mitigation options," *Applied Energy*, vol. 290, p. 116723, 2021.

[23] H. T. Nguyen, G. Yang, A. H. Nielsen, and P. H. Jensen, "Challenges and research opportunities of frequency control in low inertia systems," in *E3S Web of Conferences*, vol. 115. EDP Sciences, 2019, p. 02001.

[24] P. Makolo, I. Oladeji, R. Zamora, and T.-T. Lie, "Data-driven inertia estimation based on frequency gradient for power systems with high penetration of renewable energy sources," *Electric Power Systems Research*, vol. 195, p. 107171, 2021.

[25] Q. Hong, M. A. U. Khan, C. Henderson, A. Egea-Àlvarez, D. Tzelepis, and C. Booth, "Addressing frequency control challenges in future low-inertia power systems: a great britain perspective," *Engineering*, vol. 7, no. 8, pp. 1057–1063, 2021.

[26] Nahid-Al-Masood, R. Yan, and T. K. Saha, "Cascading contingencies in low inertia power systems: Frequency response challenges and a potential solution," in *2017 IEEE Power Energy Society General Meeting*, 2017, pp. 1–5.

[27] A. Ulbig, T. S. Borsche, and G. Andersson, "Impact of low rotational inertia on power system stability and operation," *IFAC Proceedings Volumes*, vol. 47, no. 3, pp. 7290–7297, 2014.

[28] N. Holjevac, T. Baškarad, J. Daković, M. Krpan, M. Zidar, and I. Kuzle, "Challenges of high renewable energy sources integration in power systems—the case of croatia," *Energies*, vol. 14, no. 4, p. 1047, 2021.

[29] J. D. Boles, Y. Ma, L. M. Tolbert, and F. Wang, "Frequency support comparison for vanadium and lithium-ion besss using a converter-based grid emulator," in *2018 IEEE Applied Power Electronics Conference and Exposition (APEC)*. IEEE, 2018, pp. 623–630.

[30] D. Zografos and M. Ghandhari, "Estimation of power system inertia," in *2016 IEEE Power and Energy Society General Meeting (PESGM)*. IEEE, 2016, pp. 1–5.

[31] D. Zografos, M. Ghandhari, and R. Eriksson, "Power system inertia estimation: Utilization of frequency and voltage response after a disturbance," *Electric Power Systems Research*, vol. 161, pp. 52–60, 2018.

[32] D. Zografos and M. Ghandhari, "Power system inertia estimation by approaching load power change after a disturbance," in *2017 IEEE Power & Energy Society General Meeting*. IEEE, 2017, pp. 1–5.

[33] P. Wall, F. Gonzalez-Longatt, and V. Terzija, "Estimation of generator inertia available during a disturbance," in *2012 IEEE Power and Energy Society General Meeting*. IEEE, 2012, pp. 1–8.

[34] P. Wall and V. Terzija, "Simultaneous estimation of the time of disturbance and inertia in power systems," *IEEE Transactions on Power Delivery*, vol. 29, no. 4, pp. 2018–2031, 2014.

[35] K. Tuttelberg, J. Kilter, D. Wilson, and K. Uhlen, "Estimation of power system inertia from ambient wide area measurements," *IEEE Transactions on Power Systems*, vol. 33, no. 6, pp. 7249–7257, 2018.

[36] V. Sagar and S. K. Jain, "Estimation of power system inertia using system identification," in *2019 IEEE Innovative Smart Grid Technologies-Asia (ISGT Asia)*. IEEE, 2019, pp. 285–290.

[37] P. Makolo, R. Zamora, and T. Lie, "Online inertia estimation for power systems with high penetration of RES using recursive parameters estimation," *IET Renewable Power Generation*, 2021.

[38] H.-P. Beck and R. Hesse, "Virtual synchronous machine," in *2007 9th international conference on electrical power quality and utilisation*. IEEE, 2007, pp. 1–6.

[39] Q.-C. Zhong and G. Weiss, "Synchronverters: Inverters that mimic synchronous generators," *IEEE transactions on industrial electronics*, vol. 58, no. 4, pp. 1259–1267, 2010.

[40] Q.-C. Zhong, P.-L. Nguyen, Z. Ma, and W. Sheng, "Self-synchronized synchronverters: Inverters without a dedicated synchronization unit," *IEEE Transactions on power electronics*, vol. 29, no. 2, pp. 617–630, 2013.

[41] J. M. Ramirez, E. T. Montalvo, and C. I. Nuño, "Modelling, synchronisation, and implementation of the virtual synchronous generator: a study of its reactive power handling," *Electrical Engineering*, vol. 102, no. 3, pp. 1605–1619, 2020.

[42] K. Sakimoto, Y. Miura, and T. Ise, "Stabilization of a power system with a distributed generator by a virtual synchronous generator function," in *8th International Conference on Power Electronics-ECCE Asia*. IEEE, 2011, pp. 1498–1505.

[43] X. Hou, H. Han, C. Zhong, W. Yuan, M. Yi, and Y. Chen, "Improvement of transient stability in inverter-based AC microgrid via adaptive virtual inertia," in *2016 IEEE Energy Conversion Congress and Exposition (ECCE)*. IEEE, 2016, pp. 1–6.

[44] S. Kumaravel, V. Thomas, T. O'Donnel, and S. Ashok, "Transient frequency response improvement in microgrid using virtual synchronous machine," *Journal of The Institution of Engineers (India): Series B*, vol. 100, no. 4, pp. 371–377, 2019.

[45] N. Pogaku, M. Prodanovic, and T. C. Green, "Modeling, analysis and testing of autonomous operation of an inverter-based microgrid," *IEEE Transactions on power electronics*, vol. 22, no. 2, pp. 613–625, 2007.

[46] X. Hou, Y. Sun, X. Zhang, J. Lu, P. Wang, and J. M. Guerrero, "Improvement of frequency regulation in VSG-based AC microgrid via adaptive virtual inertia," *IEEE Transactions on Power Electronics*, vol. 35, no. 2, pp. 1589–1602, 2019.

[47] U. Tamrakar, D. Shrestha, M. Maharjan, B. P. Bhattarai, T. M. Hansen, and R. Tonkoski, "Virtual inertia: Current trends and future directions," *Applied Sciences*, vol. 7, no. 7, p. 654, 2017.

[48] F. Yu, C. Booth, and A. Dyśko, "Backup protection requirements in future low-inertia power systems," in *2016 51st International Universities Power Engineering Conference (UPEC)*. IEEE, 2016, pp. 1–6.

[49] NationalGridESO, "What is short circuit level," https://www.nationalgrideso.com/news/what-short-circuit-level, accessed: 2021-12.

[50] A. Asrari, M. Mustafa, M. Ansari, and J. Khazaei, "Impedance analysis of virtual synchronous generator-based vector controlled converters for weak ac grid integration," *IEEE Transactions on Sustainable Energy*, vol. 10, no. 3, pp. 1481–1490, 2019.

[51] T. Shintai, Y. Miura, and T. Ise, "Oscillation damping of a distributed generator using a virtual synchronous generator," *IEEE transactions on power delivery*, vol. 29, no. 2, pp. 668–676, 2014.

[52] B. Li, L. Zhou, X. Yu, C. Zheng, and J. Liu, "Improved power decoupling control strategy based on virtual synchronous generator," *IET Power Electronics*, vol. 10, no. 4, pp. 462–470, 2017.

[53] P. Zhang, H. Zhao, H. Cai, J. Shi, and X. He, "Power decoupling strategy based on 'virtual negative resistor'for inverters in low-voltage microgrids," *IET Power Electronics*, vol. 9, no. 5, pp. 1037–1044, 2016.

[54] M. A. Abusara, J. M. Guerrero, and S. M. Sharkh, "Line-interactive UPS for microgrids," *IEEE Transactions on Industrial Electronics*, vol. 61, no. 3, pp. 1292–1300, 2013.

[55] H. Pan, T. Wei, C. Deng, H. Long, and Y. Zhang, "A novel PQ control strategy for non phase-locked loop based on hilbert transform," in *2018 IEEE Energy Conversion Congress and Exposition (ECCE)*. IEEE, 2018, pp. 2676–2682.

[56] Y. Chen, J. Zhao, J. Wang, K. Qu, S. Ushiki, and M. Ohshima, "A decupled PQ control strategy of voltage-controlled inverters," in *2015 9th International Conference on Power Electronics and ECCE Asia (ICPE-ECCE Asia)*. IEEE, 2015, pp. 1374–1379.

[57] Y. Chen, J. Zhao, K. Qu, and F. Li, "PQ control of micro grid inverters with axial voltage regulators," *Journal of Power Electronics*, vol. 15, no. 6, pp. 1601–1608, 2015.

[58] J. Astrada and C. De Angelo, "Double virtual-impedance loop for inverters with repetitive and droop control in UPS applications," *Electric Power Systems Research*, vol. 204, p. 107680, 2022.

[59] D. Çelik and M. E. Meral, "A coordinated virtual impedance control scheme for three phase four leg inverters of electric vehicle to grid (V2G)," *Energy*, vol. 246, p. 123354, 2022.

[60] X. Lu, J. Wang, J. M. Guerrero, and D. Zhao, "Virtual-impedance-based fault current limiters for inverter dominated AC microgrids," *IEEE Transactions on Smart Grid*, vol. 9, no. 3, pp. 1599–1612, 2016.

[61] V. Natarajan and G. Weiss, "Synchronverters with better stability due to virtual inductors, virtual capacitors, and anti-windup," *IEEE Transactions on Industrial Electronics*, vol. 64, no. 7, pp. 5994–6004, 2017.

[62] P. Piya, M. Ebrahimi, M. Karimi-Ghartemani, and S. A. Khajehoddin, "Fault ride-through capability of voltage-controlled inverters," *IEEE Transactions on Industrial Electronics*, vol. 65, no. 10, pp. 7933–7943, 2018.

[63] M. A. Khan, A. Haque, and V. B. Kurukuru, "Dynamic voltage support for low-voltage ride-through operation in single-phase grid-connected photovoltaic systems," *IEEE Transactions on Power Electronics*, vol. 36, no. 10, pp. 12 102–12 111, 2021.

[64] K. Shi, H. Ye, P. Xu, D. Zhao, and L. Jiao, "Low-voltage ride through control strategy of virtual synchronous generator based on the analysis of excitation state," *IET Generation, Transmission & Distribution*, vol. 12, no. 9, pp. 2165–2172, 2018.

[65] S. Bagchi, D. Chatterjee, R. Bhaduri, and P. K. Biswas, "An improved low-voltage ride-through (LVRT) strategy for PV-based grid connected inverter using instantaneous power theory," *IET Generation, Transmission & Distribution*, vol. 15, no. 5, pp. 883–893, 2021.

[66] K. Shi, W. Song, P. Xu, R. Liu, Z. Fang, and Y. Ji, "Low-voltage ride-through control strategy for a virtual synchronous generator based on smooth switching," *IEEE Access*, vol. 6, pp. 2703–2711, 2017.

[67] L. Chen, Y. Tang, J. Shi, and Z. Sun, "Simulations and experimental analyses of the active superconducting fault current limiter," *Physica C: Superconductivity*, vol. 459, no. 1-2, pp. 27–32, 2007.

[68] L. Chen, C. Deng, F. Guo, Y. Tang, J. Shi, and L. Ren, "Reducing the fault current and overvoltage in a distribution system with distributed generation units through an active type SFCL," *IEEE Transactions on Applied Superconductivity*, vol. 24, no. 3, pp. 1–5, 2013.

[69] L. Chen, H. Chen, G. Li, X. Tian, Y. Xu, L. Ren, Y. Li, L. Zhu, and Y. Tang, "Coordination of SMES, SFCL and distributed generation units for micro-grid stability enhancement via wireless communications," *IEEE Access*, vol. 6, pp. 36 699–36 710, 2018.

[70] L. Chen, G. Li, H. Chen, M. Ding, X. Zhang, Y. Li, Y. Xu, L. Ren, and Y. Tang, "Investigation of a modified flux-coupling-type SFCL for low-voltage ride-through fulfillment of a virtual synchronous generator," *IEEE Transactions on Applied Superconductivity*, vol. 30, no. 4, pp. 1–6, 2020.

[71] P.Kundur, *Power system stability and control.* New York: McGraw-Hill.Electrica Power Systems, 1994.

[72] F. Milano, F. Dörfler, G. Hug, D. J. Hill, and G. Verbi, "Foundations and challenges of low-inertia systems (invited paper)," *2018 Power Systems Computation Conference (PSCC)*, pp. 1–25, 2018.

[73] Primary secondary and tertiary frequency control - engineering articles. [Online]. Available: https://top10electrical.blogspot.com/2015/10/primary-secondary-and-tertiary.html

[74] Y. Rebours and D. S. Kirschen, "What is spinning reserve," 2005.

[75] G. Liu and K. Tomsovic, "Quantifying spinning reserve in systems with significant wind power penetration," *IEEE Transactions on Power Systems*, vol. 27, no. 4, pp. 2385–2393, 2012.

[76] M. Q. Wang and H. Gooi, "Spinning reserve estimation in microgrids," *IEEE Transactions on Power Systems*, vol. 26, no. 3, pp. 1164–1174, 2011.

[77] M. A. Ortega-Vazquez and D. S. Kirschen, "Optimizing the spinning reserve requirements using a cost/benefit analysis," *IEEE Transactions on Power Systems*, vol. 22, no. 1, pp. 24–33, 2007.

[78] M. Dreidy, H. Mokhlis, and S. Mekhilef, "Inertia response and frequency control techniques for renewable energy sources: A review," *Renewable and sustainable energy reviews*, vol. 69, pp. 144–155, 2017.

[79] H.-H. Yu, K.-H. Chang, H.-W. Hsu, and R. Cuckler, "A monte carlo simulation-based decision support system for reliability analysis of taiwan's power system: Framework and empirical study," *Energy*, vol. 178, pp. 252–262, 2019.

[80] M. A. El-Shennawy, S. A. S. Farghal, A. E. A. Amin, and S. M. Abdelkader, "Impact of renewable energy sources on inertia and frequency response of power systems," *MEJ. Mansoura Engineering Journal*, vol. 43, no. 3, pp. 19–23, 2020.

[81] M. Milligan, B. Kirby, H. Holttinen *et al.*, "Impact of large-scale wind penetration on grid reliability," in *IEEE Power and Energy Society General Meeting*, 2009, pp. 1–9.

[82] C. Hiroux and M. Saguan, "Large-scale wind power in european electricity markets: Time for revisiting support schemes and market designs?" *Energy Policy*, vol. 38, no. 7, pp. 3135–3145, 2010.

[83] A. Sharma, M. Jain, and R. Saxena, "Economic dispatch of renewable energy sources with output curtailment," *International Journal of Renewable Energy Research*, vol. 10, no. 1, pp. 158–167, 2020.

[84] R. A. Rodríguez, G. B. Andresen, S. Becker, and other, "Transmission needs across a fully renewable european power system," *Renewable Energy*, vol. 63, pp. 467–476, 2015.

[85] J. Zhang, S. Huang, and X. Li, "Control of wind power generation under varying conditions," *Renewable Energy*, vol. 114, pp. 63–72, 2017.

[86] Y. Jiang, R. Pates, and E. Mallada, "Dynamic droop control in low-inertia power systems," *IEEE Transactions on Automatic Control*, vol. 66, no. 8, pp. 3518–3533, 2020.

[87] M. Nedd, C. Booth, and K. Bell, "Potential solutions to the challenges of low inertia power systems with a case study concerning synchronous condensers," in *2017 52nd International Universities Power Engineering Conference (UPEC)*. IEEE, 2017, pp. 1–6.

[88] J. Fang, H. Li, Y. Tang, and F. Blaabjerg, "On the inertia of future more-electronics power systems," *IEEE Journal of Emerging and Selected Topics in Power Electronics*, vol. 7, no. 4, pp. 2130–2146, 2018.

[89] R. Yan, T. K. Saha *et al.*, "Cascading contingencies in low inertia power systems: Frequency response challenges and a potential solution," in *2017 IEEE Power & Energy Society General Meeting*. IEEE, 2017, pp. 1–5.

[90] R. Yan, T. K. Saha, N. Modi, N.-A. Masood, and M. Mosadeghy, "The combined effects of high penetration of wind and PV on power system frequency response," *Applied Energy*, vol. 145, pp. 320–330, 2015.

[91] M. H. Bollen, *Understanding Power Quality Problems: Voltage Sags and Interruptions*. Wiley IEEE Press, 2003.

[92] U. Datta, A. Kalam, and J. Shi, "A review of key functionalities of battery energy storage system in renewable energy integrated power systems," *Energy Storage*, vol. 3, no. 5, p. e224, 2021.

[93] X. Liang, "Emerging power quality challenges due to integration of renewable energy sources," *IEEE Transactions on Industry Applications*, vol. 53, no. 2, pp. 855–866, 2016.

[94] J. Ndirangu, J. Nderu, A. Muhia, and C. Maina, "Power quality challenges and mitigation measures in grid integration of wind energy conversion systems," in *2018 IEEE International Energy Conference (ENERGYCON)*. IEEE, 2018, pp. 1–6.

[95] J. Arrillaga, N. R. Watson, and S. Chen, *Power System Harmonics*. John Wiley & Sons, 1998.

[96] P. M. Ashton, C. S. Saunders, G. A. Taylor, A. M. Carter, and M. E. Bradley, "Inertia estimation of the GB power system using synchrophasor measurements," *IEEE Transactions on Power Systems*, vol. 30, no. 2, pp. 701–709, 2014.

[97] E. Heylen, F. Teng, and G. Strbac, "Challenges and opportunities of inertia estimation and forecasting in low-inertia power systems," *Renewable and Sustainable Energy Reviews*, vol. 147, p. 111176, 2021.

[98] G. Chavan, M. Weiss, A. Chakrabortty, S. Bhattacharya, A. Salazar, and F.-H. Ashrafi, "Identification and predictive analysis of a multi-area WECC power

system model using synchrophasors," *IEEE Transactions on Smart Grid*, vol. 8, no. 4, pp. 1977–1986, 2016.

[99] N. Janssens and A. Kamagate, "Interarea oscillations in power systems," *IFAC Proceedings Volumes*, vol. 33, no. 5, pp. 217–226, 2000.

[100] P. Cuffe, P. Smith, and A. Mullane, "System strength: definition, issues, and solutions," *IET Renewable Power Generation*, vol. 13, no. 2, pp. 166–173, 2019.

[101] X. Wang, P. Wang, Y. Wang, and F. Shi, "Online estimation of short-circuit fault level in active distribution network," *Applied Sciences*, vol. 10, no. 11, p. 3812, 2020.

[102] S. Peyghami, Z. Wang, and F. Blaabjerg, "Reliability modeling of power electronic converters: A general approach," in *2019 20th workshop on control and modeling for power electronics (COMPEL)*. IEEE, 2019, pp. 1–7.

[103] S. Peyghami, F. Blaabjerg, and P. Palensky, "Incorporating power electronic converters reliability into modern power system reliability analysis," *IEEE Journal of Emerging and Selected Topics in Power Electronics*, vol. 9, no. 2, pp. 1668–1681, 2020.

[104] Y. Song and B. Wang, "Survey on reliability of power electronic systems," *IEEE transactions on power electronics*, vol. 28, no. 1, pp. 591–604, 2012.

[105] T. Dragičević, P. Wheeler, and F. Blaabjerg, "Artificial intelligence aided automated design for reliability of power electronic systems," *IEEE Transactions on Power Electronics*, vol. 34, no. 8, pp. 7161–7171, 2018.

[106] J. Falck, C. Felgemacher, A. Rojko, M. Liserre, and P. Zacharias, "Reliability of power electronic systems: An industry perspective," *IEEE Industrial Electronics Magazine*, vol. 12, no. 2, pp. 24–35, 2018.

[107] S. Peyghami, P. Davari, and F. Blaabjerg, "System-level reliability-oriented power sharing strategy for dc power systems," *IEEE Transactions on Industry Applications*, vol. 55, no. 5, pp. 4865–4875, 2019.

[108] Y.-Y. Hong, C.-I. Wu, T.-H. Hsiao, and C.-S. Lin, "Reliability of a power system with high penetration of renewables: A scenario-based study," *IEEE Access*, vol. 9, pp. 78 050–78 059, 2021.

[109] B. Zhang, M. Wang, and W. Su, "Reliability analysis of power systems integrated with high-penetration of power converters," *IEEE Transactions on Power Systems*, vol. 36, no. 3, pp. 1998–2009, 2020.

[110] B. Zhang, M. Wang, and W. Su, "Reliability assessment of converter-dominated power systems using variance-based global sensitivity analysis," *IEEE Open Access Journal of Power and Energy*, vol. 8, pp. 248–257, 2021.

[111] K. S. Ratnam, K. Palanisamy, and G. Yang, "Future low-inertia power systems: Requirements, issues, and solutions-a review," *Renewable and Sustainable Energy Reviews*, vol. 124, p. 109773, 2020.

[112] H. T. Nguyen, G. Yang, A. H. Nielsen, and P. H. Jensen, "Combination of synchronous condenser and synthetic inertia for frequency stability enhancement in low-inertia systems," *IEEE Transactions on Sustainable Energy*, vol. 10, no. 3, pp. 997–1005, 2018.

[113] V. Arayamparambil Vinaya Mohanan, I. M. Mareels, R. J. Evans, and R. R. Kolluri, "Stabilising influence of a synchronous condenser in low inertia networks," *IET Generation, Transmission & Distribution*, vol. 14, no. 17, pp. 3582–3593, 2020.

[114] H. Beltran, S. Harrison, A. Egea-Àlvarez, and L. Xu, "Techno-economic assessment of energy storage technologies for inertia response and frequency support from wind farms," *Energies*, vol. 13, no. 13, p. 3421, 2020.

[115] Hornsdale Power Reserve, "Our vision," https://hornsdalepowerreserve.com.au/our-vision/, 2024, accessed: 2024-12-20.

[116] National Grid, "Enhanced frequency response faqs," 2016, version 5.0. [Online]. Available: https://www.nationalgrid.com/sites/default/files/documents/Enhanced%20Frequency%20Response%20FAQs%20v5.0_.pdf

[117] B. Gundogdu, S. Nejad, D. T. Gladwin, and D. A. Stone, "A battery energy management strategy for uk enhanced frequency response," in *2017 IEEE 26th*

International Symposium on Industrial Electronics (ISIE). IEEE, 2017, pp. 26–31.

[118] H. Bevrani, H. Golpira, A. R. Messina, N. Hatziargyriou, F. Milano, and T. Ise, "Power system frequency control: An updated review of current solutions and new challenges," *Electric Power Systems Research*, vol. 194, p. 107114, 2021.

[119] R. K. Sarojini, K. Palanisamy, P. Sanjeevikumar, and J. B.-H. Nielsen, "Inertia emulation control technique based frequency control of grid-connected single-phase rooftop photovoltaic system with battery and supercapacitor," *IET Renewable Power Generation*, vol. 14, no. 7, pp. 1156–1163, 2020.

[120] A. Kasis, N. Monshizadeh, and I. Lestas, "Secondary frequency control with on–off load side participation in power networks," *IEEE Transactions on Control of Network Systems*, vol. 7, no. 2, pp. 603–613, 2019.

[121] I. M. Alotaibi, M. Abido, and M. Khalid, "Primary frequency regulation by demand side response," *Arabian Journal for Science and Engineering*, vol. 46, no. 10, pp. 9627–9637, 2021.

[122] H. Karbouj, Z. Rather, D. Flynn, and H. Qazi, "Non-synchronous fast frequency reserves in renewable energy integrated power systems: a critical review," *Electrical Power and Energy Systems*, vol. 106, pp. 488–501, Mar. 2019.

[123] S. Williams, M. Short, and T. Crosbie, "On the use of thermal inertia in building stock to leverage decentralised demand side frequency regulation services," *Applied Thermal Engineering*, vol. 133, pp. 97–106, 2018.

[124] E. O. Kontis, I. D. Pasiopoulou, D. A. Kirykos, T. A. Papadopoulos, and G. K. Papagiannis, "Estimation of power system inertia: A comparative assessment of measurement-based techniques," *Electric Power Systems Research*, vol. 196, p. 107250, 2021.

[125] H. Bevrani, T. Ise, and Y. Miura, "Virtual synchronous generators: A survey and new perspectives," *International Journal of Electrical Power & Energy Systems*, vol. 54, pp. 244–254, 2014.

[126] L. He and S. Yu, "Systematic decoupling grid-forming control for utility-scale inverter-based distributed energy resources in weak distribution grids," *IEEE Open Access Journal of Power and Energy*, 2024.

[127] J. M. Guerrero, L. G. De Vicuna, J. Matas, M. Castilla, and J. Miret, "Output impedance design of parallel-connected ups inverters with wireless load-sharing control," *IEEE Transactions on industrial electronics*, vol. 52, no. 4, pp. 1126–1135, 2005.

[128] G. Li, F. Ma, A. Luo, Z. He, W. Wu, X. Wei, Z. Zhu, and J. Guo, "Virtual impedance-based virtual synchronous generator control for grid-connected inverter under the weak grid situations," *IET Power Electronics*, vol. 11, no. 13, pp. 2125–2132, 2018.

[129] C. Zheng, T. Dragičević, and F. Blaabjerg, "Model predictive control-based virtual inertia emulator for an islanded alternating current microgrid," *IEEE Transactions on Industrial Electronics*, vol. 68, no. 8, pp. 7167–7177, 2020.

[130] C. Dou, Z. Zhang, D. Yue, and M. Song, "Improved droop control based on virtual impedance and virtual power source in low-voltage microgrid," *IET Gener. Transm. Distrib*, vol. 11, no. 4, pp. 1046–1054, 2017.

[131] B. Fan, Q. Li, W. Wang, G. Yao, H. Ma, X. Zeng, and J. M. Guerrero, "A novel droop control strategy of reactive power sharing based on adaptive virtual impedance in microgrids," *IEEE Transactions on Industrial Electronics*, vol. 69, no. 11, pp. 11 335–11 347, 2021.

[132] R. Aouini, B. Marinescu, K. B. Kilani, and M. Elleuch, "Synchronverter-based emulation and control of hvdc transmission," *IEEE Transactions on Power Systems*, vol. 31, no. 1, pp. 278–286, 2015.

[133] D. G. Photovoltaics and E. Storage, "IEEE application guide for IEEE Std 1547™, IEEE standard for interconnecting distributed resources with electric power systems," *IEEE std*, pp. 1547–2, 2009.

[134] N. C. Colombage, "Design and control of on-board bidirectional battery chargers with islanding detection for electric vehicle applications," Ph.D. dissertation, University of Sheffield, 2015.

[135] F. Liu, X. Zhang, C. Yu, Z. Shao, W. Zhao, and H. Ni, "LCL-filter design for grid-connected three-phase PWM converter based on maximum current ripple," in *2013 IEEE ECCE Asia Downunder*. IEEE, 2013, pp. 631–635.

[136] M. Dursun and M. K. DÖŞOĞLU, "LCL filter design for grid connected three-phase inverter," in *2018 2nd International Symposium on Multidisciplinary Studies and Innovative Technologies (ISMSIT)*. IEEE, 2018, pp. 1–4.

[137] M. Liserre, F. Blaabjerg, and S. Hansen, "Design and control of an LCL-filter-based three-phase active rectifier," *IEEE Transactions on industry applications*, vol. 41, no. 5, pp. 1281–1291, 2005.

[138] A. Reznik, M. G. Simões, A. Al-Durra, and S. Muyeen, "LCL filter design and performance analysis for grid-interconnected systems," *IEEE transactions on industry applications*, vol. 50, no. 2, pp. 1225–1232, 2013.

[139] J. Xu, S. Xie, L. Huang, and L. Ji, "Design of LCL-filter considering the control impact for grid-connected inverter with one current feedback only," *IET Power Electronics*, vol. 10, no. 11, pp. 1324–1332, 2017.

[140] M. H. Bollen, "Understanding power quality problems," in *Voltage sags and Interruptions*. IEEE press Piscataway, NJ, USA, 2000.

[141] I. S. Association, "Ieee standard for interconnection and interoperability of distributed energy resources with associated electric power systems interfaces," *IEEE Std 1547-2018*, 2018, accessed on: Jan 3, 2025.

[142] E. N. of Transmission System Operators for Electricity (ENTSO-E), "Requirements for generators (rfg)," Available at https://www.entsoe.eu, 2016, accessed on: Jan 3, 2025.

[143] VDE, *Technical Requirements for the Connection and Operation of Customer Installations to the High Voltage Network (VDE-AR-N 4120)*. VDE Verlag, 2015, accessed on: Jan 3, 2025.

[144] A. E. M. O. (AEMO), "National electricity rules (ner)," Available at https://www.aemo.com.au, 2021, accessed on: Jan 3, 2025.

[145] NationalGridESO. The grid code. [Online]. Available: https://www.nationalgrideso.com/document/162271/download

[146] H. Berndt, M. Hermann, H. D. Kreye, R. Reinisch, U. Scherer, and J. Vanzetta. Transmission code 2007: Network and system rules of the german transmission system operators. [Online]. Available: https://www.vde.com

[147] X. Bao, P. Tan, F. Zhuo, and X. Yue, "Low voltage ride through control strategy for high-power grid-connected photovoltaic inverter," in *2013 Twenty-Eighth Annual IEEE Applied Power Electronics Conference and Exposition (APEC)*. IEEE, 2013, pp. 97–100.

[148] Y. He, M. Wang, Y. Jia, J. Zhao, and Z. Xu, "Low-voltage ride-through control for photovoltaic generation in the low-voltage distribution network," *IET Renewable Power Generation*, vol. 14, no. 14, pp. 2727–2737, 2020.

[149] Y. Yang, F. Blaabjerg, and H. Wang, "Low-voltage ride-through of single-phase transformerless photovoltaic inverters," *IEEE Transactions on Industry Applications*, vol. 50, no. 3, pp. 1942–1952, 2013.

[150] R. Zeng and M. S. Chinthavali, "Fault ride-through control strategy for single-phase virtual synchronous generator," in *2019 IEEE Power & Energy Society Innovative Smart Grid Technologies Conference (ISGT)*. IEEE, 2019, pp. 1–5.

[151] J. Alipoor, Y. Miura, and T. Ise, "Voltage sag ride-through performance of virtual synchronous generator," *IEEJ Journal of Industry Applications*, vol. 4, no. 5, pp. 654–666, 2015.

[152] J. Bock, A. Hobl, J. Schramm, S. Krämer, and C. Jänke, "Resistive superconducting fault current limiters are becoming a mature technology," *IEEE Transactions on Applied Superconductivity*, vol. 25, no. 3, pp. 1–4, 2014.

[153] L. Chen, H. Chen, J. Yang, L. Zhu, Y. Tang, L. H. Koh, Y. Xu, C. Zhang, Y. Liao, and L. Ren, "Comparison of superconducting fault current limiter and dynamic

voltage restorer for LVRT improvement of high penetration microgrid," *IEEE Transactions on Applied Superconductivity*, vol. 27, no. 4, pp. 1–7, 2017.

[154] J.-F. Moon, S.-H. Lim, J.-C. Kim, and S.-Y. Yun, "Assessment of the impact of SFCL on voltage sags in power distribution system," *IEEE Transactions on Applied Superconductivity*, vol. 21, no. 3, pp. 2161–2164, 2010.

[155] S. Alaraifi and M. S. El Moursi, "Design considerations of superconducting fault current limiters for power system stability enhancement," *IET Generation, Transmission & Distribution*, vol. 11, no. 9, pp. 2155–2163, 2017.

[156] N. Hayakawa, Y. Maeno, and H. Kojima, "Fault current limitation coordination in electric power grid with superconducting fault current limiters," *IEEE Transactions on Applied Superconductivity*, vol. 28, no. 4, pp. 1–4, 2018.

[157] A. Komijani, M. Sedighizadeh, and M. Kheradmandi, "Improving fault ride-through in meshed microgrids with wind and PV by virtual synchronous generator with SFCL and SMES," *Journal of Energy Storage*, vol. 50, p. 103952, 2022.

[158] J. Rodriguez and P. Cortes, *Predictive control of power converters and electrical drives*. John Wiley & Sons, 2012.

[159] L. Wang, S. Chai, D. Yoo, L. Gan, and K. Ng, *PID and predictive control of electrical drives and power converters using MATLAB/Simulink*. John Wiley & Sons, 2015.

[160] T. Liu, A. Chen, F. Gao, X. Liu, X. Li, and S. Hu, "Double-loop control strategy with cascaded model predictive control to improve frequency regulation for islanded microgrids," *IEEE Transactions on Smart Grid*, vol. 13, no. 5, pp. 3954–3967, 2021.

[161] B. Long, Y. Liao, K. T. Chong, J. Rodríguez, and J. M. Guerrero, "MPC-controlled virtual synchronous generator to enhance frequency and voltage dynamic performance in islanded microgrids," *IEEE Transactions on Smart Grid*, vol. 12, no. 2, pp. 953–964, 2020.

[162] J. Jongudomkarn, J. Liu, and T. Ise, "Virtual synchronous generator control with reliable fault ride-through ability: A solution based on finite-set model predictive

control," *IEEE journal of emerging and selected topics in power electronics*, vol. 8, no. 4, pp. 3811–3824, 2019.

[163] D. A. Kisinga and P. Trodden, "A low voltage ride through (lvrt) strategy using an active superconductor fault current limiter (sfcl) for a virtual synchronous generator (vsg) connected to a weak grid," in *2023 IEEE PES Innovative Smart Grid Technologies Europe (ISGT EUROPE)*. IEEE, 2023, pp. 1–5.

[164] C. Alexander and M. Sadiku, *Fundamentals of electric circuits*, 3rd ed. McGraw-Hill Education, 2006.

[165] B. Stellato, T. Geyer, and P. J. Goulart, "High-speed finite control set model predictive control for power electronics," *IEEE Transactions on power electronics*, vol. 32, no. 5, pp. 4007–4020, 2016.

[166] B. Tan, J. Zhao, M. Netto, V. Krishnan, V. Terzija, and Y. Zhang, "Power system inertia estimation: Review of methods and the impacts of converter-interfaced generations," *International Journal of Electrical Power & Energy Systems*, vol. 134, p. 107362, 2022.

[167] U. Tamrakar, D. A. Copp, T. A. Nguyen, T. M. Hansen, and R. Tonkoski, "Real-time estimation of microgrid inertia and damping constant," *IEEE Access*, vol. 9, pp. 114 523–114 534, 2021.

[168] E. Carlini, F. Del Pizzo, G. Giannuzzi, D. Lauria, F. Mottola, and C. Pisani, "Online analysis and prediction of the inertia in power systems with renewable power generation based on a minimum variance harmonic finite impulse response filter," *International Journal of Electrical Power & Energy Systems*, vol. 131, p. 107042, 2021.

[169] D. Yang, B. Wang, G. Cai, J. Ma, J. Tian, Z. Chen, and L. Wang, "Inertia-adaptive model predictive control-based load frequency control for interconnected power systems with wind power," *IET Generation, Transmission & Distribution*, vol. 14, no. 22, pp. 5029–5036, 2020.

[170] E. Heylen, J. Browell, and F. Teng, "Probabilistic day-ahead inertia forecasting," *IEEE Transactions on Power Systems*, 2021.

[171] T. Inoue, H. Taniguchi, Y. Ikeguchi, and K. Yoshida, "Estimation of power system inertia constant and capacity of spinning-reserve support generators using measured frequency transients," *IEEE Transactions on Power Systems*, vol. 12, no. 1, pp. 136–143, 1997.

[172] D. P. Chassin, Z. Huang, M. K. Donnelly, C. Hassler, E. Ramirez, and C. Ray, "Estimation of WECC system inertia using observed frequency transients," *IEEE Transactions on Power Systems*, vol. 20, no. 2, pp. 1190–1192, 2005.

[173] P. Du and Y. Makarov, "Using disturbance data to monitor primary frequency response for power system interconnections," *IEEE Transactions on Power Systems*, vol. 29, no. 3, pp. 1431–1432, 2013.

[174] P. Ashton, G. Taylor, A. Carter, M. Bradley, and W. Hung, "Application of phasor measurement units to estimate power system inertial frequency response," in *2013 IEEE Power & Energy Society General Meeting*. IEEE, 2013, pp. 1–5.

[175] M. Sun, Y. Feng, P. Wall, S. Azizi, J. Yu, and V. Terzija, "On-line power system inertia calculation using wide area measurements," *International Journal of Electrical Power & Energy Systems*, vol. 109, pp. 325–331, 2019.

[176] D. Zografos, M. Ghandhari, and K. Paridari, "Estimation of power system inertia using particle swarm optimization," in *2017 19th International Conference on Intelligent System Application to Power Systems (ISAP)*. IEEE, 2017, pp. 1–6.

[177] C. Phurailatpam, Z. H. Rather, B. Bahrani, and S. Doolla, "Measurement-based estimation of inertia in AC microgrids," *IEEE Transactions on Sustainable Energy*, vol. 11, no. 3, pp. 1975–1984, 2019.

[178] D. Wilson, J. Yu, N. Al-Ashwal, B. Heimisson, and V. Terzija, "Measuring effective area inertia to determine fast-acting frequency response requirements," *International Journal of Electrical Power & Energy Systems*, vol. 113, pp. 1–8, 2019.

[179] N. Hosaka, B. Berry, and S. Miyazaki, "The world's first small power modulation injection approach for inertia estimation and demonstration in the island

grid," in *2019 8th International Conference on Renewable Energy Research and Applications (ICRERA)*. IEEE, 2019, pp. 722–726.

[180] R. J. Best, P. V. Brogan, and D. J. Morrow, "Power system inertia estimation using HVDC power perturbations," *IEEE Transactions on Power Systems*, vol. 36, no. 3, pp. 1890–1899, 2020.

[181] NationalGridESO. Future system inertia. [Online]. Available: https://eepublicdownloads.entsoe.eu/clean-documents/Publications/SOC/Nordic/Nordic_report_Future_System_Inertia.pdf

[182] B. Wang, H. Sun, W. Li, C. Yang, W. Wei, B. Zhao, and S. Xu, "Power system inertia estimation method based on maximum frequency deviation," *IET Renewable Power Generation*, vol. 16, no. 3, pp. 622–633, 2022.

[183] X. Cao, B. Stephen, I. F. Abdulhadi, C. D. Booth, and G. M. Burt, "Switching markov gaussian models for dynamic power system inertia estimation," *IEEE Transactions on Power Systems*, vol. 31, no. 5, pp. 3394–3403, 2015.

[184] J. Zhang and H. Xu, "Online identification of power system equivalent inertia constant," *IEEE Transactions on Industrial Electronics*, vol. 64, no. 10, pp. 8098–8107, 2017.

[185] J. Zhang and H. Xu, "Microperturbation method for power system online model identification," *IEEE Transactions on Industrial Informatics*, vol. 12, no. 3, pp. 1055–1063, 2016.

[186] M. Karrari and O. Malik, "Identification of physical parameters of a synchronous generator from online measurements," *IEEE transactions on energy conversion*, vol. 19, no. 2, pp. 407–415, 2004.

[187] M. Cui, J. Qi, and K. Sun, "A review of phasor measurement unit applications in power system analysis," *IEEE Transactions on Smart Grid*, vol. 10, no. 4, pp. 4500–4513, 2019. [Online]. Available: https://doi.org/10.1109/TSG.2018.2889823

[188] M. H. None, L. Ding, M. K. None, W. B. None, X. Z. None, M. Popov, and V. Terzija, "A review on application of machine learning-based methods for power system inertia monitoring," 2024.